1. MECHANICAL DETECTION OF ELECTRON SPIN RESONANCE FROM NITROXIDE SPIN PROBES, 2. ULTRASENSITIVE CANTILEVER TORQUE MAGNETOMETRY OF MAGNETIZATION SWITCHING IN INDIVIDUAL NICKEL NANORODS

A Dissertation

Presented to the Faculty of the Graduate School

of Cornell University

in Partial Fulfillment of the Requirements for the Degree of

Doctor of Philosophy

by

Eric W. Moore

January 2012

1. MECHANICAL DETECTION OF ELECTRON SPIN RESONANCE FROM NITROXIDE SPIN PROBES, 2. ULTRASENSITIVE CANTILEVER TORQUE MAGNETOMETRY OF MAGNETIZATION SWITCHING IN INDIVIDUAL NICKEL NANORODS

Eric W. Moore, Ph.D.

Cornell University 2012

In 2004 mechanical detection of magnetic resonance was used to detect a single electron spin. However, the demonstration required a carefully chosen sample and the techniques developed there are not immediately applicable to detecting single electron spins in organic spin labels and probes widely used in biology. In this dissertation ultrasensitive mechanical detection of magnetic resonance is extended to detect electron spin resonance from TEMPAMINE, a nitroxide spin probe. Using an ultrasensitive cantilever with a spherical nickel tip $4\,\mu\text{m}$ in diameter $400\,\mu_{\text{B}}$ sensitivity was demonstrated in a force gradient experiment and a route to single nitroxide spin detection outlined. A necessity for reaching single spin sensitivity is controlling the close approach surface force and frequency noise the cantilever experiences. Using a nickel nanorod with $100\,\text{nm} \times 100\text{nm}$ cross section batch-fabricated to overhang the tip of an ultrasensitive cantilever by $350\,\text{nm}$, the lowest surface force noise ever achieved in a scanned-probe experiment was demonstrated and the magnetic tip used to detect electron spin resonance. Unfortunately, the surface frequency noise experienced by the batch-fabricated tip was extremely large and the demonstrated sensitivity of the batch fabricated tip is poor. To take advantage of the extremely low surface force noise experienced by the overhanging tip, a technique based on non degenerate parametric amplification that converts

a modulated frequency shift into an on resonance amplitude was developed and demonstrated.

Mechanical detection requires a very high quality magnetic tip, however, the tip must be small and located at the end of a fragile cantilever. A non destructive way to determine the magnetic moment and anisotropy constant for the magnetic tip is cantilever torque magnetometry. Prior studies have investigated in-plane switching and here the in-plane to out-of-plane transition is studied. Multiple sharp, simultaneous transitions in cantilever frequency, dissipation and jitter were observed as the external field was swept. A quantitative model for the frequency shift at high field and qualitative models for the frequency shift and dissipation peaks near the switching field were developed.

BIOGRAPHICAL SKETCH

Eric William Moore was born on May 4, 1983 just outside of Pittsburgh in Monroeville, Pennsylvania. He grew up in western Pennsylvania and graduated from Penn-Trafford High School in the spring of 2001. Following high school, he migrated across the state to attend Drexel University. Unlike nearly all other Drexel students he foolishly chose not to participate in the co-op program and graduated in the spring of 2005, earing a Bachelor of Science degree in Chemistry. While at Drexel he worked on functionalizing carbon nanotubes using bipolar electrodeposition with Prof. Jean-Claude Bradley and took part in the NNIN RUE program during the summer of 2004, working with Prof. Seong Kim at Penn State on electrospinning of hydrogel nanofibers. Eric arrived at Cornell in the fall of 2005 and elected to join Prof. John Marohn's group to work on mechanical detection of magnetic resonance.

ACKNOWLEDGEMENTS

I would like to thank the following people who contributed to this work and made my experiences in graduate school as gratifying as they have been. My advisor, John Marohn, whose support and guidance made this thesis possible. More than anyone else, John brings unending enthusiasm to every project and every bit of new data. He has a strong vision for where MRFM can go and the drive to take it there. I worked closely with SangGap Lee during graduate school and suspect there is no aspect of our experiment that we haven't argued (often fruitlessly) about. I hope that I was able to teach him at least a fraction of what he taught me. The rest of team MRFM, Seppe, Steve, Joni, Sarah and Lee, thanks for making this such a fun project to work on. To the rest of the Marohn group, I'm grateful to have had the experiences sharing an office and lab space with you. The people in the group are what make it an enjoyable place to work.

TABLE OF CONTENTS

LIST OF FIGURES

LIST OF TABLES

CHAPTER 1

INTRODUCTION

Following the first demonstrations of electron spin resonance in 1944[1] and nuclear magnetic resonance in 1946, [2, 3] magnetic resonance techniques have become vital tools in many branches of science and medicine. As a spectroscopic technique, magnetic resonance provides a wealth of information on the structure and dynamics of molecules, up to and including moderately sized proteins. Magnetic resonance imaging, developed starting in the 1970s[4, 5], is a dominate clinical imaging tool providing a routine, non-invasive view of structure and function with in the body. Through these two modalities, magnetic resonance can provide insights covering both large, tens to hundreds of micrometers and up, and small, molecular length scales. However, intermediate lengths, ranging from a few micrometers down to a few nanometers represent a blind spot of sorts, too large for most spectroscopic techniques and too small for conventional imaging. Unfortunately, this is precisely the length scale of much of biology and of much modern technology. The work presented in this thesis is primarily concerned with attempting to bridge this gap through the further development of a magnetic resonance technique based around mechanical detection of magnetic resonance, known as magnetic resonance force microscopy or MRFM.

Magnetic resonance force microscopy was proposed in 1991[6] as a nondestructive, 3-dimensional imaging technique capable of extremely high spatial resolution. The proposal was motivated by the desire for a tool capable of imaging biological structures for the purposes of advancing our understanding and treatment of disease. Although this is still the goal that motivates much of the work, mechanical detection is a general detection method and applications have emerged or are

proposed in studies of nanostructured magnetic devices[7], superconductivity[8], quantum dots[9], organic electronics, dopants in semiconductors[10] and quantum computing[11–13].

In study of molecular scale biological structure the two dominate tools are X-ray diffraction and conventional NMR. Despite the large number of studies and the insights these tools provide there are strong limits on the samples that can be studied using them. X-ray diffraction requires a crystalline sample, which is difficult or impossible to obtain for many large biomolecules and for very large or difficult to crystallize molecules a synchrotron X-ray source may also be necessary[14]. Likewise, liquid state NMR is limited to small ($\lesssim 50$ kDa) expressible proteins that do not aggregate in the high concentrations required for data collection[15]. Solid state NMR is a powerful tool for studying polycrystalline or amorphous solids and because the dipolar coupling is not removed by molecular tumbling, it represents an excellent opportunity to directly access molecular structure. However it remains difficult to collect spectra at high enough resolution to permit full assignment of the observed resonances and many of the structural studies to date have depended on accessing structural information through large numbers of qualitative constraints[16–18].

For macromolecules not amenable to analysis by conventional NMR or X-ray diffraction, the tertiary structure of proteins[19–21], nucleic acids[22, 23] and biomolecular assembles[24, 25] can be explored by using inductively-detected ESR to measure distances between pairs of attached spin labels[20–23, 25, 26]. These studies, however, require bulk quantities of sample[27] and demand multiple experiments with spin labels attached to different locations in the target macromolecule. Mechanical detection and imaging of single-electron spins has been demonstrated,

in E' centers in gamma-irradiated quartz[28] and this thesis represents the beginning of an effort to apply magnetic resonance force microscopy to map the locations of individual spin labels attached to a single biomacromolecule.

1.1 MRFM Basics

In contrast to conventional magnetic resonance where transverse spin magnetization is detected by via the electromotive force induced in a receiver coil (or other resonant structure) by the precession of spin magnetic moments, MRFM detects spin magnetization by using the gradient-dipole force between the spin magnetic moment and a magnetic field gradient source, generally a small ferromagnet, mounted on a microcantilever. The gradient-dipole force is

$$\boldsymbol{F} = (\boldsymbol{\mu} \cdot \nabla) \, \boldsymbol{B} \tag{1.1}$$

where $\boldsymbol{\mu}$ is the vector magnetic moment, $\boldsymbol{B}$ is the magnetic field, and $\boldsymbol{F}$ is the force. Although the original proposal[6] was to directly detect the precession of the spin magnetic moments by matching the cantilever's resonant frequency to the spin's Larmor frequency, all successful MRFM experiments to date have detected the longitudinal spin magnetization. Eq. 1.1 can be simplified by keeping only the term involving the longitudinal spin magnetic moment, μ_z, that also produces a force oriented along the cantilever's soft direction,

$$F_x = \mu_z \frac{\partial B_z}{\partial x} = \mu_z G. \tag{1.2}$$

Eq. 1.2 shows that the size of the force is determined by the magnetic moment of the spin, a constant of nature, and the achievable magnetic field gradient, which, fortunately, depends on the experiment design.

Shown in Fig. 1.1 are schematics of the experimental geometries used in all

3
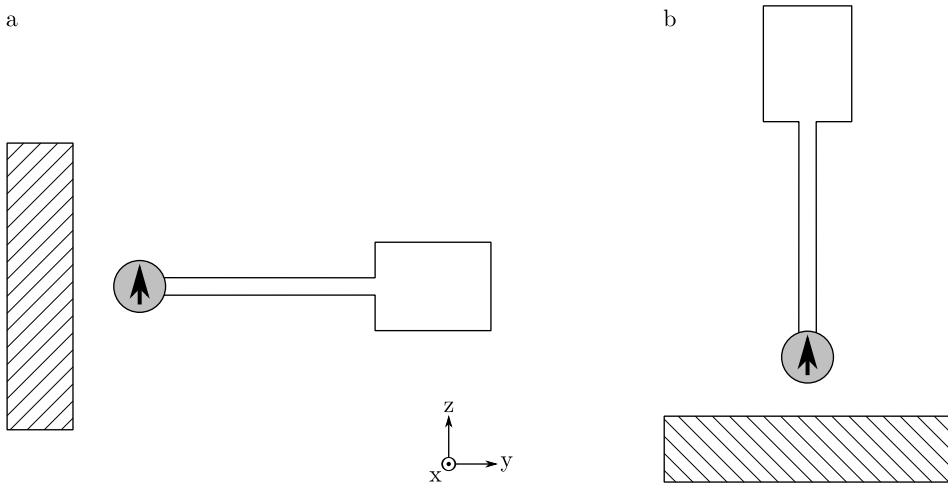
Figure 1.1: Schematics of the two geometries used in ultrasensitive MRFM, (a) the springiness preservation by aligning magnetization or SPAM geometry used for the work presented here and (b) the hang down geometry. For both schematics, the cantilever is white and oscillates in x, in and out of the page, the magnetic tip is gray, and the sample is cross hatched.

high-sensitivity MRFM experiments. In both geometries the long axis of the cantilever is normal to the sample surface and the cantilever oscillates parallel to the sample surface. The cantilever is approached to the surface in this pendulum geometry rather than the convention AFM geometry (long axis parallel, oscillation normal) because the electrostatic and van der Waals forces between the body of the cantilever and the sample surface are strong enough to overcome the cantilever's spring constant and cause the cantilever to snap into contact with the surface. The geometry shown in Fig. 1.1(a) is called the springiness preservation by aligning magnetization or SPAM geometry[29, 30] and has the advantage that the external magnetic field does not cause either frequency shifts or dissipation in a magnetic tipped cantilever. A drawback in comparison to the geometry shown in Fig. 1.1(b), called the hang down geometry, is that the maximum attainable G is smaller by a factor of $3.2\times$ (for a spherical magnetic tip) in the SPAM geometry. This trade off can be worthwhile if the magnetic tip is large. All of the MRFM experiments presented in this thesis were carried out using the SPAM geometry.

Before considering questions of resolution and the details of actually using this force to create an image, it is worthwhile to consider the magnitude of the spin force in a representative experiment and potential signal-to-noise ratio (SNR) achievable when detecting the force. The magnetic field gradient produced by a small ferromagnet depends on the material of the magnet and its shape; let us consider a spherical magnetic tip magnetized along the z direction producing a magnetic field gradient,

$$G(x, y, z) = \mu_0 M r_{\text{tip}}^3 \frac{x\left(x^2 + y^2 - 4z^2\right)}{\left(x^2 + y^2 + z^2\right)^{7/2}}, \tag{1.3}$$

where r_{tip} is the radius of the magnetic tip, M is the tip magnetization, and the spin is located at (x, y, z) relative to the center of the magnet. In the coordinate system shown for the SPAM geometry in Fig. 1.1(a), the sample lies in the xz-plane and a spin located at $(2y, y, 0)$ feels the peak G of

$$G^{\text{peak}}(y) = \frac{16}{25\sqrt{5}} \frac{\mu_0 M r_{\text{tip}}^3}{y^4} \tag{1.4}$$

If we assume $r_{\text{tip}} = 50\,\text{nm}$, $\mu_0 M = 0.6\text{T}$ and a tip-sample separation $h = |y| - r_{\text{tip}} = 5\,\text{nm}$ the peak force from a single electron spin is $F_x = 22\,\text{aN}$, where $1\,\text{aN} = 1 \times 10^{-18}\,\text{N}$. Depending on the details of the experiment the force may be a static force or the force may be modulated at a frequency, f_{mod}. In either case the force will be detected by monitoring the deflection of the cantilever. The magnitude and phase of the cantilever's deflection, x_0 is determined by the cantilever's susceptibility, $\chi(f)$ and spring constant, k_c,

$$x_0 = F_x \frac{\chi(f)}{k_c} \tag{1.5}$$

where the force, F_x and response, x_0, are phasors. Modelling the cantilever as an underdamped harmonic oscillator, its susceptibility will be

$$\chi(f) = \frac{f_c^2}{f_c^2 - f^2 + i f f_c / Q} \tag{1.6}$$

5

where $f_c = \frac{1}{2\pi}\sqrt{\frac{k_c}{m}}$ is the cantilever's resonate frequency, m its effective mass and Q its quality factor.

The SNR with which the small spin force or any other force can be detected is limited by the microscopic fluctuating forces that act on the cantilever. In an ideal measurement the only source of force fluctuations is the cantilever's finite temperature, which gives rise to a fluctuating force with spectral density $P_F(f) = 4k_BT\Gamma$ where k_B is Boltzmann's constant, T is temperature and $\Gamma = k/2\pi f_c Q$ is the cantilever's friction coefficient. In a real measurement there are other source of force fluctuations external to the cantilever, such as fluctuating electric fields from the sample that couple to uncompensated charge on the cantilever's tip [31, 32]. These fluctuating forces, whatever the source, give rises to cantilever position fluctuations with power spectral density

$$P_{\delta x}(f) = P_F(t)\frac{|\chi(f)|^2}{k_c^2}. \tag{1.7}$$

The relevant noise amplitude for an AC measurement in a bandwidth, b will be

$$x_{\text{noise}} = \left(\int_{f_{\text{mod}}-b/2}^{f_{\text{mod}}+b/2} P_{\delta x}(f)\,df\right)^{1/2}, \tag{1.8}$$

where f_{mod} is the center frequency of the measurement.[1] For a small enough b the integral Eq. 1.8 can be approximated as as

$$x_{\text{noise}} = \sqrt{P_{\delta x}(f_{\text{mod}})b} = \sqrt{P_F(f_{\text{mod}})b}\frac{|\chi(f_{\text{mod}})|}{k_c} \tag{1.9}$$

where we have used Eq. 1.7. Using Eqs. 1.5 and 1.9 the SNR is

$$\text{SNR} = \frac{x_0}{x_{\text{noise}}} = \frac{F_x}{\sqrt{P_F(f_{\text{mod}})b}}. \tag{1.10}$$

---

[1]In a DC measurement, the lower integration limit will be 0 and the upper limit $b/2$ because we have defined $P_{\delta x}(f)$ as one-sided. Here we are defining b as the total width of the passband rather than the width of the equivalent baseband filter. This choice is necessary to identify the usual expression for F_{min} below.

The denominator of Eq. 1.10 for $b = 1\,\text{Hz}$ is known as the minimum detectable force, F_{min}. The value of r_{tip} and $\mu_0 M$ used to calculate $F_x = 22\,\text{aN}$ above are the nominal values for the magnetic tip used in Ref. 33 and Chapter 3. Using the measured value of Γ for that cantilever at $h = 5\,\text{nm}$, the minimum detectable force is $F_{\text{min}} = 8\,\text{aN}$, producing an estimated SNR $= 2.75$ in 1 s. The SNR ratio in Eq. 1.10 will be independent of the modulation frequency if $P_F(f)$ is white, as it is in a thermally limited measurement[34]. However, nearly all high-sensitivity force measurements modulate the force at f_c for two reasons. One, external noise sources do not necessarily have a white spectrum (e.g. building or microscope vibrations). And two, the finite sensitivity of real displacement sensors means that the displacement sensor becomes the dominate source of noise away from the Q enhanced response near the resonant frequency.

Although the highest sensitivity MRFM experiment[35] to date used force detection, the single electron spin experiment of Rugar *et al.* [28], and the experiments presented here [33, 36, 37] detect the spin force via a small change in the cantilever's spring constant. Experimentally, one detects changes to the spring constant by using the cantilever as the frequency determining element in a positive feedback circuit which drives the cantilever to a non-zero amplitude while monitoring the cantilever's resonant frequency. One of the principle advantages of frequency shift detection is that, unlike the cantilever's amplitude which requires several cantilever damping times $\tau = Q/\pi f_c$ to reach steady state, the resonant frequency shifts instantaneously [38]. For a small shift, the change in spring constant, Δk is related to the change in frequency, Δf, as

$$\frac{\Delta f}{f_c} = \frac{\Delta k}{2k_c}. \tag{1.11}$$

The Δk in an MRFM experiment can be calculated by expanding Eq. 1.1 in a

Taylor series about the cantilever's equilibrium position, and identifying the first derivative term, $\frac{dF_x}{dx}x$ as having the same form as Hooke's Law and $\Delta k \equiv \frac{dF_x}{dx}$. Evaluating the derivative of Eq. 1.1 we find

$$\Delta k = \frac{d\mu_z}{dx}G + \mu_z\frac{dG}{dx}$$
$$= \frac{d\mu_x}{dx}\frac{dB_z}{dx} + \mu_z\frac{d^2B_z}{dx^2}. \qquad (1.12)$$

To produce a Δk the first term in Eq. 1.12 requires that the spin magnetic moment depend on the cantilevers position, a requirement which is most easily fulfilled by inverting the spin every half cantilever cycle [39–41]. The Δk produced by the second term does not require any particular spin modulation. Using the second term to detect spins has been named Cantilever Enabled Readout of Magnetization Inversion Transients or CERMIT by Garner and coworkers [42] because after a volume of spins have been inverted, the Δk they produced tracks the return to thermal equilibrium directly and can be used to measure the spin-lattice relaxation time. The CERMIT effect has been used to detect the thermal polarization of [71]Ga[42, 43] and [69]Ga[43] spins, the statistical polarization of [19]F[44] spins, and— in the experiments presented here—the thermal polarization of electron spins in TEMPAMINE, an nitroxide free radical.

In a thermally limited force gradient measurement the thermomechanical position fluctuations of the cantilever appear as a white spectrum of frequency fluctuations,

$$P_{\delta f}(f) = \frac{k_B T f_c}{2\pi k Q x_{\mathrm{rms}}^2} \qquad (1.13)$$

where x_{rms} is the cantilever's RMS amplitude [38, 45]. Unfortunately, surface induced frequency noise often sets the noise floor; this difficulty, and a method to mitigate it will be extensively discussed in Chapter 4.

In MRFM, just as in MRI the spatial resolution comes from exciting magnetic

resonance in a three-dimensional "slice" of the sample determined by the magnetic field, magnetic field gradient, excitation frequency and resonance linewidth. This is very different from most scanned probe techniques where most often it is the size of the probe tip that determines the spatial resolution[46] and the sensitivity is often only to the sample surface. The highest resolution image to date was created by scanning the sensitive slice in three dimensions and reconstructing the image using a nonlinear, iterative Landweber algorithm[35]. Creating an image using this reconstruction technique is not ideal because the reconstruction will introduce artifacts unless the spin density is zero at the image boundaries, limiting the possible samples to finite objects and precluding the study of films or small regions of larger objects (e.g. a whole cell). This is very different from MRI where a linear, SNR preserving Fourier transform is used for image reconstruction[47]. Other imaging protocols that attempt allow for a linear reconstruction and semi-inifinte samples are known, however, to date they are limited to micrometer resolution[48, 49] or remain to be demonstrated in an MRFM experiment[50].

Above the force from a single electron spin was estimated to be a few tens of attonewtons for a realistically sized gradient source. This force is much smaller than can be detected using a commercially available cantilever and a key component of the single electron experiment[28] was developing a cantilever capable of detecting such small forces[51, 52]. However fabricating a sensitive enough cantilever is only part of the challenge, because the cantilever must also have a magnetic tip producing $G \geq 10^6$ T/m while maintaining its force sensitivity near a surface. Ref. 33 and Chapter 3 have demonstrated that an ultrasensitive cantilever with a magnetic tip that overhangs the silicon body of the cantilever successfully maintains $F_{\min} \leq 10$ aN until a tip height of 3 nm. Prior to the experiment presented there, all demonstrations of "scanned probe" (magnet-on-tip) MRFM used a magnetic

tip that was attached to the cantilever by hand [39, 42, 53, 54] and limited to $r_{\text{tip}} \sim 75$ nm by ion damage from focussed-ion beam milling [39, 54, 55]. The cantilever and magnetic tip used in Chapter 3 were fabricated using a challenging batch fabrication protocol [33] that, with further refinement, should be capable of producing magnetic tips with $r_{\text{tip}} \lesssim 35$ nm.

Demonstrating the integrity of the magnetic tip is difficult because it is very small and located on the end of a fragile cantilever. Cantilever torque magnetometry is one of the few techniques that can nondestructively probe the magnetization of the tip, extracting the magnetic moment and anisotropy constant of the magnet[29, 56]. Prior studies of magnetic tipped ultrasensitive cantilevers [56–58] have only observed in-plane switching, however, when operating in the SPAM geometry the magnetic tip is magnetized out of plane assuming the easy axis of the magnetic particle is aligned with the long axis of the cantilever. If operating with a large enough external magnetic field $(B_0 \gg \mu_0 M_{\text{tip}})$, magnetizing the tip out-of-plane does not present any additional concerns. However, the ESR experiments presented here take place at ~ 0.6 T, very near the saturation field for nickel tip and incomplete saturation of the magnetic tip was a significant concern. Cantilever magnetometry can also probe the in-plane to out-of-plane transition.

CHAPTER 2

FORCE-GRADIENT DETECTED ELECTRON SPIN RESONANCE FROM NITROXIDE SPIN PROBES

2.1   Introduction

A generally applicable approach for determining the tertiary structure of an individual macromolecule *in vitro* at angstrom or sub-angstrom resolution would create exciting opportunities for answering many long-standing questions in molecular biology. For macromolecules too large to characterize by NMR or X-ray diffraction, the tertiary structure of proteins [19–21], nucleic acids [22, 23], and biomolecular assemblies [24, 25] can be explored by using inductively-detected electron spin resonance (ESR) to measure distances between pairs of attached spin labels [20–23, 25, 26]. These studies, however, require bulk quantities of sample [27] and demand multiple experiments with spin labels attached to different locations in the target macromolecule. Mechanical detection and imaging of single electron spins has been demonstrated, in E′ centers in gamma-irradiated quartz [28], and it is natural to explore applying magnetic resonance force microscopy (MRFM) [35, 42, 59–61] to map the locations of individual spin labels attached to a single biomacromolecule.

The ultimate limit of imaging resolution in MRFM is set by the intrinsic linewidth of the resonance and the applied magnetic field gradient. For a 0.1 mT homogeneous linewidth, typical of the organic radical studied here, a gradient of 4×10^6 T/m allows selective excitation of individual spin labels only 0.025 nm apart. A magnetic field gradient this large has recently been demonstrated in an MRFM experiment using ferromagnetic pillars fabricated by electron-beam lithog-

raphy [35]. The force sensitivity required to detect single electrons in this gradient is 40 aN, above the minimum detectable force (in 1 Hz bandwidth) of $5 - 10$ aN reported for a high-compliance cantilever operated with its metalized leading edge above a metal-coated surface in high vacuum at $300\,\mathrm{mK}$ [35]. In all high-sensitivity MRFM experiments to date, sensitivity has been limited by interactions of the cantilever with fluctuating electric fields and electric field gradients originating in the sample substrate. Efforts to mitigate this surface noise by fabricating magnetic tips that extend beyond the leading edge of the cantilever are described in Refs. 62 and 63. Careful sample preparation can also help mitigate surface noise, for instance, polystyrene is known to be one of the quietest samples [31, 32, 64] and efforts are underway [65] to use polystyrene beads to improve upon the 4 nm imaging result of Ref. 35.

Before these improvements in sensitivity and resolution can be harnessed to study organic spin labels, a suitable method must be devised for creating a distinguishable spin signal. Unfortunately, organic spin labels do not meet the stringent sample requirements of established mechanical single-spin detection protocols [28]. The force-based i-OSCAR approach, used by Rugar *et al.* to detect single electron spins in quartz [28], requires samples with rotating-frame spin-lattice relaxation times of $T_{1\rho} \geq 0.1\,\mathrm{s}$ to reach single spin sensitivity. At low temperatures we expect nitroxide spin labels to have spin-lattice relaxation times in the range $1\,\mathrm{s} \geq T_1 \geq 1\,\mathrm{ms}$ and $T_{1\rho}$'s of only a few µs [66–68], making signal modulation by i-OSCAR [69] inapplicable. Cyclic adiabatic inversion [35] is likewise inapplicable, since it relies on continuous spin locking meaning the governing relaxation time is still $T_{1\rho}$. Saturating the sample spins cyclicly is another approach to creating a distinguishable signal [41, 70]. To achieve high sensitivity, spin magnetization should be modulated at the cantilever's resonance frequency. Cyclic saturation

thus requires samples with spin-lattice relaxation times less than the cantilever period, $T_1 < T_c$, which would necessitate using cantilevers with impractically low resonance frequencies, given the expected range of T_1 for nitroxides at low temperatures. The force-gradient approach to mechanically detecting spins introduced by Garner *et al.* [42] can in principle be used to create a detectable spin signal from a nitroxide spin label. In practice, however CERMIT has to date [42, 44] only been used to observe magnetic resonance from spins with $T_1 \gg 0.1\,\text{s}$ and, moreover, has relied on adiabatic rapid passage to flip spins and create a distinguishable signal.

Here we introduce an improved force-gradient approach to mechanically detecting magnetic resonance that is applicable to samples — such as nitroxide spin probes — with T_1's as short as ≈ 0.2 ms. We demonstrate the approach by using a magnetic-tipped ultrasensitive cantilever operated at high magnetic field to detect electron spin resonance from a thin-film containing the nitroxide spin probe TEMPAMINE widely used in ESR studies of biomolecules. The expanded force-gradient approach to mechanical detection of magnetic resonance introduced here requires only milligauss microwave magnetic fields to detect ESR from a nitroxide free radical, is well suited to the study of thin-film samples, and is compatible with magnetic-tipped attonewton-sensitivity cantilevers at high magnetic field. The new method is capable of detecting magnetic resonance in samples whose spin-lattice relaxation times are as short as a single cantilever period, extending the lower limit of sample relaxation times that can be detected using force-gradient methods by $\geq 10^2$. Our findings, moreover show that saturation, when married to force-gradient detection, can be used to create a detectable signal even when $T_1 \gg T_c$. This combination of capabilities opens up new avenues for pushing detection and imaging of electron spin resonance from a wide range samples, particularly nitroxide spin probes, towards single spin sensitivity.

2.2 Apparatus

Experiments were carried out in high vacuum, $P \leq 10^{-6}$ mbar, and at liquid helium temperatures, $T = 4.2$ K, in a custom-built probe. The microscope was originally designed and constructed by Kuehn [43] for NMR experiments in either the hang-down or SPAM geometries and contains no provision for lateral scanning. As part of the work described in this thesis the microscope was modified to perform ESR experiments at 17 GHz while maintaining the option of either geometry. These modifications consisted primarily of replacing the sample mounting block and RF tank circuit with a planar microwave resonator and an appropriate mounting block. The probe head was constructed from grade 2 commercially pure titanium machined either in the LASSP machine shop or graduate student machine shop. Coarse and fine tip-sample positioning was carried out using a commercial nanopositioner (Attocube Systems AG, ANPx51/HV/LT) onto which the cantilever assembly was mounted. Fig. 2.1(a) is a sketch of the experiment; the components will be described below.

2.2.1 Cantilever and Displacement Sensor

The central component of the experiment is a high-compliance cantilever [51, 52] (200 µm long, 4 µm wide and 0.34 µm thick) with spring constant $k_0 = 7.8 \times 10^{-4}$ N/m, resonance frequency $f_0 = 4975$ Hz, mechanical quality factor $Q = 1.05 \times 10^5$, and force sensitivity $F_{\min} = 7.5 \times 10^{-18}$ N in a 1 Hz bandwidth at a temperature of $T = 4.2$ K and in a vacuum of $P = 10^{-6}$ mbar. The last 5 µm of the cantilever is only 1 µm wide to facilitate gluing a magnetic sphere to the cantilever end. A nickel sphere of diameter 4µm (Novamet, CNS-10) was affixed to
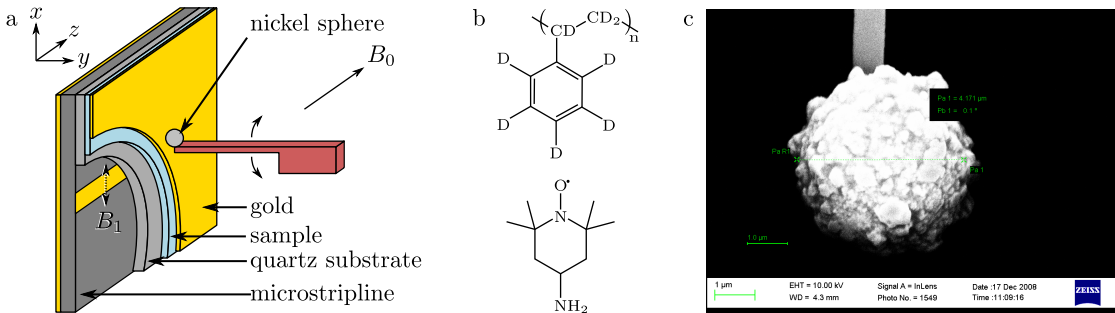
Figure 2.1: (a) Scanned-probe electron spin resonance experiment schematic. A microstripline half-wave resonator delivers a transverse magnetic field, B_1, oscillating at 17.7 GHz. In the center of the resonator, the microwave field oscillates along the x direction. A longitudinal Zeeman field of magnitude $B_0 \approx 0.6$ T is applied along the z axis. The high-compliance cantilever has its long axis along y and oscillates in the x direction. The cantilever's 4 µm-diameter nickel tip was affixed by hand. The sample is a 230 nm-thick film of 40 mM TEMPAMINE in perdeuterated polystyrene, coated with 20 nm of gold. The sample film was spin-coated onto a 250 µm-thick quartz wafer. For clarity, sample and substrate are not drawn to scale. (b) Molecular structures of (top) perdeuterated polystyrene and (bottom) TEMPAMINE. (c) Scanning electron microscope image of the 4 µm nickel magnet. At the top of the image the 1 µm wide narrowed tip of the cantilever can be seen.

this narrow section as follows. A small amount of magnetic powder was dispersed onto a polished brass surface. While observing through an inspection microscope, optical micrometer stages were used to touch the cantilever tip to a small drop of epoxy (Miller-Stephenson 907) and then to an isolated magnetic particle. The anisotropy of these particles is small enough that allowing the epoxy to cure in an applied field to align the magnetic easy axis with the field direction was not necessary [42]. A scanning electron microscopy image of the magnetic particle used in this experiment can be seen in Fig. 2.1(c).

Cantilever motion was detected using the temperature-tuned [71] optical-fiber interferometer [72] described in Ref. 43, briefly summarized here. The optical fiber (9/125 single mode, SMF-28, Corning; Metrotek part #FC/00-016ft-S-S1) passes into the vacuum chamber through an 1/8" Ultra-Torr Swagelok fitting with

15

a custom Teflon ferrule [73]. The optical fiber, sold as "900 µm single mode" by Metrotek, does not have a Kevlar layer between the PVC jacket and the tight inner buffer. We found that, in contrast to to Ref. 73, a helium-tight high-vacuum seal could be formed with this fiber without removing the PVC jacket. When machining a Teflon ferrule a #67 drill (0.032"$\sim$ 813 µm) produced a correctly sized hole to pass the optical fiber. Future instruments should use 1/4" fittings; the Teflon ferrule quickly became irreversibly crushed with an 1/8" Swagelok, a problem which is entirely solved by using a larger fitting.

The interferometer's optical fiber was aimed at a reflective pad (octagonal, 20 µm side-to-side) fabricated 75 µm from the cantilever tip. The cantilever was aligned by hand, using tweezers or dental picks, to the cleaved optical fiber which was epoxied (Stycast 2850-FT, Lake Shore Cryotronics, Inc) to the cantilever mounting block. Once epoxied, the tight inner buffer of a properly prepared fiber extended through approximately half of the 5 mm epoxy covered region. This ensured that that the inner buffer strain relieved the fiber at the attachment point. The cantilever extends only 12.5 µm past the edge of the optical fiber and the epoxy on the upper surface of the optical fiber had to be very thin to ensure that it did not touch the sample surface before the cantilever tip. The distance between the optical fiber and the cantilever was 50–100 µm, determined by the position of the epoxied fiber. Coupling visible light into the optical fiber greatly aided in aligning the cantilever to the fiber. During experiments the cantilever-incident optical power was $P \sim 3\,\mu\text{W}$ at a wavelength $\lambda = 1310\,\text{nm}$, corresponding to $\sim 1\%$ of the laser output. A commercial photodetector (New Focus, model 2011) was used. The detected motion at the octagonal pad was smaller than the motion of the cantilever tip. Modeling the cantilever as a singly clamped beam of rectangular cross section, we estimate that the tip deflection is 2.02 times larger than the

detected motion [74].

The cantilever's spring constant was determined by observing thermomechanical position fluctuations [75]. The power spectrum of a 20 s record of cantilever position was calculated and $n_{\mathrm{avg}} = 50$ such spectra were averaged together. The averaged position power spectrum was fit to

$$P_{\delta x}(f) = P_{\delta x}(0)\frac{f_0^4}{(f^2 - f_0^2)^2 - f^2 f_0^2/Q^2} + P_{\delta x}^{\mathrm{det}} \qquad (2.1)$$

where the first term is the spectrum of position fluctuations for a underdamped harmonic oscillator and $P_{\delta x}^{\mathrm{det}}$ is a white background from the finite sensitivity of the displacement sensor. The spring constant was determined from the fit parameters $P_{\delta x}(0)$, f_0, and Q using

$$k_0 = \frac{2k_B T}{\pi P_{\delta x}(0) Q f_0}. \qquad (2.2)$$

In order to estimate errors in the fitted parameters, we made the ansatz that the standard deviation in the power spectrum was $P_{\delta x}(f) \times n_{\mathrm{avg}}^{1/2}$ [64, Supplemental Information]. The cantilever's quality factor was calculated from the measured $1/e$ ringdown time τ using $Q = \pi f_0 \tau$. The Q found from fitting the position fluctuation power spectrum was always smaller than the Q found from the $1/e$ time. The Q was identical if measured on a positive-going or negative-going interferometric fringe, indicating that the observed Q is not being reduced or enhanced by photothermal feedback [76, 77].

2.2.2   Frequency Determination

To measure the cantilever frequency and determine frequency shifts, the cantilever was driven into self-oscillation via a piezo mounted at the cantilever base using a fixed-gain positive feedback loop, [38] the interferometer output digitized, and
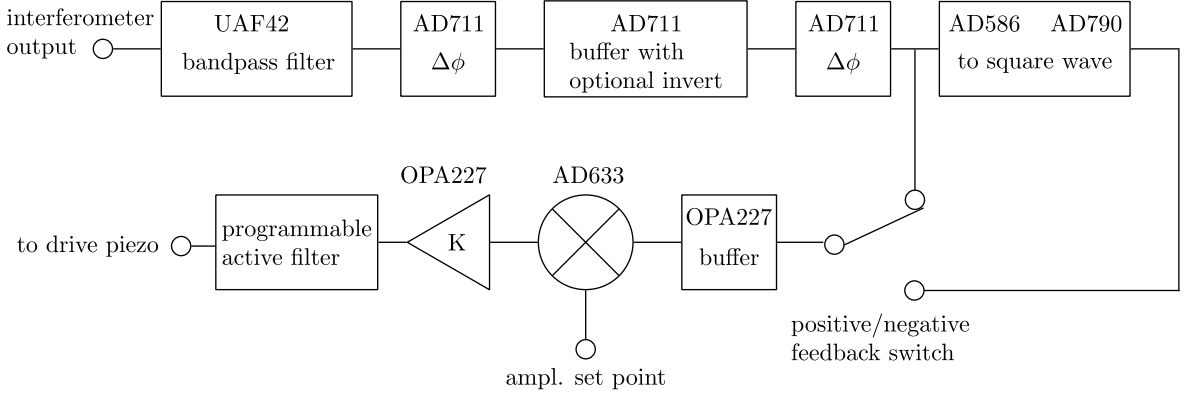
Figure 2.2: Block diagram of the feedback circuit. The circuit was constructed on a solderless breadboard and driven using two 12 V batteries. The part numbers of the integrated circuits used to built the feedback circuit are indicated at the top of each element. The final programmable active filter is a independent instrument and could easily be replaced with a second UAF42 filter.

the resulting signal fed into a high-bandwidth software frequency demodulator [64]. The custom-built feedback loop could provide positive feedback for frequency shift measurements or negative feedback for amplitude measurements. A block diagram for the feedback loop is shown in Fig. 2.2. The feedback circuit operated as follows. The input signal was filtered using a $Q = 0.625$ pass-band filter centered at the cantilever's resonance frequency and built around a active filter IC (UAF42, Texas Instruments Inc.) used in the inverting pole pair configuration. Following the filter, the signal was phase shifted using the op-amp circuit shown in Fig. 2.3. This circuit is an all-pass filter with (as implied) magnitude response of $|G(i\omega)| = 1$ and a phase response of

$$\arg G(i\omega) = \tan^{-1} \frac{2\omega R_p C}{(\omega R_p C)^2 - 1} \tag{2.3}$$

where, as implemented $R = 10\,\text{k}\Omega$, $C = 0.01\,\text{µF}$, and the potentiometer R_p covers the range 0–10 kΩ. Two copies of this circuit were used in the feedback circuit to provide a larger range of phase shifts. The phase shifters were followed by a voltage follower which could optionally invert the signal, controlled by a switch on the front panel. When the circuit was used in positive feedback mode, the

18

filtered and phase shifted signal was converted to a TTL level square wave using a comparator (AD790, Analog Devices, Inc.) whose output level was set by a precision 5 V reference (AD586, Analog Devices, Inc.). In negative feedback mode the comparator was bypassed using a switch on the front panel. The strength of the feedback was controlled by multiplying the signal by an externally supplied voltage using an analog multiplier (AD633, Analog Devices Inc.). The external voltage was usually produced using one of the auxiliary DC voltage outputs from a lock-in amplifier (SR830, Stanford Research Systems Inc.). Further gain, $1 \leq K \leq 10$, was applied using a non-inverting amplifier built around a single op-amp (OPA227, Texas Instruments, Inc.). Before being sent to the drive piezo, the feedback signal was filtered using a tunable active filter (model 3940, Krohn-Hite Corp.). The feedback circuit provides a copy of the TTL level square wave for external use. The TTL level copy was fed into a universal counter (SR620, Stanford Research Systems Inc.) for real time frequency determination, used as a lock-in reference, and used as a clock to provide cantilever synchronized microwave pulses. The correct phase shift can be determined by a lock-in amplifier measurement, however, adjusting the potentiometers controlling the phase shift to produce the largest possible amplitude was sufficient to correctly phase the feedback. It was not necessary to adjust the center frequency of the initial filter when changing cantilevers because the resonance frequency of all of the cantilevers used fall with 4–9 kHz, a small enough range to be covered by a single set of filter coefficients.

The software frequency demodulator uses a frequency demodulation algorithm based on the Hilbert transform [78–80] that also provides the instantaneous amplitude. To demodulate a signal $s(t)$, here assumed to be narrow band, the analytic signal associated with s is computed. The analytic signal is a unique complex signal, $z(t) \equiv s(t) + i\mathcal{H}[s(t)]$, where $\mathcal{H}[\,]$ is the Hilbert transform. The Hilbert
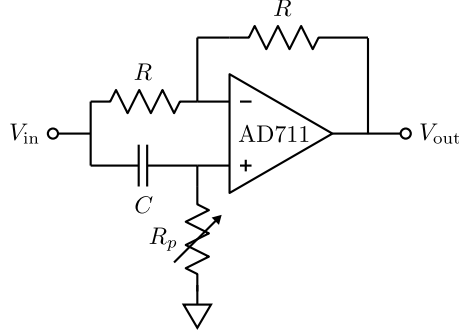
Figure 2.3: Schematic for the all-pass variable phase shifter. As implemented in the feedback circuit, $R = 10$ kΩ, $C = 0.01$ μF, $R_p = 0$–10 kΩ, and as indicated in the schematic, it is built around an AD711 op-amp.

transform is defined as

$$\mathcal{H}[s(t)](\tau) = \frac{1}{\pi} P \int_{-\infty}^{\infty} \frac{s(t)}{t - \tau} dt \qquad (2.4)$$

where the P indicates that the Cauchy principal value is taken. Practically, this integral transform takes $\sin t$ to $\cos \tau$ and $\cos t$ to $-\sin \tau$. In the Fourier domain the Hilbert transform can be carried out by multiplying by

$$H(f) = \begin{cases} +i & \text{if } f < 0 \\ 0 & \text{if } f = 0 \\ -i & \text{if } f > 0 \end{cases} \qquad (2.5)$$

If $z(t)$ is recast into a polar representation, $z(t) = a(t)e^{i\phi(t)}$, the utility becomes clear. The instantaneous amplitude and phase of $s(t)$ are the modulus and argument, respectively of $z(t)$. The instantaneous frequency, $f(t)$ of $s(t)$ is

$$f(t) = \frac{1}{2\pi} \frac{d\phi(t)}{dt} \qquad (2.6)$$

The polar representation of $z(t)$ also demonstrates that the Fourier transform of $z(t)$ is one-sided and contains only positive frequencies.

Our implementation of this frequency demodulation algorithm operates as follows and is shown pictorially in Fig. 2.4. First, the discrete Fourier transform of the

20
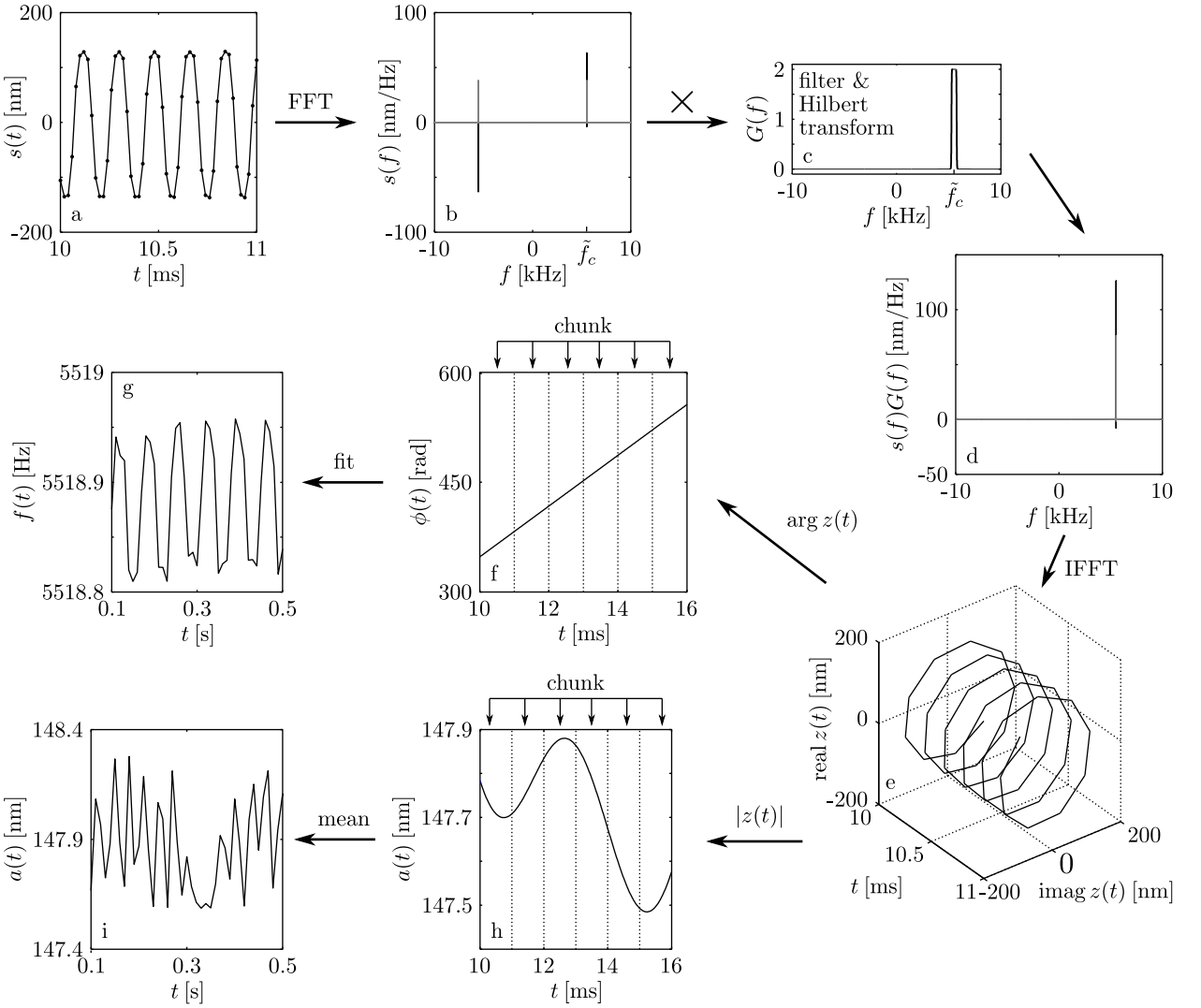
Figure 2.4: Pictorial description of the frequency demodulation algorithm. The digitized trace of cantilever motion (a) is Fourier transformed, (b). The resulting spectrum consists of narrow band signals at $\pm f_c$. The spectrum is filtered and converted to the Fourier transform of the analytic signal by multiplying by (c). The resulting spectrum, (d), is one sided. The inverse Fourier transform of a one sided narrow band spectrum is a complex exponential, (e). The argument of $z(t)$ is the cantilever's phase, $\phi(t)$, (f), which is very nearly linear after the phase discontinuities introduced by the arctangent have been removed by phase unwrapping. $\phi(t)$ is divided in to chunks, here 1 ms in length, which are individually fit using linear least squares regression. The slope of each chunk is an estimate of the instantaneous frequency, $f(t)$ during that chunk, (g). Here $f(t)$ is frequency modulated at $f_{\mathrm{mod}} = 14.4\,\mathrm{Hz}$ due to spin-tip interactions as described in this chapter. The modulus of $z(t)$ is the cantilever's amplitude, $a(t)$, (h), which is divided into chunks as in (f). The mean of $a(t)$ during each chunk is computed, producing the down-sampled estimate of the cantilever's instantaneous amplitude, (i).

21

digitized interferometer output is computed and the average cantilever frequency, $\tilde{f}_c$ estimated as the (positive) frequency with the largest Fourier amplitude. This estimated frequency is used as the center frequency for bandpass filtering which is carried out in the Fourier domain by multiplying by

$$G(f) = \frac{2}{1 + \left((f - \tilde{f}_c)/b \right)^{20}} \tag{2.7}$$

where b is a specified bandwidth. This filtering function is a shifted version of the magnitude of the frequency response of a 10th order Butterworth filter [81]. The function $G(f)$ only passes positive frequencies and thereby simultaneously restricts the bandwidth and performs the Hilbert transform. The inverse Fourier transform is taken, producing the analytic signal. The modulus, $a(t)$ and argument, $\phi(t)$ of the analytic signal are divided into chunks where $T_{\text{chunk}} = 1/f_{\text{out}}$ and f_{out} is the sampling frequency of the output instantaneous frequency. For each chunk, the instantaneous frequency is found by extracting the slope of $\phi(t)$ using linear least squares regression and the instantaneous amplitude is found by taking the mean of $a(t)$.

Before carrying out the MRFM experiments described below, we investigated the cantilever frequency noise experienced at small tip-sample separations by the specific magnet tipped cantilever and gold-coated sampled used below. While the cantilever was self-oscillated to an amplitude of $x_{0\text{p}} = 330\,\text{nm}$ as described above, the cantilever position was recorded for 25 s intervals and the instantaneous frequency calculated. Power spectra were computed from these frequency traces; $n_{\text{avg}} = 25$ power spectra at each tip-sample separation were averaged together to give the spectra plotted in Fig. 2.5. At the largest tip-sample heights the low-frequency cantilever frequency fluctuations are limited by thermal fluctuations consistent with a cantilever temperature $T = 4.2\text{K}$ [38, 64]. As the cantilever is

approached toward the surface, low frequency surface induced frequency fluctuations begin to grow in. At the closest tip-sample spacings used, the surface induced frequency noise sets the noise floor for our measurements.

Earlier experiments in the Marohn lab using ultrasensitive cantilevers used longer, $L = 400\,\mu m$ cantilevers with correspondingly lower resonant frequencies $f_0 \approx 2.2\,kHz$ and spring constants $k_0 \approx 55\,\mu N/m$ [42, 43, 52]. Unfortunately when a long cantilever was mounted on our commercial nanopositioner, we were unable to measure thermally limited frequency noise. The literature provided by the nanopositioner manufacturer indicated that the nanopositioner had a mechanical resonance near 2 kHz. We hypothesized that using a cantilever with a similar resonance frequency to the nanopositioner was the cause of the excess frequency noise. To test this hypothesis we mounted the long cantilever to a solid block in the probe, cooled to $T = 4.2\,K$ and repeated the frequency noise measurements. With the cantilever on a rigid mount, the low-frequency frequency fluctuations we observed were consistent with the cantilever temperature, indicating that mounting the long cantilever on the nanopositioner was the source of the excess frequency noise. In a further experiment using a shorter $L = 200\,\mu m$ cantilever with unloaded resonance frequency $f_0 = 9\,kHz$ mounted on the nanopositioner, we were able to observe thermally limited frequency noise, presumably due to the incommensurate resonance frequencies. Following these measurements, all of the experiments described in this thesis used the shorter, $L = 200\,\mu m$ cantilevers.

2.2.3 Microwave Resonator and Electronics

A gap-coupled half wave microstripline patch resonator [82, 83] was used to provide the oscillating transverse field. The microstripline transmission line geometry
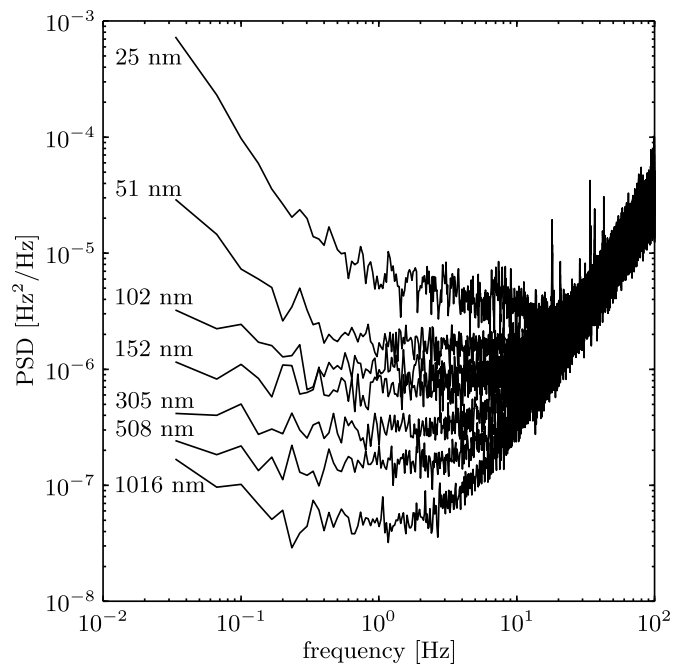
Figure 2.5: Cantilever frequency power spectra for a series of tip-sample heights. At high frequencies the power spectra are dominated by detector noise and proportional to f^2. At lower frequencies and large tip-sample heights, the magnitude is set by the mechanical properties and the temperature of the cantilever. At the smallest tip-sample heights, surface-induced noise is the dominant source of cantilever frequency noise.
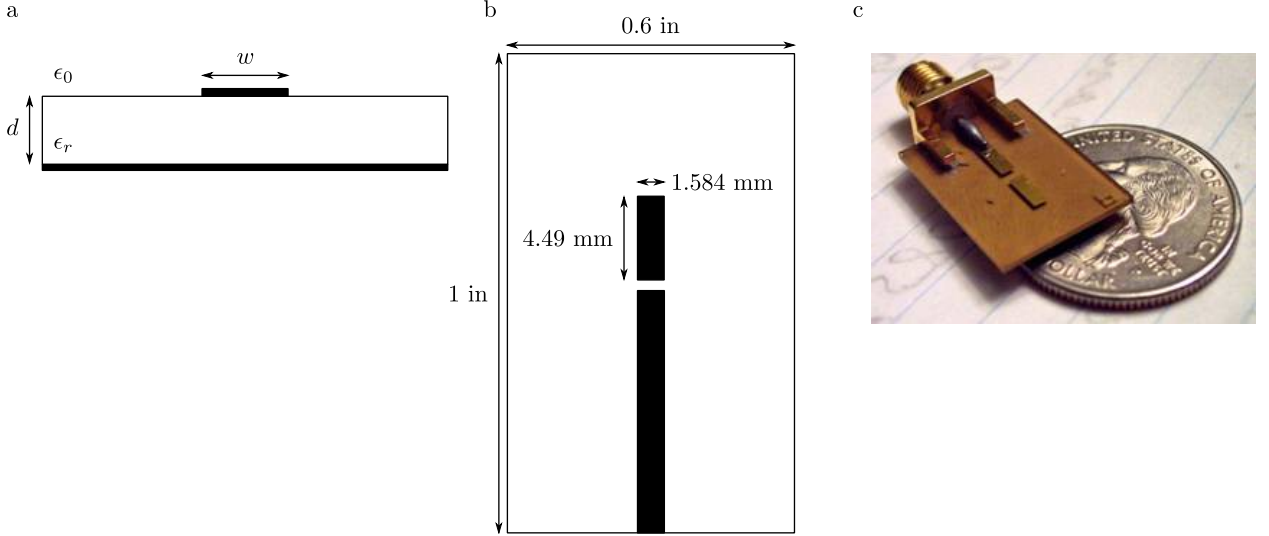
Figure 2.6: (a) Cross sectional view of a microstripline consisting of a dielectric substrate (white) with dielectric constant ϵ_r and thickness d, a ground plane (gold or copper, black) covering the bottom of the substrate and a strip conductor of width w on the top of the substrate. The thickness of the ground plane and top strip are not to scale. (b) Top view of the microstripline resonator. The substrate dimensions, $0.6\,\text{in} \times 1\,\text{in}$ are set by the microscope. An end-launch SMA connector is attached (not shown) to the bottom edge of the substrate, connecting to the short launch line that is coupled though the gap to the resonator patch. (c) A photo of a first generation microstripline resonator on quartz.

consists of a thin strip conductor on top of a dielectric substrate with a conductive plane below; a cross section of such a transmission line is shown in Fig. 2.6(a). The lowest order mode supported by this transmission line is a quasi-TEM wave. Exact analysis of this structure is complicated by the finite dimensions of the strip and the two dielectric constants. However, approximate design equations are known and vary between authors [84–86]; we used the design equations found in Ref. 85.

The impedance of the microstripline in ohms is

$$Z_0 = \frac{377}{\sqrt{\epsilon_{\text{eff}}}} \left(\frac{w}{d} + 1.98 \left(\frac{w}{d} \right)^{0.172} \right)^{-1} \tag{2.8}$$

where w and d are the width of the strip and the thickness of the substrate, respectively, and ϵ_{eff} is an effective relative dielectric constant for the entire dielectric/air

system, equal to

$$\epsilon_{\text{eff}} = 1 + \frac{\epsilon_r - 1}{2}\left(1 + \frac{1}{\sqrt{1 + 10d/w}}\right). \tag{2.9}$$

Initially, our microstripline resonators were fabrication on $d = 750\,\mu\text{m}$ thick quartz (University Wafer) with $\epsilon_r = 3.8$. Using these values and an impedance of $Z_0 = 50\,\Omega$ in Eqs. 2.8 and 2.9 we calculated a strip width $w = 1.584\,\text{mm}$.

A patch antenna or resonator is formed by terminating the microstripline and placing an electrically floating patch a short distance away, as shown in Fig. 2.6(b). The capacitance between the end of the transmission line and the patch will couple electromagnetic waves into the patch and its size and shape will determine the frequency of the resonator. The simplest version of such a resonator has the same width as the microstripline, as shown in Fig. 2.6(b), but in principle the patch can take other shapes. Our patch had the same width. When the effective electrical length of the patch is equal to a integer multiple of $\lambda/2$, the patch will resonate. Knowing the desired resonance frequency, f_{mw} of the first resonance, the length of the patch must be

$$l = \frac{1}{\sqrt{\epsilon_{\text{eff}}}}\frac{\lambda}{2} - \Delta l \tag{2.10}$$

where $\lambda = c/f_{\text{mw}}$ and c is the speed of light in a vacuum, and $\Delta l \sim 0.3\,\text{mm}$ is a small frequency dependent correction to the physical length due to the fringing fields at the open end of the resonator. The MRFM experiment does not depend on a carefully tuned and matched resonator of a precise frequency and further refinement of these values by, for instance finite element modeling, was not done at this time. For a design frequency of $f_{\text{mw}} = 17\,\text{GHz}$ on quartz, the resonator had $l = 4.49\,\text{mm}$.

The initial resonators on quartz were fabricated using optical lithography, electron-beam evaporation, and liftoff to produce 200 nm thick gold layers. An

end-launch SMA connector (Johnson Components, part #142-0701-881) was used to connect the resonator to the microwave source. Fig. 2.6(c) is a photograph of one of the resonators.

There were two problems with fabricating resonators this way. One, soldering by hand to a 200 nm thick gold film on quartz was extraordinarily difficult to do without burning holes in the film and two, the quartz substrates were not particularly robust under even moderate loads, leading to broken resonators while assembling the microscope. Despite these problems working resonators were fabricated and used in the initial experiments.

To address the problems experienced with resonators fabricated on quartz substrates, the resonator used to collect the data shown in this chapter was fabricated on FR-4, a standard epoxy and fiberglass composite printed circuit board material. FR-4 substrates (Injectorall, PC40, 1/32 in thick) were purchased with 1 oz/ft^2 copper cladding on both sides. The dielectric constant for FR-4 is manufacturer dependent and to determine the microstripline dimensions on FR-4 we assumed a dielectric constant of $\epsilon_r = 4.4$. The resonator was 5.6 mm long and 1.4 mm wide. To define the transmission line and resonator on the top side, an appropriately sized pattern was printed out, and the border of the transmission line cut into the copper cladding using a razor blade knife. To make an etch mask, the areas of copper to keep were colored-in several times using a sharpie marker. The excess copper was etched using a saturated warm ferric chloride hexahydrate (FeCl$_3$-6H$_2$O) solution. The gap defining the resonator was created after etching by taking one pass with a razor blade. The same model of end launch SMA connector as was used with the quartz substrates was used with the FR-4 resonators. Soldering to the FR-4 exhibited none of the problems experienced with thin gold

films, since the copper cladding was $\sim 34\,\mu m$ thick and could handle the heat load without delaminating.

Microwaves were supplied by a Wiltron (now Anritsu) source (model 68147B) borrowed from Dr. Doran Smith of the Army Research Laboratory. Following the source, the microwaves were routed through a high speed switch (American Microwave Corporation, model SWN-218-2DT, option 912) and an amplifier (Narda Microwave West, model DBP-0618N830). The peak power out of the amplifier was approximately 32.5 dBm. This power was attenuated by 8.5 dB by the 4.5 m of cable leading to the resonator.

To provide cantilever-synchronized microwave pulses, the 5 V peak-to-peak square wave produced by the positive feedback circuit was digitally divided down using 12-bit binary counters (CD4040B, Texas Instruments, Inc.) to produce a square wave at the modulation frequency and the pulse repetition frequency. These two waves were AND-gated together and the output used to trigger a pulse/delay generator (Berkeley Nucleonics, model 565) which provided precise control of the pulse duration. This system could maintain cantilever synchronization indefinitely; schemes for cantilever synchronization using only carefully tuned pulse/delay generator settings were found to be more susceptible to unlocking as the cantilever frequency drifted. The pulse/delay generator produced TTL-level pulses which were accepted directly by the microwave switch.

To test the resonators, the reflected power was measured using either a network analyzer (Agilent, 8722ES, 50 MHz–40 GHz) or a lock-in amplifier (Standford Research System, SR830), directional coupler (Krytar model 102020020), and RF power detector (Wiltron model 75KA50). When the resonator was connected by a short length ($\sim 18\,in$) coaxial cable and resting on the table, a strong resonance

near the desired frequency was observed. This testing was used to determine the appropriate size for the coupling gap and for the resonators. On quartz, a gap of 0.1 mm gave the highest Q. Later, when fabricating resonators on FR-4 a much smaller gap was used (25 – 40 µm) and was found to produce a strong resonance. The resonator used in this work had a quality factor of ~ 800 when measured outside of the microscope. Unfortunately, when installed in the microscope, no resonance was observed for resonators on either substrate. The reason why no resonance was observed is not clear.

To attempt to locate the resonance *in situ*, we amplitude-modulated the microwaves at the cantilever resonance frequency, f_0, using a switch and observed the resulting cantilever excitation using a lock-in amplifier with the cantilever located between 100 nm and 10 µm above the sample surface. With this procedure, we identified three resonances: 9.82, 13.79, and 17.99 GHz. Upon cool down the last resonance shifted to 17.73 GHz. Although this procedure was used to select the microwave frequency for this work, it is not clear what is being measured, or that this is the best procedure to select the microwave frequency *in situ*.

2.2.4 Sample Preparation

The sample was prepared by spin casting TEMPAMINE and perdeuterated polystyrene onto a quartz substrate and coating the resulting film with a thin layer of gold. The molecular structure of TEMPAMINE and polystyrene are shown in Fig. 2.1(b). The solution used for spin casting was prepared by dissolving 0.0063 g of of TEMPAMINE (Aldrich, 163945) in 1 mL of d_8-toluene, 0.33 mL of which was further diluted to 1 mL and from that, a 0.1 mL aliquot was added to a solution of 0.039 g perdeuterated polystyrene (Polymer Source, P4179B-dPS, $M_n = 200 \times 10^3$ and
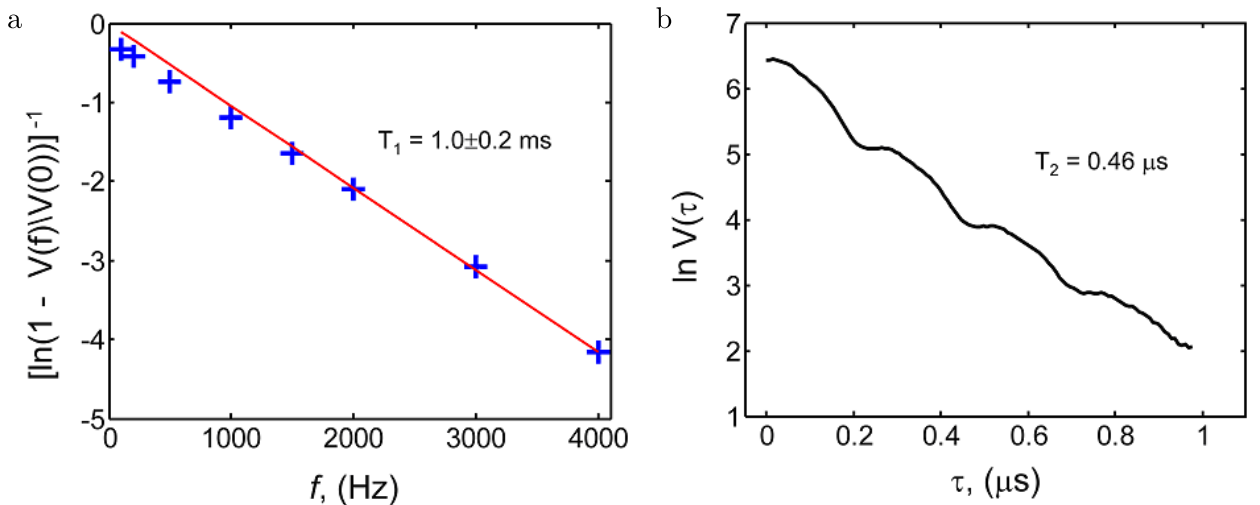
Figure 2.7: Relaxation time measurements of TEMPAMINE in perdeuterated polystyrene by pulsed ESR at $T = 4.16$ K. (a) Primary echo amplitude versus repetition frequency. (b) Primary echo decay.

$M_w/M_n = 1.4$) in 0.9 mL of d_8-toluene. The resulting solution was spun at 2000 rpm for 30 s onto a 250 µm thick quartz chip (NOVA Electronics). Film thickness was determined by profilometry on simultaneously prepared samples. A top coating of 20 nm of gold was electron-beam evaporated in high vaccum onto the chip at a rate of 0.2 nm/s. A small voltage was applied between the cantilever and the gold coating to minimize non-contact friction [31, 32, 87] and surface frequency noise [28, 64]. The wire used to apply the bias voltage was connected to the thin gold layer using silver paint.

Samples for characterization by low temperature inductively-detected pulsed ESR [36, Supplemental Information] were prepared by Sarah Wright as described above, minus the gold, removed from the substrate and inserted into a 2 mm i.d. Suprasil tube. The low temperature pulsed ESR measurents were carried out by Peter Borbat. A two-pulse primary echo sequence was used to measure T_1 and T_2. Figure 2.7(a) is a plot of the primary echo amplitude versus pulse repetition frequency f. The sample T_1 was estimated by fitting the primary echo amplitude

V to [88]

$$V(f) = V(0) \left(1 - e^{-1/(fT_1)}\right) \qquad (2.11)$$

where $V(0)$ is the echo amplitude, measured at a repetition frequency of a few hertz, and T_1 is the spin-lattice relaxation time. From the fit we find $T_1 = 1.0 \pm 0.2$ ms. The $\pi/2$ and π pulses, separated by 250 ns, were of duration 16 and 32 ns respectively. At low repetition rates ($< 500\,\text{Hz}$) the data deviates from a simple exponential dependence, as one would expect for this temperature. The 20% uncertainty in T_1 mostly originates from a small background impurity signal that was present in the resonator at the time of the measurements. The sample T_2 was determined to be 460 ns from the primary echo decay, Fig. 2.7(b), using 45/90 ns pulse widths. Instantaneous diffusion [89] was only a very minor effect, due to suppression by a fast spin flip-flop rate, which apparently was a major source of the short T_2 found.

2.3   Measurements

The cantilever was brought over the thin-film sample, located in the x-z plane of Fig. 2.1, with the long axis of the cantilever along the y axis such that the cantilever oscillated in the x direction. A static magnetic field, from a superconducting solenoid, was applied along the z direction, parallel to the width of the cantilever [29, 42]. We applied the field along the width of the cantilever in order to mitigate damping of the cantilever arising from tip-field interactions [53]. The microwave magnetic field from the microstripline resonator oscillates in the x direction.

We detect small shifts in the cantilever frequency due to spring constant changes arising from spin-tip interactions. In the experimental geometry of Fig. 2.1, sample

spins interact with the magnetic tip of the cantilever to shift the mechanical spring constant of the cantilever by an amount

$$\Delta k_{\mathrm{m}} = \sum_j \mu_{z,j} \frac{\partial^2 B_z^{\mathrm{tip}}}{\partial x^2} \tag{2.12}$$

where $\mu_{z,j}$ is the z-component of the magnetic moment of the j-th spin in the sample and $G' \equiv \partial^2 B_z^{\mathrm{tip}}/\partial x^2$ is the second derivative of the tip field's z component, B_z^{tip}, with respect to the oscillation direction x. The sum is over all spins in the sample. To create a distinguishable signal, we flip spins in a region below the tip via magnetic resonance. To achieve these spin flips, we turn on the microwave field, in synchrony with the cantilever oscillation, for a half cantilever period every few periods (Fig. 2.8). Spins at a certain distance from the tip are partially saturated and this "saturated slice" is swept through the sample to create a region of diminished electron spin magnetization. The location of the saturated slice is determined by the microwave frequency, the tip magnetization, the tip-sample separation, and the static field. The microwave field is turned off for $n - 1/2$ cycles, during which time the saturated-slice magnetic moment μ^{res} recovers towards equilibrium. During these n cycles the cantilever receives a phase kick of

$$\Delta\phi \approx \frac{\pi f_0}{k_0} \mu_z^{\mathrm{res}} G' \int_0^{nT_{\mathrm{c}}} e^{-t/T_1} \, dt \tag{2.13}$$

$$= \frac{\pi f_0 \, \mu_z^{\mathrm{res}} G' \, T_1}{k_0} (1 - e^{-nT_{\mathrm{c}}/T_1}) \tag{2.14}$$

where T_{c} is the cantilever period, T_1 is spin-lattice relaxation time (assumed the same in each saturated slice), and where we assume that $\Delta k_{\mathrm{m}} \ll k_0$ (valid here). After n cycles the microwave field is reapplied and the slice's spin magnetization resaturated. As a result of the repeated saturation, the cantilever's frequency change is approximately

$$\Delta f_c \approx \frac{1}{2\pi} \frac{\Delta\phi}{nT_{\mathrm{c}}} \approx \frac{f_0}{2k_0} \times \mu_z^{\mathrm{res}} G' \tag{2.15}$$
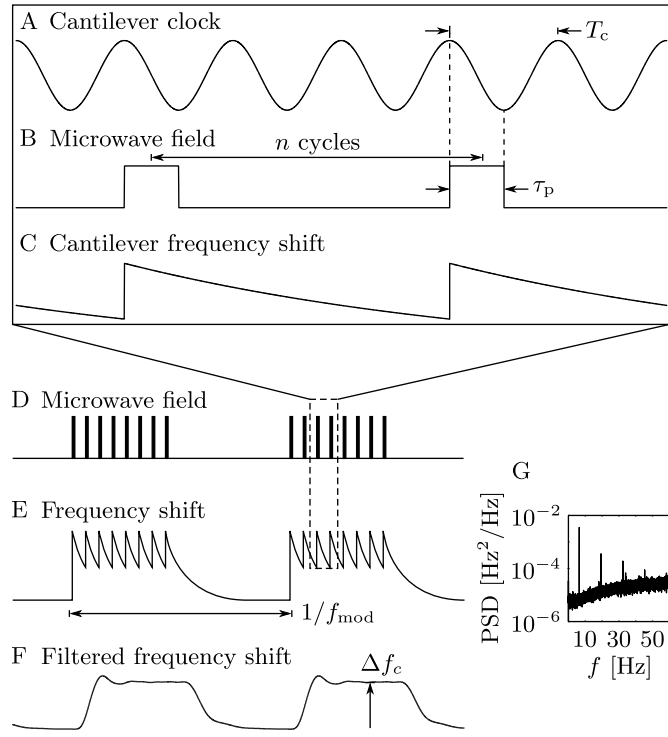
Figure 2.8: Protocol for force-gradient detection of $T_1 \sim 1\,\text{ms}$ spins. (A) The cantilever is self oscillated at its mechanical resonance frequency (4975 Hz; cantilever period $T_c = 201\,\mu\text{s}$) to an amplitude of $x_{\text{rms}} = 233\,\text{nm}$. When the cantilever is at its maximum positive displacement, a microwave switch (B) is turned on. The applied microwave field (partially) saturates the sample's electron spins, which relax over a few cantilever cycles. The microwave field remains on for a half of a cantilever period, $\tau_p = T_c/2 \approx 100.5\,\mu\text{s}$, during which time a region or "slice" of partially-saturated spin magnetization is swept out in the sample. (A series of short pulses are used to minimize sample heating, a single long pulse is also effective.) This sample magnetization interacting with the second derivative of the cantilever's tip field shifts the mechanical frequency (C) of the cantilever. The microwave field is reapplied, in synchrony with the cantilever oscillation, every few (n) cycles. (D) This procedure is repeated for approximately 77 ms, followed by a 77 ms period during which no microwave field is applied. (E) The resulting modulation of the cantilever frequency contains components at the pulse frequency, however we are sensitive only to the slower modulation (F) within the demodulation bandwidth $\sim 60\,\text{Hz}$. The on-off cycling of the microwave pulses introduces a modulation of the cantilever frequency at f_{mod}. (G) The cantilever frequency power spectral density versus frequency under the scheme of (A–F). The largest peak is at $f_{\text{mod}} = 6.48\,\text{Hz}$. The modulation is well approximated by a square wave and higher odd harmonics of f_{mod} are also visible.

when $nT_\mathrm{c} \ll T_1$, which will be approximately the case here.

To more easily detect this tiny frequency shift, the shift is modulated at frequency $f_\mathrm{mod} \approx 6.48$ Hz. This modulation is achieved by turning on and off the microwave field every $\sim 1/2f_\mathrm{mod}$ seconds, again in synchrony with the cantilever oscillation. The cantilever frequency from the demodulator is sent to a software lock-in amplifier operating at reference frequency f_mod. The modulation is a square wave of amplitude Δf_c, resulting in a lock-in output whose primary frequency component has a root-mean-square amplitude of $\delta f_c = \sqrt{2}\Delta f_c/\pi$.

A plot of δf_c versus longitudinal field B_0 is shown in Fig. 2.9 for various tip-sample separations. The peak at field B_b occurs near the Larmor frequency of $B^\mathrm{res} = f_\mathrm{mw}/\gamma_e = 0.63$T and its location is independent of tip-sample separation; this peak we assign to a "bulk" resonance in which the tip magnet is coupled to a large number of spins far away from the tip. The signal peak at field B_c is from spins seeing a tip-field opposing the longitudinal field. Assuming a tip magnetization of $\mu_0 M_\mathrm{tip} = 0.6$ T as expected for nickel, a tip field of approximately $-\mu_0 M_\mathrm{tip}/3 = -0.2$T is expected for spins directly below a spherical tip at small tip-sample separation. These spins require a longitudinal field of $B^\mathrm{res}+0.2$T ≈ 0.8T to achieve resonance, in rough agreement with field value B_c. We assign the peak at field B_c as due to a "local" signal — a relatively small number of spins in resonance directly below the tip. The location of the signal peak at field B_a and the change of signal sign between field B_b and B_c can only be understood by simulating the spins in resonance at a given field and by considering the sign of G' experienced by each spin in-resonance. This analysis requires detailed numerical simulations to be described below.

A worry with detecting magnetic resonance mechanically, particularly of elec-
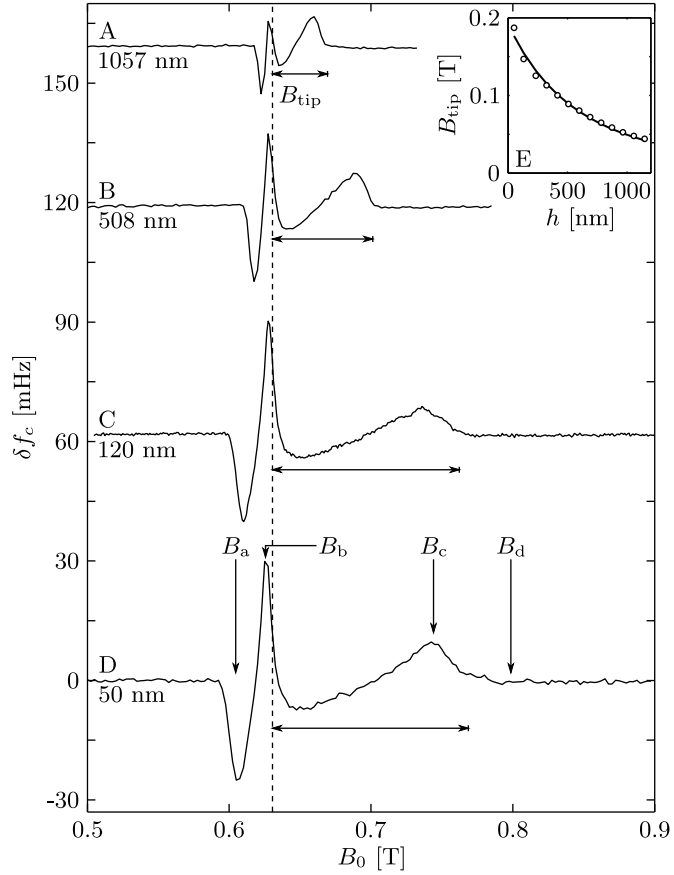
Figure 2.9: Force-gradient detected electron spin resonance from TEMPAMINE, acquired using the protocol of Fig. 2.8 with $n = 3$. (A–D) Fourier component of the cantilever frequency at $f_{\mathrm{mod}} = 6.48\,\mathrm{Hz}$ versus longitudinal field. The signal was acquired with detection bandwidth $b = 0.45\,\mathrm{Hz}$ and microwave frequency $f_{\mathrm{mw}} = 17.7\,\mathrm{GHz}$. The signal was averaged for $10\,\mathrm{s/pt}$ with a field step of $2.5\,\mathrm{mT}$ between each point for (A, B, D) and $0.5\,\mathrm{mT}$ for (C). (E) The tip field B_{tip} (indicated with arrows) was estimated as the separation between $B^{\mathrm{res}} = 0.63\,\mathrm{T}$ and the high field edge of the signal and plotted versus tip-sample separation h. The data was fit to Eq. 2.16 to give a tip radius of $r_{\mathrm{tip}} = 1.85 \pm 0.05\,\mathrm{\mu m}$ and a tip magnetization of $\mu_0 M_{\mathrm{tip}} = 0.44 \pm 0.1\,\mathrm{T}$.

tron spins, is that spin diffusion [90] or thermomagnetic fluctuations in the tip [39, 57, 91] might deleteriously lower the sample's relaxation time. To address these concerns, we measured T_1 mechanically at the same temperature and field as the previously described pulsed ESR measurement.

As indicated by Eq. 2.14 the phase kick that the cantilever receives and thus the magnitude of the frequency shift produced (Eq. 2.15), depends on the ratio nT_c/T_1. An attractive looking way to measure T_1 is to measure the frequency shift as a function of n, the number of cantilever cycles between microwave pulses. This approach is problematic.

At a constant f_{mod}, the background signal varied with duty cycle and therefore n, making it difficult to see the expected exponential dependence of spin signal on pulse delay on top of the varying background. Varying n but keeping the duty cycle constant mitigated this complication, but required either simultaneously varying f_{mod} or using pulse sequences with unequal on and off durations, both of which led to data that was not straightforward to interpret.

A representative data set is shown in Fig. 2.10. This measurement was carried out as indicated in Fig. 2.8 with the time between pulses stepped by one cantilever cycle between each point while the number of pulses in each on-cycle was held fixed. Because of the low-pass filter present in the software frequency demodulator, the measured signal reflects the low-frequency modulation at f_{mod} and not the high-frequency modulation introduced individually by each pulse. When the time between pulses becomes large, the frequency shift seen in Fig. 2.10 decays, we hypothesize, because the smoothed spin-induced cantilever frequency modulation is no longer well approximated by a square wave at f_{mod}.
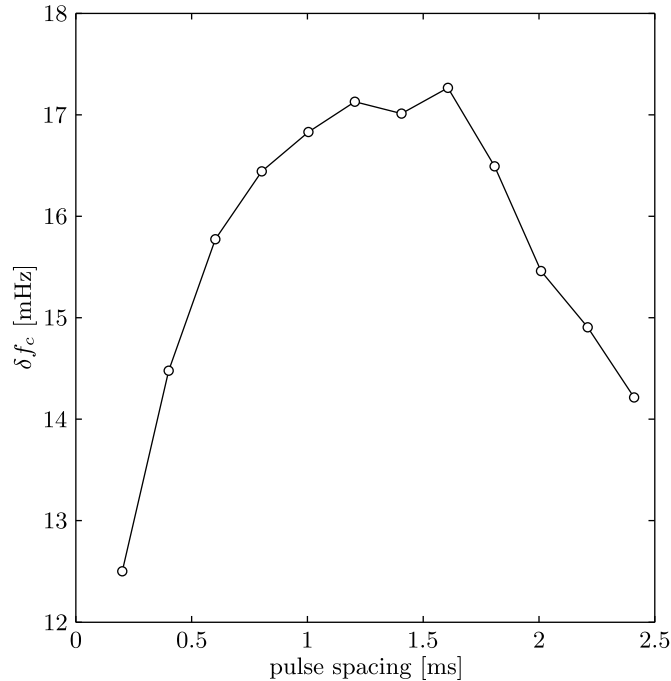
Figure 2.10: A representative frequency shift T_1 measurement. This data is from the peak at field B_b.

To address the difficulties with frequency-based T_1 measurements, a different approach is necessary. We developed an alternative *phase*-based protocol, Fig. 2.11, for measuring T_1 that yielded much cleaner data. Here, as in Fig. 2.8, the microwave field was applied for half of a cantilever cycle to create a region of diminished spin magnetization below the tip. The sample magnetization recovers for $n = 1 - 32$ cycles, during which time the cantilever phase is advanced due to interactions with sample spins by $\Delta\phi$ (Eq. 2.14). Thirty-two microwave pulses are applied and the net phase shift, $\Delta\phi^{\text{tot}} = 32\Delta\phi$, is inferred by comparing the phase before and after the period of microwave irradiation. We limited the number of repetitions to 32 so that the longest irradiation period, $32 \times 32 \times T_{\text{c}} \approx 0.2\,\text{s}$ was much shorter than the cantilever phase memory time (i.e., ringdown time) of $\sim 5\,\text{s}$. Before using this protocol to measure T_1, we fixed $n = 16$ and measured the phase shift versus magnetic field. The results of this measurement are shown in Fig. 2.12
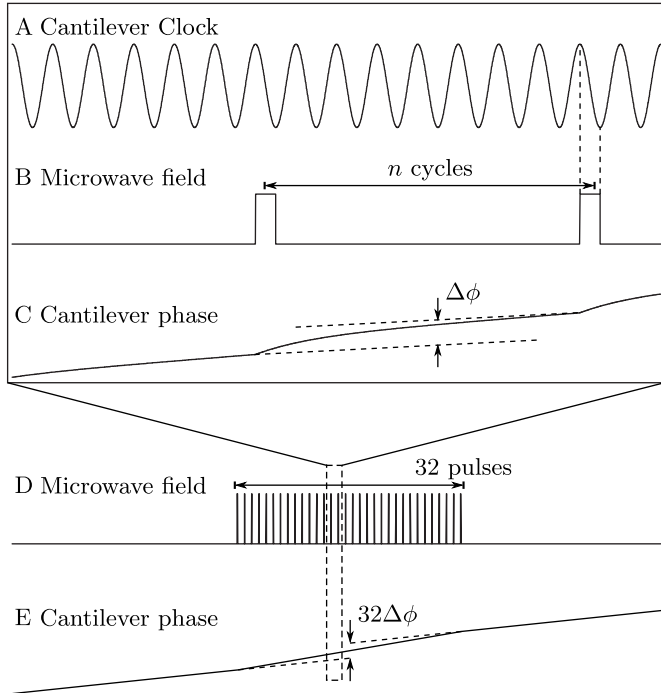
Figure 2.11: Modified force-gradient protocol for measuring the sample spin-lattice relaxation time of $T_1 \sim 1\,\mathrm{ms}$ spins via observation of cantilever *phase* shift. (A) As in Fig. 2.8, the cantilever is self oscillated and the microwave field (B) is turned on for a half cantilever cycle every n cycles to saturate the sample spins. To measure the spin-lattice relaxation time the delay n is stepped from 1 to 32 cycles. The spin-induced cantilever frequency shift leads to a phase shift (C), $\Delta\phi(n)$, which depends on the ratio of the repetition time nT_c to the spin relaxation time T_1. (D) A total of 32 pulses are applied, resulting in a net cantilever phase shift (E) of $32\,\Delta\phi(n)$. The cantilever phase is measured for a time $T_{\Delta\phi}^{\mathrm{acq}} = 0.41\mathrm{s}$, before and after application of the microwave field. The irradiation period was 0.2 s. The two phase-versus-time signals are fit to a line and the spin-induced phase shift computed by comparing the before and after intercepts.
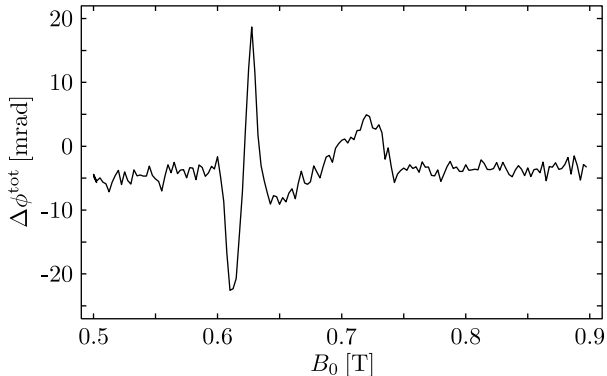
Figure 2.12: Phase-based measurement of the force-gradient ESR signal. For this measurement, $n = 16$, and each point is the average of 10 measurements, in a bandwidth $b = 10\,\text{Hz}$.

and they reproduce the lineshape measure earlier.

The resulting $\Delta\phi^{\text{tot}}$ versus n data are remarkably well described by Eq. 2.14 (Fig. 2.13). Fitting the data quantitatively required adding a small n-independent term to Eq. 2.14 to account for two expected effects: background microwave-induced phase kicks plus a phase advance arising from spin interactions with the cantilever during the half cycle of interaction present even when $n = 1$. The fits are excellent and the T_1 measured for both bulk and local peaks are identical. Moreover, the T_1's measured mechanically agree very well with $T_1 = 1\,\text{ms}$ measured by pulsed ESR.

The finding that $T_1 \sim 1\,\text{ms}$ validates the assumption implicit in Eq. 2.12 that T_1 is longer than the cantilever period of $T_{\text{c}} = 0.2\,\text{ms}$. In order to proceed with numerically simulating the signal of Fig. 2.9, we verified that we were changing sample magnetization by saturation and not, for example, by adiabatic inversion [39, 69]. In Fig. 2.14 we plot the spin signal δf_c versus microwave power P delivered to the microstripline resonator. We can see that both the local- and bulk-peak signals saturate above $P \sim 100\,\text{mW}$. Modeling the spin magnetization using Bloch equations, we fit the data of Fig. 2.14 to $\delta f_c = \delta f_c^{\text{pk}} S/(1 + S)$ with δf_c^{pk}

39
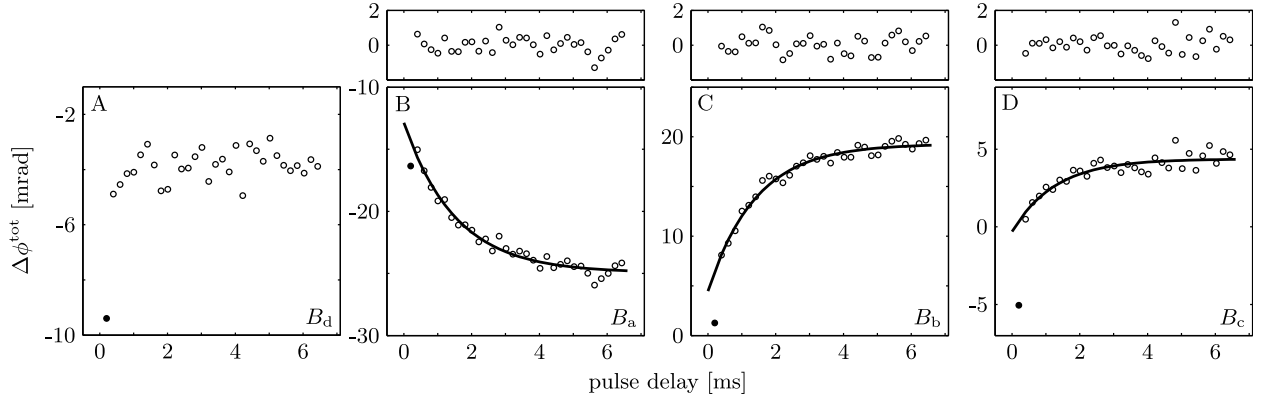
Figure 2.13: Phase-based measurement of sample spin-lattice relaxation time. Cantilever phase shift versus delay time (A) at a field $B_d = 0.8000$ T at which no spins are in resonance and (B-D) at fields B_a, B_b, and B_c (Fig. 2.9). The phase shift data (open circles) were fit to $\Delta\phi^{\mathrm{tot}} = \Delta\phi^{\mathrm{pk}}(1 - e^{-\tau_{\mathrm{d}}/T_1}) + \Delta\phi^{\mathrm{backgnd}}$ (solid line) with $\tau_{\mathrm{d}} = nT_{\mathrm{c}}$ the pulse delay, $\Delta\phi^{\mathrm{pk}}$ the peak phase shift, T_1 the spin-lattice relaxation time, and $\Delta\phi^{\mathrm{backgnd}}$ a background phase kick (see text for details). The phase shift at the $n = 1$ delay was anomalous (filled circles) and excluded from the fits. Fit residuals are displayed on top. The measured spin-lattice relaxation times are $T_1 = 1.41 \pm 0.24$ ms at $B_a = 0.6125$ T, $T_1 = 1.53 \pm 0.29$ ms at $B_b = 0.6275$ T, and $T_1 = 1.27 \pm 0.63$ ms at $B_c = 0.7200$ T. Each point is the average of 25 runs of $T_{\Delta\phi}^{\mathrm{acq}} = 0.41$ s each.
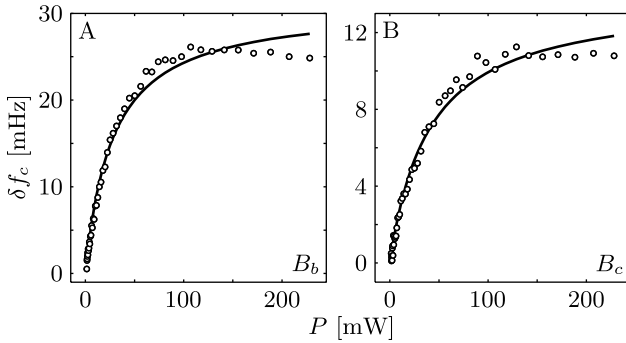
Figure 2.14: The dependence of electron spin resonance signal on microwave power for the (A) "bulk" peak at field $B_b = 0.6275$ T and (B) "local" peak at $B_c = 0.7200$ T. The data was fit to $\delta f_c = \delta f_c^{\mathrm{pk}} S / (1 + S)$ with δf_c^{pk} the peak frequency shift and $S = P c_P^2 \gamma_e^2 T_1 T_2$ the saturation factor, with $T_1 = 1.3$ ms and $T_2 = 450$ ns to give a coil constant of $c_P = 14 \, \mathrm{mG}/\sqrt{\mathrm{W}}$.

the peak frequency shift and $S = P c_P^2 \gamma_e^2 T_1 T_2$ the saturation factor. Here c_P is a "coil constant" relating the power delivered to the microstripline resonator and the magnitude B_1 of the resulting transverse magnetic field; as defined, $B_1^2 = c_P^2 P$. Taking $T_2 = 450$ns from inductively-detected pulsed ESR measurements, we infer a coil constant of $c_P = 14 \, \mathrm{mG}/\sqrt{\mathrm{W}}$. At a given applied power we can now determine the saturation factor S from Fig. 2.14 or, alternatively, from c_P, T_1, and T_2.

To numerically simulate the signal it remains to model the field and the field second derivative from the tip. We estimated the tip diameter and magnetization by studying the signal (δf_c versus B_0) as a function of the tip-sample separation h (Fig. 2.9). At each h, the tip field B_{tip} was estimated from the signal as the difference between the resonance field $B^{\mathrm{res}} = f_{\mathrm{rf}}/\gamma_e = 0.6305$ T and the high-field edge of the local peak. A plot of B_{tip} versus h can be seen in the inset of Fig. 2.9. The tip was modeled as a uniformly magnetized sphere and the data of Fig. 2.9(inset) fit to

$$|B_{\mathrm{tip}}| = \frac{\mu_0 M_{\mathrm{tip}}}{3} \left(\frac{r_{\mathrm{tip}}}{r_{\mathrm{tip}} + h} \right)^3 \tag{2.16}$$

with $\mu_0 M_{\mathrm{tip}}$ the tip magnetization and r_{tip} the tip radius. The observed B_{tip} versus

h is well described by Eq. 2.16 with $\mu_0 M_{\mathrm{tip}} = 0.44 \pm 0.1\,\mathrm{T}$, in reasonable agreement with $\mu_0 M_{\mathrm{sat}} = 0.6\,\mathrm{T}$ expected for the saturation magnetization of nickel. The inferred tip radius $r_{\mathrm{tip}} = 1.85 \pm 0.05\,\mu\mathrm{m}$, is in excellent agreement with $2.0 \pm 0.1\,\mu\mathrm{m}$ estimated from a scanning electron micrograph of the tip, Fig. 2.1(c).

Finally, the signal of Fig. 2.9 was numerically simulated. The tip was modeled as a uniformly magnetized sphere using the measured $\mu_0 M_{\mathrm{sat}}$ and tip radius. The sample approximated as a finite box with dimensions $27\,\mu\mathrm{m} \times 24\,\mu\mathrm{m} \times 0.215\,\mu\mathrm{m}$ divided into $1390 \times 1390 \times 10$ elements. The electron spin density in the sample box was taken to be $\rho_{\#} = 2.41 \times 10^{25}\,\mathrm{m}^{-3}$ as appropriate for a 40 mM TEM-PAMINE sample. B and G' were calculated at each location in the sample box. The z component of spin magnetization was simulated using the steady-state Bloch equations, with the measured T_1, T_2, B_1, and calculated spin density. A magnetization profile was computed with the cantilever at its maximum extension; this profile was translated in the x direction to mimic the cantilever oscillation, and the smallest z magnetization at each grid point retained to mimic the saturated slice. To calculate the spring constant shift, the contribution to Eq. 2.12 from each grid element was computed by multiplying the magnetization profile by the volume and G' and summing over the entire sample. The resulting spring constant shift was scaled by the Curie-Law magnetization, with $B_0 = 0.632\,\mathrm{T}$ and $T = 11\,\mathrm{K}$. The temperature was varied to give good agreement between simulation and experiment. In the experiment, a thermistor measured the temperature near the sample; during microwave irradiation we observed $T \sim 8$ K at this thermistor. The measured temperature agrees well with the simulation temperature given the proximity of the thermistor to the sample and the greater thermal conductivity of titanium, where the thermistor is mounted, over the quartz chip used as a sample platform.
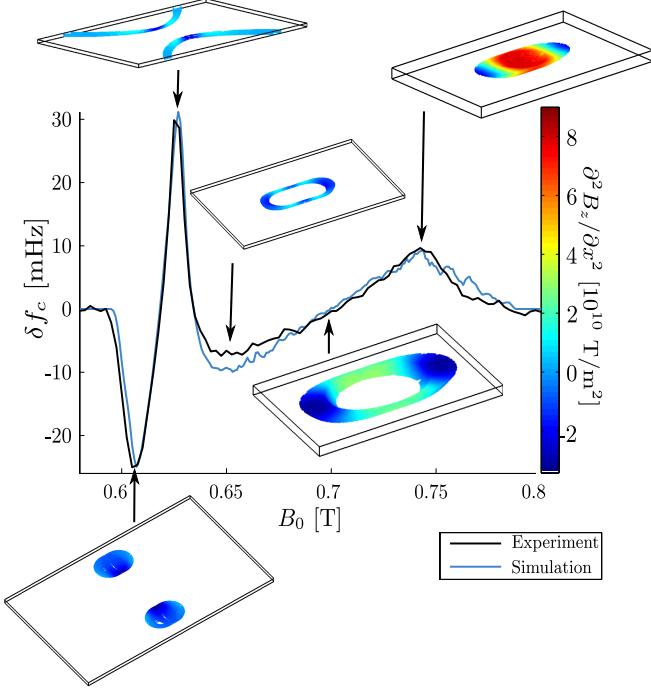
Figure 2.15: Simulation of the frequency shift, δf_c, versus magnetic field for a tip-sample height of 50 nm. The sensitive slice is shown for a selection of field values, colored by the second derivative of the tip field. The simulation is fit to the Fig. 2.9D data using only sample temperature as a free parameter.

The numerical simulation (Fig. 2.15) agrees remarkably well with the observed signal. The simulation properly predicts not only the multiple sign changes in the observed frequency shift as the field is increased but also the correct absolute size of the observed frequency shift. Plotting the spins in resonance at selected fields confirms our assignment of the signal at field B_d as due to spins directly below the tip and helps us understand a number of initially puzzling features of the signal. For example, we can see that the signal goes to zero between fields B_b and B_c because of a cancellation of net G', which can be both positive and negative, when summed over the spins in resonance. We can also see that the signal peak at B_a is indeed due to spins far away from the tip which experience a positive G' and, unlike most spins contributing to the signal, a positive field from the tip.

43
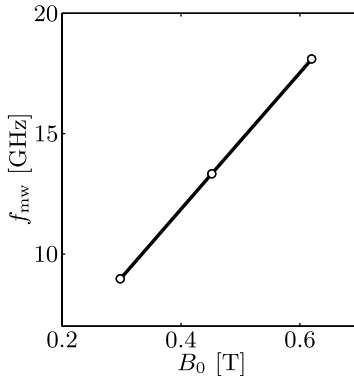
Figure 2.16: Plot of microwave frequency, f_{mw}, versus the location of the B_b peak. The slope of a line fit to the data is proportional to the g factor for the electrons in the sample. From the fit we extract, $g = 2.026 \pm 0.003$. Microwaves frequencies used were 8.99 GHz, 13.33 GHz, and 18.10 GHz.

While the ESR spectrum of TEMPAMINE cannot be observed directly in our experiment because of inhomogeneous broadening of the resonance by the tip field, we can measure the g factor with enough precision to demonstrate that the signal in our experiment is due to unpaired electrons with $g \sim 2.0$. To do this, we applied the microwaves at other eigenfrequencies of our half wave resonator, (present, we conjecture, due to nonidealities in the resonator). A plot of the location of the B_b peak versus microwave frequency is shown in Fig. 2.16. From the slope of the line we infer $g = 2.026 \pm 0.003$. This is not in good agreement with $g = 2.0057$ measured by conventional ESR for TEMPAMINE [92]. The value of g that we measure differs from the accepted value for TEMPAMINE for a number of reasons. The main sources of error are uncertainty in the tip field as the external field is reduced, magnetostriction in the z piezo causing changes in the tip height as the field is changed, a change in tip magnetization during the field ramp, and difficulty extracting the resonance field from the complicated lineshape.

2.4 Discussion

2.4.1 Sensitivity

To estimate the spin sensitivity of our experiment we convert the measured frequency noise to an equivalent spring-constant noise and then use Eq. 2.12 to calculate an equivalent magnetic moment noise, resulting in

$$P_\mu = \frac{4k_0^2 P_{\delta f}}{f_0^2 G'^2} \tag{2.17}$$

The measured frequency noise at height $h = 120$ nm, drive amplitude $x_{\mathrm{rms}} = 233$nm, and frequency offset $f_{\mathrm{mod}} = 6.48$Hz is approximately $P_{\delta f} = 1 \times 10^{-6} \mathrm{Hz}^2/\mathrm{Hz}$ (see Fig. 2.5), 100 times the noise expected from thermomechanical cantilever motion [38, 64]. Spins directly below the tip — those giving rise to the signal at field B_c in Fig. 2.9 — experience the largest G' and therefore couple most strongly to the tip. From the simulations of Fig. 2.15 we infer that G' varies from -1×10^{10} T/m^2 to 8.5×10^{10} T/m^2 for the spins in this slice. Taking the larger of these two values gives a minimum detectable magnetic moment of $\mu_{\mathrm{min}} = (P_\mu b)^{1/2} = 4 \times 10^2 \, \mu_{\mathrm{B}}$ in a $b = 1$ Hz bandwidth.

Another estimate of the sensitivity can be made by counting spins in the B_c-field slice. The total number of spins in the B_c-field slice is 4.22×10^5; weighted by G' at each point, these spins give rise to a frequency shift of 10 mHz. The frequency noise in a 1 Hz bandwidth is 1 mHz, giving a minimum detectable number of (fully polarized) spins in the B_c-field slice of $1.6 \times 10^3 \, \mu_{\mathrm{B}}$. Considering that this second estimate includes contributions from spins weighted by a wide range of G'''s, these two estimates are in reasonable agreement.

This sensitivity is comparable to the 184 μ_{B} sensitivity (in 1 Hz bandwidth)

achieved by Bruland *et al.* [93] who used a magnetic tip similar in diameter to ours, a soft commercial Si_3N_4 cantilever, and cyclic saturation to detect electron spin resonance from DPPH at 77 K. Kuehn *et al.* have shown that force detection (via i-OSCAR) has equivalent signal to noise to force-gradient detection when the tip is adjusted to have amplitude $x_{0p}^c = 0.47 \, (r_{tip} + h)$ [61]. Here $x_{0p}^c = 330$ nm to avoid saturating the interferometer. Setting h to 1 µm to reduce surface noise and using $x_{0p}^c = 1.5$ µm to maximize the sensitivity would improve μ_{min} to $1 \times 10^2 \, \mu_B$, comparable to that achieved in Ref. 93. The detection approach demonstrated here is a significant advance over the Bruland *et al.* experiment because it is compatible with high sensitivity cantilevers oscillating parallel to the surface and works for samples with $T_1 \geq 0.2$ ms, such as nitroxides.

For comparison, conventional ESR microscopy of organic radicals has demonstrated sensitivity [94] of $1.6 \times 10^8 \, \text{spins}/\sqrt{\text{Hz}}$ at room temperature and 34 GHz. It has been estimated that a sensitivity of $2.4 \times 10^4 \, \text{spins}/\sqrt{\text{Hz}} = 10^3 \, \mu_B/\sqrt{\text{Hz}}$ might be achievable at 77 K and 60 GHz [27].

2.4.2 Microwave Performance

When we began this experiment, we intended to perform spin flips via adiabatic rapid passage (ARP) using the technique pioneered by IBM in their OSCAR experiments [39] and used in the first cyclic-CERMIT experiment [44]. To perform an ARP, the effective field, B_{eff}, in the rotating frame begins well below or above resonance and is swept through and then past resonance. If the effective field is swept adiabatically, i.e. slowly enough, the spins will at all times lie along the effective field and the effect of this procedure is to flip the spins. To sweep the effective field either the RF frequency or the external magnetic field can be swept.

In an NMR experiment operating in the RF band with a $0.1 - 50$ ms ARP time, producing the B_{eff} sweep using a frequency chirped RF pulse, as in Ref. 42, is straightforward. Using a frequency chirped pulse becomes increasingly difficult (and expensive) as the pulse length shrinks and the Larmor frequency increases. The insight that enables the OSCAR experiment [39] is that the necessary B_{eff} sweep can be produced using unmodulated RF, the inhomogeneous magnetic field from the magnet tip, and the motion of the cantilever.

Let us estimate how much larger a B_1 would be required to carry out a high-efficiency adiabatic rapid passage using the motion of the cantilever to sweep B_{eff}. To achieve a high-efficiency ARP, the adiabaticity parameter,

$$c_a = \gamma B_1^2 \left(\frac{dB_{\text{eff}}}{dt} \right)^{-1} \tag{2.18}$$

should satisfy $c_a \gg 1$. For an OSCAR-style spin flip $dB_{\text{eff}}/dt = G \times dx/dt$, where $G = dB_{\text{tip}}/dx$ is the first derivative of tip field in the direction of cantilever motion, and x is the coordinate of the cantilever tip. For simplicity consider a spherical tip of radius r_{tip} operating at a height $h = 0$. Surface spins at location $x = r_{\text{tip}}/2$ will see the largest gradient $G \approx 0.29 \mu_0 M_{\text{tip}}$. For a sinusoidally-driven cantilever $x(t) = x_{0\text{p}} \cos(2\pi f_0 t)$, and we estimate

$$c_a \approx \frac{0.55 \gamma B_1^2 r_{\text{tip}}}{\mu_0 M_{\text{tip}} f_0 x_{0\text{p}}}. \tag{2.19}$$

For $x_{0\text{p}} = 163$ nm, $r_{\text{tip}} = 1.85$ µm, $B_1 = 3.9$ mG, $\mu_0 M_{\text{tip}} = 0.44$ T, and $f_0 = 5$ kHz, we estimate $c_a = 6.5 \times 10^{-6}$. A field of amplitude $B_1 \geq 1.5$ G would be required to achieve, $c_a \geq 1$ in our experiment.

We were surprised to find that our coil constant is 260 times worse than that achieved by Wago *et al.* [95] for a similar resonator fabricated on sapphire ($f_{\text{mw}} = 12.6$ GHz). We hypothesized that this comparatively poor performance was likely
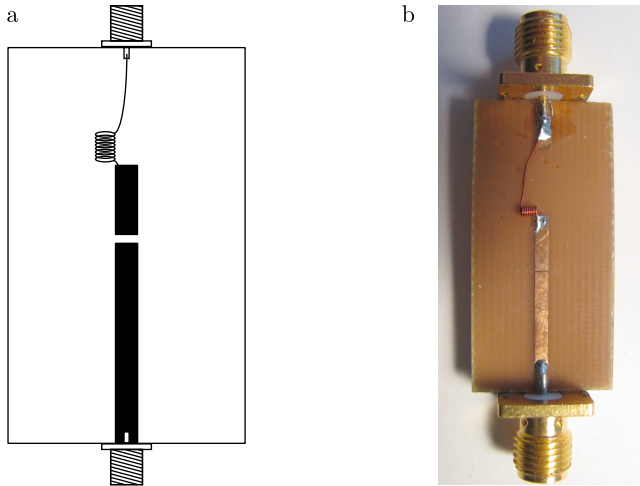
Figure 2.17: (a) Schematic of the microstripline resonator, modified to allow a bias voltage to be applied between the resonator patch and the cantilever tip. (b) Photograph of the device.

due to two factors: not having a well-enough defined electrical ground in our probe (e.g. ground loops) and the metal coating on the sample. Further experiments were undertaken to investigate both of these possibilities. We were nevertheless able to see a signal close to that theoretically possible because our technique requires such a small microwave magnetic field.

For the experiments described in this chapter the ground plane on the MW resonator was in direct contact with the metal body of the microscope. The only other place where the microwave subsystem was connected to the probe body was ~ 4 ft above, where the coaxial cable enters the microscope. Removing the MW subsystem from electrical contact with the body of the microscope, by replacing the coaxial feedthrough and employing a thin FR-4 spacer between the resonator and the probe head, did not improve the microwave performance. This observation seems to rule out ground loops as the cause of the poor resonator performance.

To check if the poor MW performance was due instead to the metal coating on the sample, a different resonator, with similar room temperature *ex situ* per-

formance, was prepared. To minimize the surface noise, an small inductor was wound from 36 gauge copper wire and used to apply a bias voltage to the resonator patch. Because the self-resonance frequency of the coil is so low compared the $f_{\mathrm{mw}} \approx 17\,\mathrm{GHz}$ resonance frequency of the patch, the electrical contact through the coil does not disturb the MW resonance. This modified resonator is pictured in Fig. 2.17. Instead of using a 250 µm thick quartz chip as a sample platform, an identical TEMPAMINE doped perdeuterated polystyrene film was spun directly on the surface of the FR-4 resonator. The coil constant of this resonator, measured as described above was $c_P = 17\mathrm{mG}/\sqrt{\mathrm{W}}$ at $f_{\mathrm{mw}} = 16.79\mathrm{GHz}$ and $c_P = 39\mathrm{mG}/\sqrt{\mathrm{W}}$ at $f_{\mathrm{mw}} = 12.20\,\mathrm{GHz}$. These values are a tiny improvement over the $c_P = 14\,\mathrm{mG}/\sqrt{\mathrm{W}}$ measured above. Furthermore, as above, the resonance vanishes once the resonator is mounted in the microscope.

For comparison let us estimate the coil constant for an untuned microstrip transmission line by assuming that the circularly polarized field above the strip is, in the rotating wave approximation,

$$B = \frac{\mu_0}{2\pi} \frac{I}{w} \tag{2.20}$$

where w is the width of the line. If a current, $I = (P/Z_0)^{1/2}$ flows, the coil constant will be

$$c_P = \frac{\mu_0}{2\pi w \sqrt{Z_0}}. \tag{2.21}$$

Assuming $w = 1.5\,\mathrm{mm}$, we compute $c_P = 188\,\mathrm{mG}/\sqrt{\mathrm{W}}$. This estimated value is a factor of 5 larger than our best measured value and does not include the $\sqrt{Q}$ enhancement expected for a resonator. To check this estimate, we can use it to estimate the quality factor of Wago's resonator [95], and find $Q^{\mathrm{Wago}} = (c_P^{\mathrm{Wago}}/c_P)^2 = (3.6\,\mathrm{G}/\sqrt{\mathrm{W}}/0.188\,\mathrm{G}/\sqrt{\mathrm{W}})^2 = 400$.

To further investigate the poor performance of our microwave resonator, we
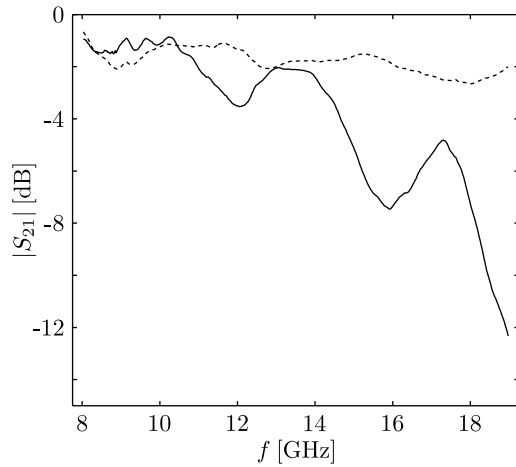
Figure 2.18: Comparison of two styles of end-launch coaxial cable connectors, Johnson Components, part #142-0701-881, used for experiment described in this chapter (solid) and Southwest Microwaves, Inc., part #1492-01A-5 (dashed). For both tests, either end of a ~ 1" length of $50\,\Omega$ microstripline on FR-4 was connected using the same style of connector and the transmission loss, $|S_{21}|$ measured. The Johnson connector is a solder-on connector, rated to 18 GHz, although it becomes quite lossy at high frequencies. The Southwest connector, on the other hand, makes electrical contact without solder, by mechanically clamping onto the substrate, is rated to 50 GHz and exhibits much higher performance in our desired frequency range.

turned to modeling using ANSYS, a commercial finite element package. The simulation predicts a coil constant of $c_P = 0.368\,\text{G}/\sqrt{\text{W}}$ considering a position directly above an untuned microstrip transmission line using the dimensions of our device. This is much better performance than we achieve with a nominally tuned resonant circuit. At this point it was not clear what the problem, was and we elected to attempt to improve the transverse field performance by moving to an untuned line, since simulation indicated that even without a Q enhancement, the achievable B_1 could be two orders of magnitude better than we were currently achieving.

Moving to an untuned transmission line was also inspired by the introduction, in 2007 by Poggio *et al.* of a "microwire" rf source, consisting of a lithographically patterned copper wire, 1 µm wide, 0.2 µm thick and 2.6 µm long that produces $B_1 = 40\,\text{G}$ at 115 MHz while depositing only $P = 350\,\text{µW}$ of heat into their $T = 0.3\,\text{K}$ microscope [96]. This is a coil constant of $c_P \approx 2100\,\text{G}/\sqrt{\text{W}}$ for samples located within 100 nm of the wire. Because the sample volume in an MRFM experiment is of similar dimensions to the microwire itself, having to work with a small wire is an excellent trade off, particularly when operating at low temperatures. The microwire is a broadband RF source [97], however, Poggio's design is limited to frequencies below 200 MHz due to the inductance of the wires used to connect to the microwire chip. Based on the fantastic performance of the microwire at radio frequencies, we began to evaluate extending the concept to microwave frequencies. Although high-efficiency planar microresonators have been developed by several groups for inductively detected ESR [98–100], the MRFM experiment does not depend on the microwave resonator's Q to enhance a small spin induced microwave current and we would prefer to construct a broadband, DC to 20 GHz transverse field source to allow the same device to be used for ESR, NMR, and future dynamic nuclear polarization [101] experiments that would

require applying simultaneous radiofrequency and microwave irradiation.

Initially, we considered a design involving a sub-wavelength constriction in a microstripline [102]. There are better suited waveguide structures, however, such as coplanar waveguide (CPW), where the impedance is nearly independent of the substrate thickness, allowing the lateral dimensions to be scaled down without compromising transmission. A CPW is a planar transmission line consisting of a center strip with two semi-infinite ground planes located parallel to the strip on the same side of the substrate [103]. A principle advantage of this design for our application is that it does not have a ground plane on the bottom of the substrate. A ground plane below puts most of the electric and magnetic fields in the dielectric, between the conductors. However, it is only the magnetic field that extends above the substrate that interacts with the spins; for CPW the magnitude of the microwave magnetic field is nearly the same inside and above the substrate.

In our CPW device, the two ground planes are finite, and only slightly wider than the center strip. Design equations for finite-ground CPW found in Ref. 104 were used to estimate the necessary dimensions for a 50 Ω transmission line. The quartz or FR-4 substrates previously used for microstripline resonators require CPW dimensions that are incompatible with mating to the available end-launch connectors and a substrate with higher dielectric constant is required. Ultra-high resistivity silicon ($\epsilon_r = 11.7$) [105] is an attractive choice. A polished silicon surface makes a very flat sample platform for scanning probe microscopy and Cornell is well equipped to process silicon wafers. Despite these qualities, we selected a hybrid design for mechanical strength and ease of making coaxial cable connections. Our design is pictured in Fig. 2.21(a); the bulk of the substrate is a commercial high dielectric constant composite (Arlon, AR1000 0.015 in thick, $1\,\mathrm{oz/ft}^2$ copper,

$\epsilon_r = 10.0$; patterned and milled by PCB Fab Express with a soft gold finish) and only the center portion, where the cantilever approaches, is silicon. The CPW on AR1000 is connected electrically to the CPW on silicon using gold wire bonds. To hold the upper surface of the two substrate parallel and to keep the metal body of the microscope far way, the AR1000 and silicon substrates sit on top of an 1/8" thick macor plate. For initial tests, the widths of the metal strips were $\sim 300\,\mu\text{m}$ to facilitate aligning the cantilever to the CPW. Future designs, for use in a probe that can scan laterally, will shrink these dimensions.

Before constructing any devices, we modeled the CPW using the ANSYS model shown schematically in Fig. 2.19(a). As in our earlier simulations the conducting strips were modeled as perfect, zero thickness, conductors. The impedance of the CPW as design was checked and adjusted based on simulating a 2D slice of the model in Fig. 2.19(a). The frequency dependent simulation results are shown in Fig. 2.19(b). Simulations of the magnetic field above the CPW using the full 3D model indicate that the peak rotating magnetic field should be 0.5 G for an input $P = 250\,\text{mW}$. Additional simulations, carried out by Dr. Chang Shin using CST Microwave Studio, which include the finite conductivity of the metal layers, the appropriate thickness of the metal strips, both the AR1000 and silicon sections, and losses in the dielectric, predicts 0.4 G, in rough agreement with our simpler simulations. This simulation predicts $c_P = 800\,\text{mG}/\sqrt{\text{W}}$, more than enough transverse field for testing on TEMPAMINE.

The measured transmission through the CPW is shown in Fig. 2.21 for the device installed in the microscope; *ex situ* performance was similar. The transmission was independent of the location of the grounded, metal cantilever mounting block down to block-transmission line separations of $\sim 125\,\mu\text{m}$, the closest ap-
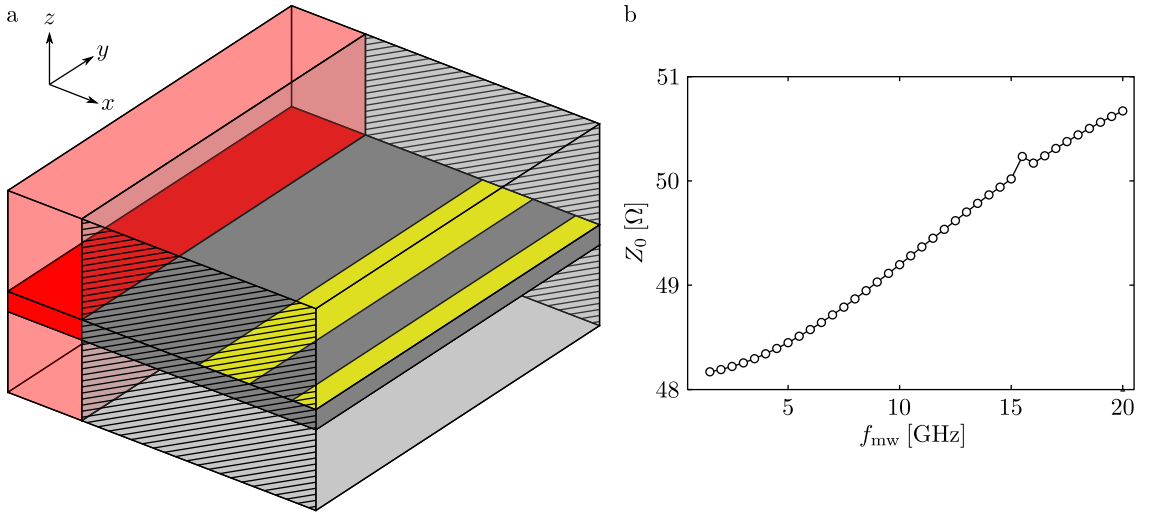
Figure 2.19: (a) Schematic of the volume used for the ANSYS simulation of the coplanar waveguide on silicon. The opaque regions are the silicon dielectric ($\epsilon_r = 11.7$) and the transparent regions are vacuum ($\epsilon_r = 1$). For this simulation, perfect zero-thickness conductors were assumed for the conductor and their locations are shown in yellow. Rather than using a much larger than necessary volume, the left side of the volume, shown in red, is a "perfectly matched layer" (PML) that absorbs any incoming electromagnetic field preventing boundary reflections from distorting the simulation results. A PML region was not used above or below since the simulation included 5 substrate thicknesses ($5 \times 0.5\,\mathrm{mm} = 2.5\,\mathrm{mm}$) above and below. The CPW is symmetric and a 1/2 size model was used, with the magnetic field constrained to be perpendicular to the volume boundary at the right edge of the model. The hatched faces were used as ports to introduce and extract the microwave field from the simulation volume. The calculated frequency-dependent impedance of this structure is shown in (b).
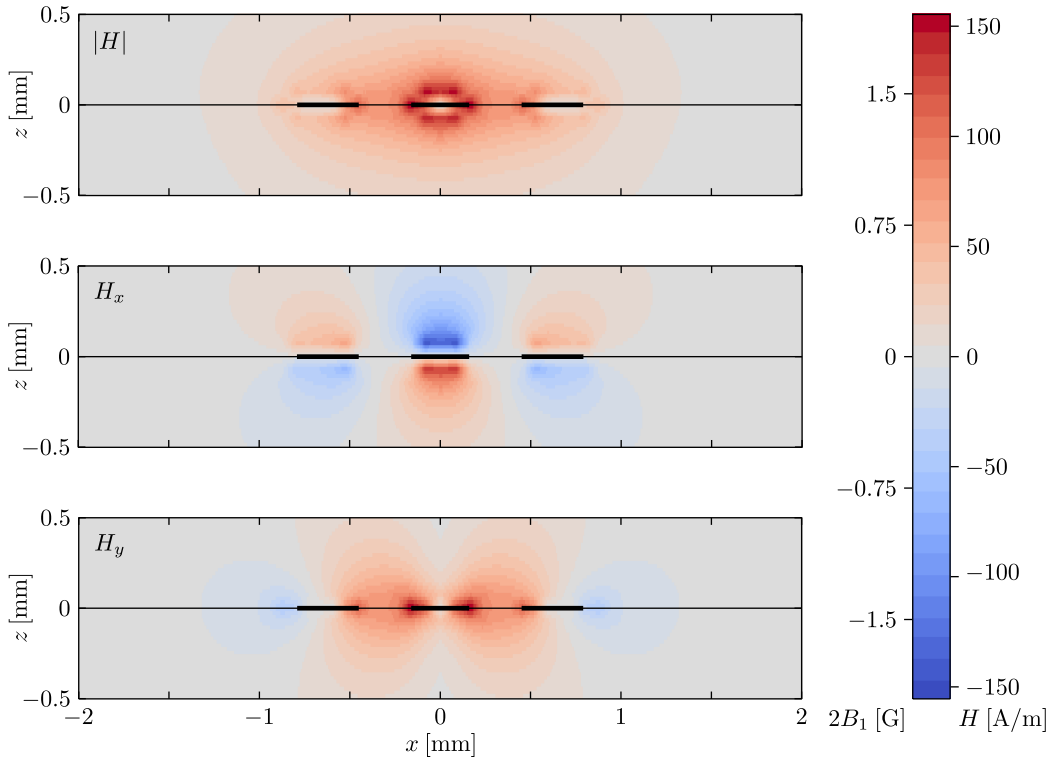
Figure 2.20: Microwave magnetic field around the coplanar waveguide on silicon calculated using ANASYS, this slice is taken 1.25 mm from port 1, see Fig. 2.19, where $P = 200\,\mathrm{mW}$ of microwave power was introduced. Although the simulation covered only the region $x \leq 0\,\mathrm{mm}$, the full device has been plotted to ease interpretation. The region depicted includes the silicon substrate, $-0.5\,\mathrm{mm} \leq z \leq 0\,\mathrm{mm}$, and the vacuum above, $0\,\mathrm{mm} \leq z \leq 0.5\,\mathrm{mm}$. The metal strips were zero-thickness perfect conductors in the simulation, however, in this figure they are indicated by thick black lines. From the central symmetry visible in $|H|$ (top), the even mode is excited. Operating in the SPAM geometry, both H_x (middle) and H_y (bottom) components of the magnetic field are oriented appropriately to manipulate the spins ($B_0 \odot$). In a future hangdown experiment, the only H_x component will be effective.

proach in an experiment. Because this is simply a length of transmission line, the output of the CPW should be directed to a 50 Ω load. There is only one coaxial cable in our microscope and adding a second one, to minimize heating of the probe head, would require an extensive microscope redesign. Therefore, we terminated the CPW using a 50 Ω load at 4 K. The DC resistance of the load we used (Mini Circuits, ANNE-50X+) actually fell from $\sim 51\Omega$ at room temperature to $\sim 50\Omega$ at 4.2 K. Additionally, a bias tee (Aeroflex, 8810SMF2-18) and DC block (Fairview Microwaves, Inc, SD3239) were used to allow biasing of the center CPW strip relative to the cantilever to minimize the surface noise.

The CPW did not perform as well as simulated. The measured coil constant was only $c_p = 38.2\mathrm{mG}/\sqrt{\mathrm{W}}$ at $f_{\mathrm{mw}} = 18\mathrm{GHz}$, 21 times smaller than expected. One possible failure mode, not captured by either simulation is the high frequency performance of the wire bonds. The wire bonds were made using the MEI 1204 manual bonder at the Cornell Center for Materials research using $0.0005 \in \times 0.002$ in gold ribbon. It was very important that the loop of wire between either end of the bond was kept as short as possible. To ensure that good electrical contact was maintained between the strip on AR1000 and the strip on silicon as many bonds as possible were made. For a CPW of the design used here, two bonds per AR1000/silicon contact were made. It was also very important that the silicon chip fit snugly into the AR1000 substrate. When the silicon chip was not a press fit, the measured transmission through the assembly was very poor. Although transmission line designs very similar to ours have been successfully used before, the operating frequency was < 9 GHz [106]. A future redesign should consider replacing the wire bonds with a direct mechanical contact (by flipping over one component) instead.
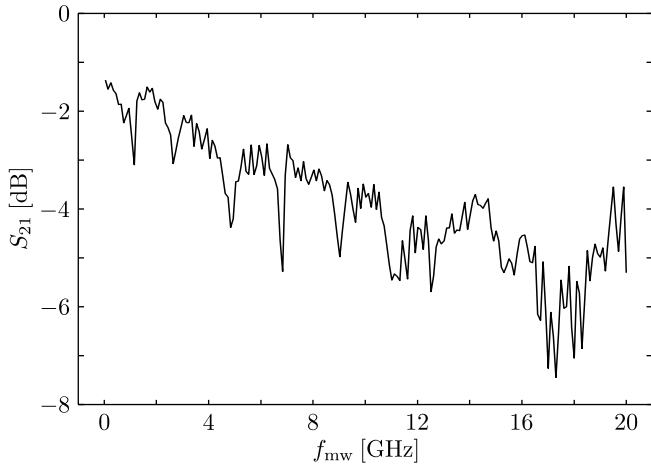
Figure 2.21: Measured transmission through the CPW while installed in the microscope. The grounded metal cantilever mounting block was $\sim 50\,\mu\text{m}$ away from the surface of the CPW during this measurement. The measured S_{21} has been corrected to show only the loss from the CPW itself. This measurement is only minimally effected by being located in the microscope.

2.4.3 Implications for Single-Electron Detection

Even with a carefully-chosen sample and meticulously designed cantilever [107], magnetic tip [39, 57, 91], microwave source [108], and protocols to detect spin fluctuations [69], 12 hr of signal averaging per point was required to observe single electron spins via i-OSCAR detection in the experiment of Ref. 28. To image individual nitroxide spin labels in a reasonable time, detection of individual electrons must be accomplished in a few seconds or minutes. Our findings suggest two modifications that will enable rapid detection of individual electron spins:

Boltzmann polarization and signal averaging. The Curie-law spin polarization is $p = 0.037$ here. Decreasing temperature to 300 mK and increasing operating frequency to 50 GHz gives $p = 0.999$. Having such a fully polarized spin as the initial condition dramatically improves the efficacy of signal averaging. This is because the improvement in the power signal-to-noise

ratio with the number of averages N scales as $\propto N$ for Curie-law signal, in comparison to the $\propto N^{1/2}$ scaling for a stochastic spin-fluctuation signal [28].

Spin modulation. The protocol of Fig. 2.8 is suitable for a single-spin experiment. With the microwaves on, spin nutation randomizes the magnetic moment of a single spin to zero over the time of a cantilever cycle. The randomly-oriented spin takes a time T_1, on average, to realign with the field via spin-lattice relaxation. The interaction of the single spin with the cantilever will thus, on average, reproduce the ensemble-average behavior depicted in Fig. 2.8. The modulation frequency in Fig. 2.8 need only satisfy $f_{\mathrm{mod}} \ll 1/T_1$, and one is at liberty to set f_{mod} to avoid surface noise (at low f) and detector noise (at high f).

Modifying the magnet-on-cantilever apparatus of Ref. 28 by replacing the irradiated quartz sample with a thin-film nitroxide-labeled biopolymer sample, working at higher field and lower temperature, and using the Fig. 2.8 protocol to detect Curie-law polarization instead of using the i-OSCAR protocol to detect stochastic polarization, we estimate that achieving a power signal-to-noise of 4 would require only 3.5 min of signal averaging. This is already sufficient to collect a 1.2×10^3 pixel image in three days. If we are willing to place the nitroxide-labeled biopolymer sample on the cantilever, we can outfit the apparatus of Ref. 35 with a microwave microwire. While the frequency noise in the Ref. 35 is unknown, if we assume that is is limited by cantilever thermomechanical fluctuations, the minimum detectable magnetic moment (in a 1 Hz bandwidth) is $0.27\,\mu_{\mathrm{B}}$, which would enable the acquisition of a 64^3-pixel image in three days.

Our approach to mechanically detecting electron spin resonance has substantially fewer technical constraints than the approach of Ref. 28. These relaxed

requirements give us significant leeway to improve per-spin sensitivity.

Microwave source. We used a microwave field of rotating-frame amplitude $B_1 = 3.9 \, \text{mG}$ to saturate spins and create a distinguishable signal while a $B_1 = 3 \, \text{G}$ field and adiabatic inversion was used in Ref. 28. Although saturation gives a signal half as large as adiabatic inversion, it requires, with a better optimized resonator than used here, only 10^{-3} times the microwave field and 10^{-6} times the microwave power — a significant advantage since microwave heating of the cantilever is a concern at low temperature [28, 108]. The smaller required B_1 gives us the freedom to employ a non-superconducting resonator and metal coat the sample to reduce surface noise.

Cantilever design. Thermal motions of the cantilever tip create a fluctuating magnetic field that, if the motions have spectral density near the Rabi frequency, can be a potent source of $T_{1\rho}$ relaxation [107]. To obtain long signal coherence times in i-OSCAR experiments, it was necessary to fabricate complex hinged cantilevers with suppressed higher, megahertz-frequency modes [28]. In contrast, the signal coherence time in our experiment is set by T_1 and therefore sensitive only to cantilever motions at the Larmor frequency of 17 GHz, which are negligible for an audio-frequency cantilever. Thus a simple beam cantilever should be sufficient for detecting individual nitroxides by the method introduced here — another significant simplification.

Tip material. Thermomagnetic noise in the tip can degrade both T_2 and $T_{1\rho}$ [39, 91] and, in magnet-on-cantilever experiments, can lead to a degradation of cantilever Q at high magnetic field [39, 57]. Here, the Q degradation was completely mitigated by orienting the field along the width of the cantilever [29, 42] (at the expense of a reduction in G', compared to an experiment in

which the tip magnetization points towards the sample plane [28]). Thermomagnetic tip fluctuations can be suppressed by using a high coercivity magnetic material for the tip, such as SmCo, and operating at low field [39] or by using a low coercivity material, such as Ni, and operating at high field [57]. The single-electron-spin experiment of Ref. 28 used a SmCo tip which had to be affixed by hand to the cantilever and whose diameter was limited to approximately 151 nm by ion-beam-milling damage. Our detection approach operates well at high field, opening up the exciting possibility of using a nickel tip which is significantly easier to deposit and lithographically pattern to sub-100 nm dimensions [33, 109].

2.5   Conclusion

The approach presented here dramatically expands the range of samples suitable for characterization by mechanically detected magnetic resonance using ultrasensitive cantilevers and opens up a new route to achieving single-electron sensitivity in reasonable averaging times. As with cryoelectron microscopy, extending our studies from a model system to a biomacromolecule will demand a significant investment in developing sample preparation protocols. Detailed studies of the mechanisms of cantilever frequency surface noise over such samples will be required to establish the ultimate limits of the approach to single-spin detection outlined above. Nevertheless, our findings clearly establish individual spin-labeled biomacromolecules as exciting possible targets for a single electron-spin experiment and suggest that research into preparing biological samples for cryogenic magnetic resonance force microscopy should be aggressively pursued.

CHAPTER 3

FRICTION, JITTER AND MECHANICALLY DETECTED ESR USING A OVERHANGING, BATCH-FABRICATED NANOROD-TIPPED CANTILEVER

3.1 Introduction

The force-gradient experiment described in Chapter 2 produced a peak signal of 0.025 mHz per fully polarized electron spin. Increasing the signal on a per spin basis requires that the spins couple more strongly to the magnetic tip and that coupling strength is ultimately determined by the magnitude of the tip field gradient, $G = dB_z/dx$. There are two ways that G can be improved over the experiment of Chapter 2: by making the magnetic tip from a magnetic material with higher magnetization than the $\mu_0 M = 0.6$ T of nickel and/or by engineering the shape of the tip to produce a stronger tip field gradient. This chapter describes experiments characterizing, using force-gradient detected ESR, close-approach surface dissipation and jitter measurements, an ultrasensitive cantilever with an integrated, overhanging nickel nanorod tip. Development of the batch fabrication procedure used to produce the cantilever and tip are described in Ref. 33 with additional details in Ref. 62. Further characterization of this magnetic tip, among others, using cantilever torque magnetometry will be described in Chapter 5.

In in all high sensitivity MRFM experiments to date, the noise floor has been set by surface induced dissipation or jitter rather than the cantilever properties and the temperature. Although it is necessary to increase the signal per spin by increasing the tip field gradient, understanding and minimizing the surface noise is also vital to increasing sensitivity. Earlier studies of close approach surface force
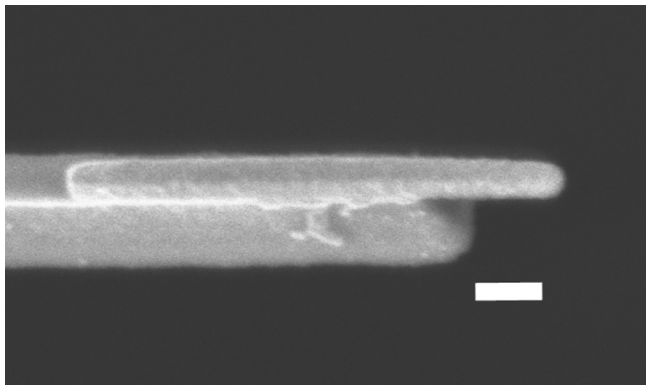
Figure 3.1: SEM image of cantilever's leading edge, showing the nickel nanorod overhanging the cantilever's leading edge by 350 nm (scale bar = 200 nm). Below the nanorod the $1.0\,\mu m \times 0.34\,\mu m$ narrowed tip of the silicon cantilever can be seen. This SEM image is was taken by S. A. Hickman.

noise [43] demonstrated a sharp, metal tip experiences less surface force noise than a blunt, silicon tip. Other workers have shown that even at low incident optical power ($P \sim 250nW$) the interferometer laser can excite electrons trapped at dopant or defect levels creating a small amount of fluctuating mobile charge in the silicon body of the cantilever [74]. This fluctuating charge can interact with electric fields from the surface to cause dissipation. Based on these results, a cantilever designed to be insensitive to surface force noise will have a sharp, metal tip, and will keep the silicon cantilever body 100s of nanometers from the sample surface. The cantilever used here was designed to meet these requirements and has a nickel tip 111 nm wide, 100 nm thick, and 1475 nm long, which overhangs the single-crystal silicon cantilever body by 350 nm. A scanning electron microscopy (SEM) image of the leading edge of the cantilever is shown in Fig. 3.1[1].

Dissipation, jitter and ESR measurements described in this chapter were conducted using the microscope, support systems, and gold coated sample described in Chapter 2.

---

[1]Figures 3.1, 3.2, 3.3, 3.4, and 3.6 reprinted with permission from Hickman *et al. ACS Nano* 4, 7141 (2010). Copyright 2010, American Chemical Society.

3.2 Dissipation Measurements

The total dissipation, Γ, experienced by the cantilever was measured as function of tip-sample separation, h. At each height, the feedback set point was adjusted to maintain a cantilever amplitude of $x_{0p} = 131\,\text{nm}$ using a software PI controller and the cantilever's frequency, f_0 and quality factor, Q, were measured as described in Chapter 2. The dissipation was calculated using the measured spring constant, k_0, frequency and quality factor using $\Gamma = k_0/2\pi f_0 Q$. The surface was located by gently touching the tip of the cantilever to the surface. At tip-sample separations of $h < 2\,\text{nm}$ the cantilever was in intermittent contact with the surface and the dissipation could not be reliably determined.

Fig. 3.2(a) is a plot of total dissipation, Γ, experienced by the cantilever as a function of tip-sample separation, h. For comparison, the dotted line is the dissipation due to internal friction in the cantilever alone. We can see that the surface-induced cantilever dissipation is negligible at tip-sample separations above $h = 10\,\text{nm}$. Internal sources of friction include clamping loses, motion of lattice defects, thermoelastic dissipation, phonon-phonon scattering, etc. [110]. For thin cantilevers, such as those used in this thesis, surface loss mechanisms have been shown to be the dominate source of internal friction [111].

Instead of reporting Γ, often it is more convenient to consider instead the magnitude of the smallest detectable force. The minimum detectable force, F_{min}, is related to the dissipation experienced by the cantilever through the fluctuation-dissipation relation for the harmonic oscillator:

$$\Gamma = \frac{1}{4k_B T} P_F(f_0) \tag{3.1}$$

where k_B is Boltzmann's constant, T is temperature, and $P_F(f_0)$ is the one-sided
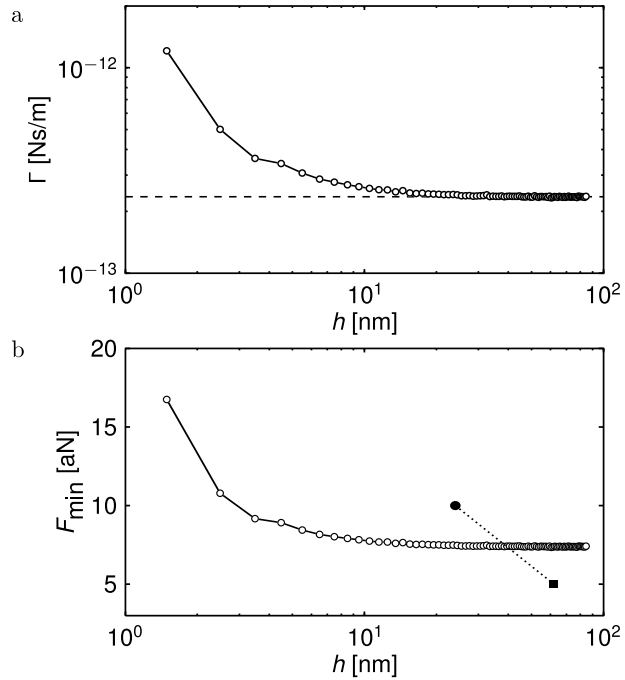
Figure 3.2: (a) Cantilever friction coefficient Γ versus tip-sample separation h. The dashed line indicates the magnitude of the dissipation that is internal to the cantilever. Surface force noise begins to deleteriously increase the friction experienced by the cantilever at $h = 20$ nm. (b) The minimum detectable force versus tip-sample separation for our tip (empty circles) and for the tip reported in Ref. 35 (filled circle and square).

spectrum of force fluctuations, evaluated at the cantilever's mechanical resonance frequency, f_0. F_{min} is then defined as

$$F_{\text{min}} = \left(\int_{f_0-b/2}^{f_0+b/2} P_F(f) df \right)^{\frac{1}{2}} = (4k_B T \Gamma b)^{\frac{1}{2}} \qquad (3.2)$$

with the bandwidth, b, conventionally taken as $b = 1$ Hz.

To compare our observed dissipation to the measured F_{min} in the most sensitive MRFM experiment to date, we convert the measured friction coefficient to the equivalent minimum detectable force using Eq. 3.2. In Fig. 3.2(b) we plot F_{min} versus tip-sample separation assuming a temperature of $T = 4.2$ K (full circles). For comparison, we plot F_{min} reported at two tip-sample separations in the recent 4 nm imaging experiment of Ref. 35 carried out at $T = 0.3$ K (filled circle and square). Our cantilever's force sensitivity is worse at large tip-sample separations, as expected since we are operating at a much higher temperature. In the experiment of Ref. 35, the minimum detectable force degraded to 10 aN at a tip-sample separation of $h = 24$ nm. Our magnetic-tipped cantilever, in contrast, maintains $F_{\text{min}} \leq 10$ aN for tip-sample separations down to $h = 3$ nm. The ability to maintain excellent force sensitivity while operating at close separation, to maximize the magnetic field gradient acting on the spin, is critical to achieving high spin sensitivity in an MRFM experiment [61].

In addition to dissipation caused by charge on the cantilever tip interacting with electric fields from the surface, eddy currents in the gold sample coating created by the motion of the spatially inhomogeneous tip field provide another potential source of dissipation. However, the dissipation measurements presented here were taken without an external magnetic field applied. Depending on the microscopic configuration of the remanence magnetization, the tip field may be very small. If the tip field is small, the dissipation in an MRFM experiment may be both larger

and longer range than measured here. Unfortunately, before this measurement could be repeated in an external magnetic field, the nanorod's magnet moment, as determined by cantilever torque magnetometry, decayed to zero. Before undertaking future MRFM experiments using a nanorod tipped cantilever, the close approach dissipation should be measured with and without an external magnetic field applied.

3.3 Frequency Jitter Measurements

Although cantilevers with overhanging nanorod tips experience very little surface force noise until the tip-sample separation is < 10 nm, the surface-induced frequency noise, as expected [54, 112], dominates the internal friction frequency noise at much larger tip-sample separations. In Fig. 3.3 we plot the power spectral density of cantilever frequency fluctuations versus offset frequency observed over the gold coated sample for tip sample separations ranging from $h = 18$ nm to $h = 1$ µm. At each tip-sample separation, the tip sample voltage was adjusted to give the smallest frequency noise and twenty-five, 25 s transients of cantilever frequency were recorded, converted to power spectra and averaged to produce the spectra shown.

At all measured tip-sample separations, the frequency noise is limited by detector noise at high offset frequencies. The displacement sensor has a white position noise floor that appears as frequency noise $\propto f^2$ [38] and is the dominate source of noise at offset frequencies of, for example, $f \geq 1$ Hz at $h = 1$ µm and $f \geq 80$ Hz at $h = 18$ nm. The bandpass filter used in the software frequency demodulator has been used to suppress frequency fluctuations above $f \sim 100$ Hz in Fig. 3.3.
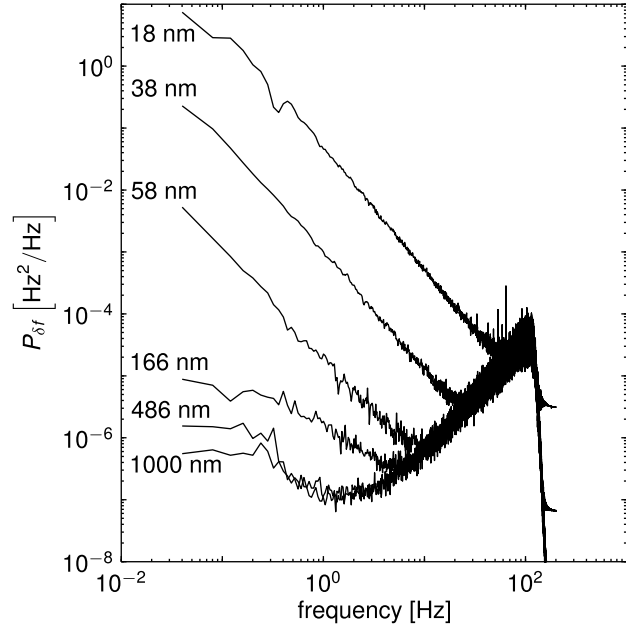
Figure 3.3: Cantilever frequency noise power spectra at various tip sample separations. At low offset frequencies $P_{\delta f}(f) \propto f^{-1}$ due to tip-surface interactions. At large tip-sample separations and low offset frequencies, $f \sim 1\mathrm{Hz}$ the cantilever frequency noise is due to the thermomechanical position fluctuations of the cantilever. As the offset frequency becomes large, $P_{\delta f}(f) \propto f^2$ due to the finite sensitivity of the optical-fiber interferometer. The optimal modulation frequency can be read directly from this plot, at tip-sample separations ≥ 486 nm, $f_{\mathrm{mod}}^{\mathrm{opt}} \approx 3$ Hz. As the tip height is decreased the optimal modulation frequency increases, to nearly $f_{\mathrm{mod}}^{\mathrm{opt}} \approx 50$ Hz at $h = 18$ nm.

67

At large tip-sample separations ($h = 486$ nm and $h = 1$ μm) and intermediate offset frequencies (f near 1 Hz), the dominate source of cantilever noise is the thermomechanical motion of the cantilever. The thermomechanical frequency noise is [64]

$$P_{\delta f}^{\text{therm}} = \frac{k_B T f_0}{2\pi^2 k_0 Q x_{\text{rms}}^2} \tag{3.3}$$

and we calculate $P_{\delta f}^{\text{therm}} = 1.4 \times 10^{-7}$ Hz^2/Hz from measured cantilever properties, temperature $T = 4.2$ K, and cantilever RMS amplitude $x_{\text{rms}} = 100$ nm. This calculated thermomechanical frequency noise is in good agreement with the observed noise near $f \sim 1$ Hz in the $h = 486$ nm and $h = 1$ μm traces of Fig. 3.3.

As the cantilever is moved closer to the sample, surface induced cantilever frequency noise become apparent at low offset frequencies. This frequency noise is presumably due to interactions of residual charge on the tip with electric field gradient fluctuations from the sample.[112] At $h = 18$ nm, the power spectral density of cantilever frequency noise at low f is $\geq 10^7$ larger than the thermomechanical limit.

When using the cantilever near the surface in an electron spin resonance experiment, there is an optimal modulation frequency. This is because the surface-induced frequency noise decreases $\propto f^{-1}$ while the detector noise increases $\propto f^2$. To measure the optimal modulation frequency, five 5 s transients of cantilever frequency were recorded and analyzed as above, at a number of tip-sample separations. At each tip-sample separation, the optimal modulation frequency $f_{\text{mod}}^{\text{opt}}$ was determined by finding the minimum value of the power spectral density of cantilever frequency fluctuations. An eleven point moving average was used to smooth the observed cantilever frequency noise power spectrum in order to facilitate identifying the minimum in the spectrum.
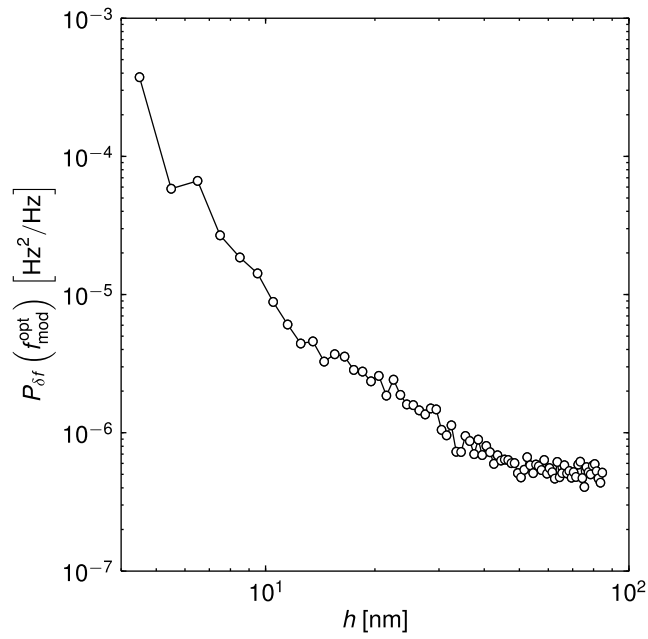
Figure 3.4: Frequency noise at the optimal modulation frequency as a function of tip-sample separation. Due to small size of the spin signal the frequency noise floor can only be so large and the modulation frequency can only be so high before the assumption that the modulation is a clean square wave begins to breakdown. These requirements and the measured cantilever frequency noise set the operating window of tip heights to $h \geq 10$ nm.

The optimal modulation frequency ranged from 25 to 5 Hz for tip-sample separations ranging from 18 to 80 nm. A plot of the power spectral density of cantilever frequency fluctuations at $f = f_{\mathrm{mod}}^{\mathrm{opt}}$ is shown in Fig. 3.4. We can see that surface interactions are the dominate source of cantilever frequency noise at tip-sample separations below approximately $h = 70\,\mathrm{nm}$.

3.4 Force-Gradient ESR Measurements

The number of techniques that can probe the magnetization of the nanorod is quite limited because of its location on the tip of a fragile cantilever and its small size. If one is restricted to techniques that do not require destructively immobilizing the cantilever by sticking it to a substrate, that number is smaller still. Furthermore, the MRFM experiment is particularly sensitive to, not the total magnetic moment of the tip, but the magnetization of the leading edge of the nanorod. All together this means that the best way to characterize a magnetic tip for use in MRFM is to simply use it in an MRFM experiment. To permit useful conclusions to be drawn in the event that no spin signal is observed, it is important to use a sample and experiment design that have already been well characterized. Here, the MRFM technique (Fig. 2.8), the sample and microwave resonator presented in Chapter 2 will be used to characterize the nanorod tip.

The cantilever was brought to 60 nm above the sample surface (80 nm above the spin containing film) in the geometry of Fig. 2.1. To saturate sample spins, a cantilever-synchronized train of 17.6 GHz microwave pulses was applied to the sample, modulated at 9.56 Hz. Unlike the experiment of Chapter 2, each pulse lasted for six cantilever cycles, followed by six cycles without microwave irradiation.
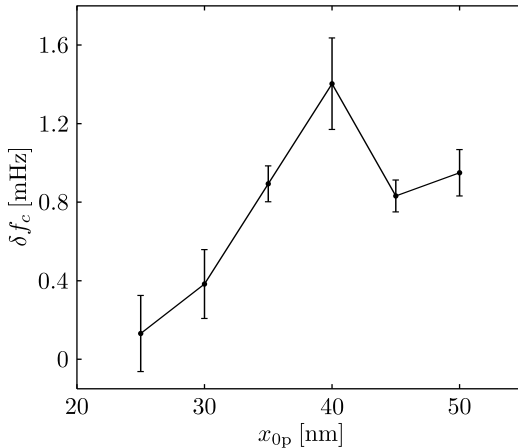
Figure 3.5: Spin-induced frequency shift as a function of cantilever amplitude. This data was collected at $\mu_0 H = 0.6225$ T; all of the experimental parameters were as described in the body of the document.

The pulse pattern was modified following an unsuccessful attempt using the half-period pulses of Chapter 2. As before, the resulting spin-induced modulation of the cantilever frequency was extracted from a digitized trace of cantilever displacement, sent to a software frequency demodulator followed by a software lock-in amplifier. After initially locating the signal, the signal size was measured as a function of cantilever amplitude, Fig. 3.5, and $x_{0p} = 80$nm selected as the cantilever amplitude for further experiments.

The measured spin-induced cantilever frequency shift is shown in Fig. 3.6(a) as a function of applied magnetic field. At each field point five 60 s traces were averaged. Between each point the magnetic field was increased by 0.5 mT, and the spectrum in Fig. 3.6(a) took 12 h to acquire. The spin signal is very small; the peak $\delta f_c = 2$ mHz is a relative frequency shift of 0.2 ppm.

In Fig. 3.6(b) we compare the observed signal to signal calculated numerically by modeling the tip as a uniformly magnetized rectangular prism. When calculating the spin polarization, the sample temperature was take to be $T = 11$K based on

71
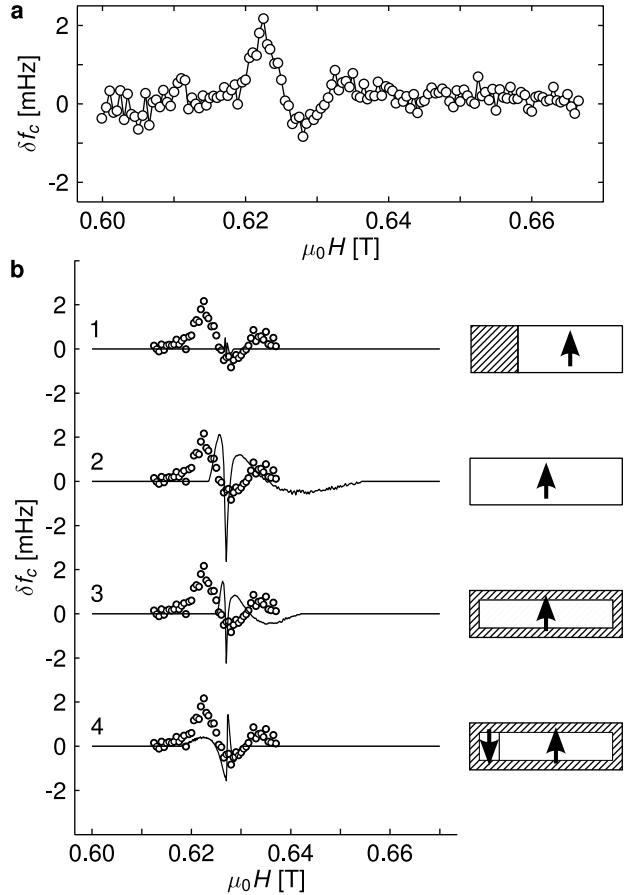
Figure 3.6: Force-gradient electron-spin resonance signal acquired using a batch-fabricated magnetic-tipped cantilever. (a) Observed cantilever frequency modulation arising from spin-tip interactions. (b) Comparison of the observed frequency modulation (open circles) and numerically calculated signal for various models of tip magnetization (solid lines, models 1–4 going from top to bottom). Here white region represent fully magnetized nickel and cross-hatched regions represent damaged nickel.

prior work with larger tips affixed to the cantilever by hand. Assuming that entire overhanging region was damaged and nonmagnetic gives a calculated signal that was far smaller than the observed signal (model 1). Assuming a fully-magnetized tip (model 2), on the other hand, overestimates the signal size and the width of the local signal, corroborating the existence of a damage layer. For reference, we note that the large negatively-going central peak in these simulations arises from a "bulk" resonance of far-way spins which experience little tip field. In model 3 we assume a uniform 12 nm thick magnetic dead layer. This model better reproduces the width of the local signal, but misses the signal present downfield from the bulk signal. The downfield signal must be due to sample spins experiencing a tip field which is parallel to the applied static magnetic field. To account for the presence of downfield signal, in model 4 we introduce a 50 nm wide domain at the leading edge of the tip magnetized antiparallel to the applied field; the agreement between simulated and observed line shape is still poor. While comparing the width and magnitude of the observed and simulated seen in Fig. 3.6 allows us to conclude that the tip's leading edge is magnetized with a damage layer no thicker than approximately 20 nm, none of the tip-damage scenarios fit the data very well.

The comparatively poor agreement between simulation and experiment apparent in Fig. 3.6 is surprising, given the quantitative agreement demonstrated in an identical experiment carried out with a ~ 4 μm diameter spherical nickel tip (Chapter 2). Our simulations approximate the tip as an ideal rectangular prism having uniform magnetization and assume that the cantilever's amplitude is zero; Additional simulations, described below, with more realistic tip shape and accounting for the finite cantilever amplitude do not substantially improve the agreement between simulation and experiment.
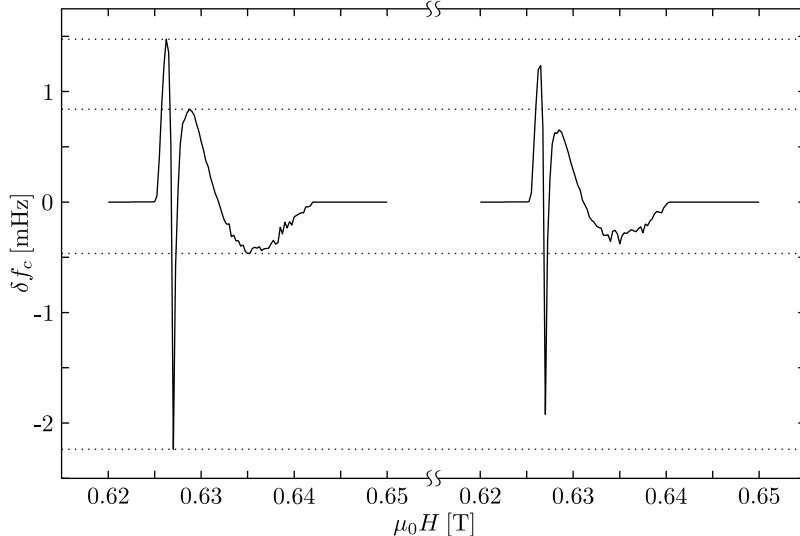
Figure 3.7: Comparison between a rounded-edge magnet model (left) and the simulation from model 3 of Fig. 3.6 (right). The more accurate model of the magnetic tip does not meaningfully improve the agreement between simulation and experiment.

3.5 Simulation Details

A rectangular prism is a convenient model for the magnetic tip because the magnetic field and derivatives can be evaluated exactly. However, it is clear from the SEM image of the magnetic tip, Fig. 3.1, that the edges of the nanorod are not sharp, but are substantially rounded over. To account for this, the magnetic tip was also modeled as a rectangular prism with rounded edges. For this round edge model, the magnetic field and derivatives were calculated by numerically integrating the "magnetic charge" or pole density over the surface of the magnet. Fig. 3.7(left), shows the signal calculated assuming magnet model 3 from above with all of the magnet's edges rounded over with a radius of $r_{\mathrm{edge}} = 20\,\mathrm{nm}$. The right hand plot of Fig. 3.7 reproduces the model 3 simulation from Fig. 3.6 for comparison. This more accurate magnet model leads to a smaller signal overall but does not change the overall shape of the simulated signal. Because the rounded-

edge model is much slower to simulate and does not meaningfully improve the agreement with experiment, the original rectangular prism model was used for all following simulations.

In Chapter 2 and in the simulations in Fig. 3.6 the spin induced spring constant shift was calculated as

$$k_{\mathrm{mag}} = \sum_j \mu_z^{\mathrm{res}} G' \tag{3.4}$$

where the sum is over all of the spins in resonance and $G' = \partial^2 B_z / \partial x^2$. Implicit in this equation is that the cantilever amplitude, $x_{0\mathrm{p}}$, is small. To determine what constitutes a small value of $x_{0\mathrm{p}}$ there are two other lengths that must be considered: the radius of the magnetic tip, r_{tip} and the tip-sample separation, h. The experiment described in Chapter 2 took place in the limit $r_{\mathrm{tip}} \gg h, x_{0\mathrm{p}}$, ($r_{\mathrm{tip}} = 2$ µm, $h = 50$–1000 nm and $x_{0\mathrm{p}} = 163$ nm) and the small amplitude assumption holds in this limit. For the force-gradient experiment described in this chapter, $r_{\mathrm{tip}} \approx 50$ nm, $h = 80$ nm, and $x_{0\mathrm{p}} = 40$ nm; it is not clear *a priori* that such an assumption will hold when $r_{\mathrm{tip}} \approx h \approx x_{0\mathrm{p}}$. To check if the small amplitude approximation is valid we can simulate the experiment taking into account the effect of the non-zero cantilever amplitude.

Eq. 3.4 comes from considering that the frequency of the cantilever is modified, in our experiment and in any other force gradient technique, by a position dependent force. Generally, this position dependent force is modeled using only the first position dependent term of its Taylor expansion:

$$F_{\mathrm{eff}} = \frac{\partial F_{\mathrm{ts}}}{\partial x} x \tag{3.5}$$

where the x is cantilever coordinate and F_{ts} is the force on the tip from the sample. In Eq. 3.4 we have identified $k_{\mathrm{mag}} \equiv \partial F_{\mathrm{ts}} / \partial x$ by recognizing that Eq. 3.5 has the same form as Hooke's law. As discussed above, this equation is valid only when

the motion of the cantilever tip, x is small enough that the force can be faithfully modeled by only the first derivative. To move beyond this approximation, we will use a result from classical Hamiltonian-Jacobi perturbation theory [113–115] that allows us to calculate the frequency shift or equivalently the spring constant shift directly. This approach to calculating frequency shifts was first applied to scanned probe microscopy by Giessibl [116], who considered tip-sample forces $\propto -x^{-n}$, with n an integer. Classical perturbation theory has also been previously applied in the context of MRFM to calculate the OSCAR frequency shift and sensitive slice[2] [117].

In Hamiltonian-Jacobi perturbation theory, the frequency shift due to a perturbing Hamiltonian V will be

$$
\begin{aligned}
\Delta f &= -\frac{f_0}{k_0 x_{0\mathrm{p}}^2} \langle F_{\mathrm{ts}}(x) x \rangle_T \\
&= -\frac{f_0}{k_0 x_{0\mathrm{p}}^2} \frac{1}{2\pi} \int_0^{2\pi} F_{\mathrm{ts}}(x_{0\mathrm{p}} \cos \phi) x_{0\mathrm{p}} \cos \phi \, d\phi
\end{aligned}
\tag{3.6}
$$

where $F_{\mathrm{ts}} = -\partial V/\partial x$ and the brackets indicate that the average is taken over one cantilever cycle. If the perturbing potential also depends on the conjugate momentum or the time Eq. 3.6 must be modified slightly [113]. For the perturbing Hamiltonians considered in this work Eq. 3.6 will be sufficient. If $V(x) = \Delta k x^2/2$, the predicted frequency shift is independent of $x_{0\mathrm{p}}$ as expected and the usual formula relating the (small) spring constant shift to the frequency shift, $\Delta f = f_0 \Delta k/2k_0$ is recovered. Before we apply Eq. 3.6 to the MRFM experiment described above, let us consider a simpler problem that can be solved exactly—calculating the frequency shift due to a single spin located directly below the tip.

Working in the hangdown geometry, consider a cantilever oriented with its long

---

[2]Berman *et al.* call it the "perturbation theory of Bogoliubov and Mitropolsky", but it is the same as the perturbation theory presented here.

axis aligned with the $\hat{z}$ axis and oscillating along $\hat{x}$, with a spherical magnetic tip of radius r_{tip} and magnetization $\boldsymbol{M} = M\hat{z}$. The cantilever interacts with a single spin of magnetic moment $\boldsymbol{\mu} = \mu_z\hat{z}$ located at $(0, 0, z)$, relative to the center of the magnetic tip. The potential that couples the spin to the tip depends on the displacement of the cantilever, x, is

$$V(x) = -\mu_z B_z = -\mu_z \frac{\mu_0 M r_{\text{tip}}^3}{3} \frac{2z^2 - x^2}{(z^2 + x^2)^{5/2}}. \tag{3.7}$$

The force on the cantilever due to the spin-tip interaction will be

$$F_{\text{ts}} = -\frac{\partial V}{\partial x} = \mu_z \mu_0 M r_{\text{tip}}^3 \frac{x^3 - 4z^2 x}{(z^2 + x^2)^{7/2}}. \tag{3.8}$$

Inserting Eq. 3.8 into Eq. 3.6 we find,

$$\Delta f = \frac{f_0 \mu_z \mu_0 M r_{\text{tip}}^3}{2\pi k_0 x_{0\text{p}}^2} \int_0^{2\pi} \frac{(x_{0\text{p}}^3 \cos^3 \phi - 4z^2 x_{0\text{p}} \cos \phi) x_{0\text{p}} \cos \phi}{(z^2 + x_{0\text{p}}^2 \cos^2 \phi)^{7/2}} d\phi. \tag{3.9}$$

In evaluating the integral, it is useful to introduce a unitless variable, $\tilde{z} \equiv z/x_{0\text{p}}$. Substituting and rearranging slightly we find

$$\Delta f = \frac{f}{2kx_{0\text{p}}} \frac{\mu_z \mu_0 M}{r_{\text{tip}}} \left(\frac{r_{\text{tip}}}{z}\right)^4 \frac{\tilde{z}^4}{\pi} \underbrace{\int_0^{2\pi} \frac{\cos^4 \phi - 4\tilde{z}^2 \cos^2 \phi}{(\tilde{z}^2 + \cos^2 \phi)^{7/2}} d\phi}_{I(\tilde{z})}. \tag{3.10}$$

The underbraced integral is an elliptic integral:

$$I(\tilde{z}) = \frac{\tilde{z}^3}{3\pi(\tilde{z}^2 + 1)^3} \left\{ 4(2\tilde{z}^4 - 7\tilde{z}^2 - 1)E\left(-\frac{1}{\tilde{z}^2}\right) - 8(\tilde{z}^4 - 1)K\left(-\frac{1}{\tilde{z}^2}\right) \right\} \tag{3.11}$$

where $K(m)$ and $E(m)$ are the complete elliptic integrals of the first and second kinds, respectively.[3]

In a measurement the signal-to-noise ratio (SNR) for detecting the spin should go to zero as the cantilever amplitude goes to zero because $P_{\delta f}^{\text{therm}} \propto x^{-2}$. We also expect that the SNR should go to zero as the cantilever amplitude becomes very

---

[3]All elliptic integrals used in this thesis are defined in terms of the parameter m rather than modulus $k(\equiv \sqrt{m})$. This is the same convention used in Mathematica and Matlab.

large because the effective spin-tip distance will be extremely large for most of the cantilever cycle. To demonstrate that these expectations are correct, we should consider the SNR rather than the frequency shift. The thermal frequency noise in a measurement bandwidth b is

$$\Delta f_{\text{noise}} = \sqrt{P_{\delta f}^{\text{therm}} b} = \sqrt{2P_F b} \frac{f_0}{2k_0 x_{0\text{p}}} \tag{3.12}$$

where $P_F = 4k_B T\Gamma$ is the one-sided spectrum of force fluctuations. Dividing Eq. 3.10 by Eq. 3.12, we calculate the SNR to be

$$\text{SNR} = \frac{1}{\sqrt{2P_F b}} \frac{\mu_z \mu_0 M}{r_{\text{tip}}} \left(\frac{r_{\text{tip}}}{z}\right)^4 I(\tilde{z}) \tag{3.13}$$

where $I(\tilde{z})$ is defined in Eq. 3.11. The SNR is composed of two parts, a ratio of constants that set the size of the signal and a unitless part, $I(\tilde{z})$, of order unity, that encapsulates the amplitude dependence.

$I(\tilde{z})$ reaches its maximum at a finite cantilever amplitude. Maximizing $I(\tilde{z})$, we find $I(\tilde{z}^{\text{max}}) = 1.07$ at $\tilde{z}^{\text{max}} = 2.1$. This is equivalent to $x_{0\text{p}} = 0.47z$. Inserting these optimal values into Eq. 3.13, the optimal SNR for detecting a single spin directly below the tip is

$$\text{SNR}^{\text{opt}} = \frac{1}{\sqrt{2P_F b}} \frac{1.07 \mu_z \mu_0 M}{r_{\text{tip}}} \left(\frac{r_{\text{tip}}}{z}\right)^4. \tag{3.14}$$

This expression and the optimal cantilever amplitude are identical to those derived, using a different approach, in Ref. 61. However, in practice the SNR calculated here is likely an overestimate, because as discussed above, it is the frequency noise due to surface proximity and the displacement sensor that set the noise level when the tip-sample separation is small. Rather than dividing Eq. 3.10 by Eq. 3.12 to produce the SNR, converting Eq. 3.10 to an equivalent force $\Delta k x_{0\text{p}}$ by multiplying by $2k_0 x_{0\text{p}}/f_0$ produces an expression that has the same amplitude dependence as Eq. 3.13 but is independent of a particular model for the noise. Fig. 3.8 is a
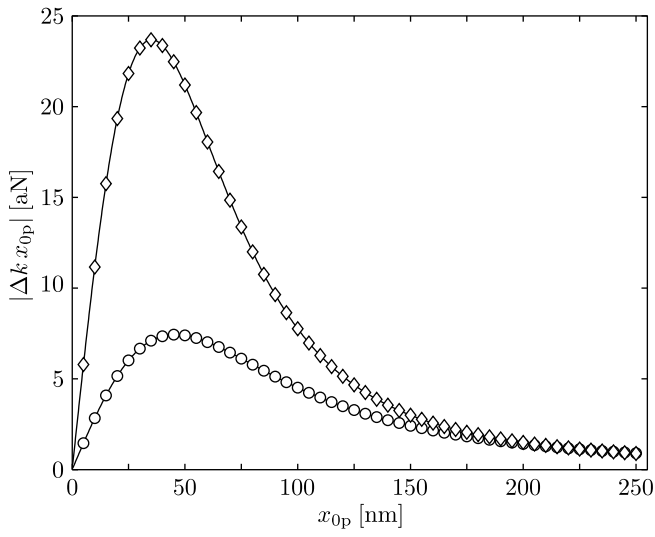
Figure 3.8: Effective force on the cantilever tip due to a single electron spin located directly below the magnetic tip in the hangdown (diamonds) and SPAM (circles) geometries. For both geometries, the solid line is the exact result and the symbols are the results of numerically integrating Eq. 3.10 or its equivalent expression for the SPAM geometry by approximating the integrand by 41 points and using the trapezoid rule. These results were calculated using $r_{\text{tip}} = 50$ nm, $z = 75$ nm, $\mu_0 M = 0.6$ T, and $\mu_z = 1\ \mu_{\text{B}}$. The Δk predicted by Eq. 3.4 appears here as the slope of the curve near $x_{0\text{p}} = 0$ nm.
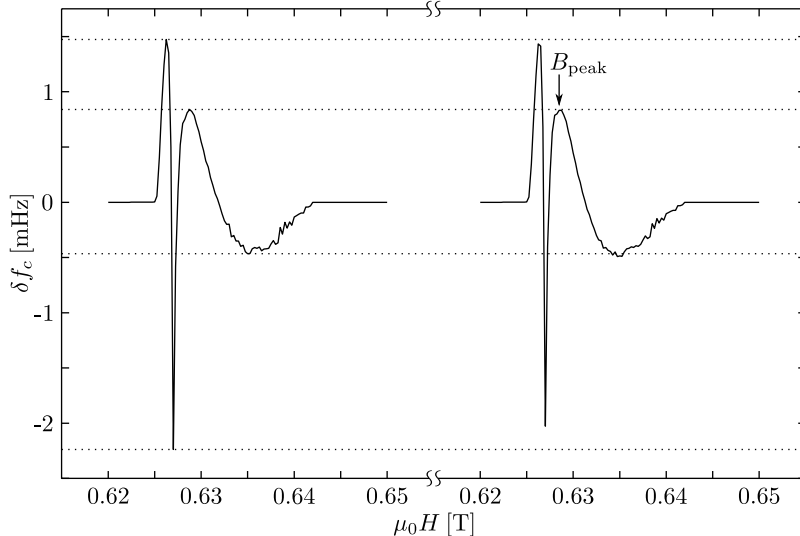
Figure 3.9: Comparison between simulated signal from model 3 (Fig. 3.6) using the small amplitude approximation (left) and classical perturbation theory (right). Comparing the peak heights using the dotted lines shows that including the effect of the cantilever amplitude on the frequency shift is small. Both simulations assume a cantilever amplitude, $x_{0p} = 40$ nm.

plot of Eq. 3.10 expressed as an effective force using $r_{tip} = 50$ nm, $z = 75$ nm, $\mu_0 M = 0.6$ T, and $\mu_z = 1\,\mu_B$. As expected, the force is zero at vanishing x_{0p}, goes to zero at large x_{0p} and reaches a peak force of $\Delta k x_{0p} = 23.7$ aN at $x_{0p} = 35.3$ nm. The equivalent result for an experiment in the SPAM geometry is also plotted in Fig. 3.8. The peak force is, however 3.2× smaller, only reaching $\Delta k x_{0p} = -7.4$ aN at $x_{0p} = 45.8$ nm.

An example of applying Eq. 3.6 to the MRFM experiment described in this chapter is shown in Fig. 3.9(right) for model 3 of Fig. 3.6; the simulated signal from Fig. 3.6 is reproduced on the left. To produce the right hand curve, the sensitive slice was defined as before, by calculating the instantaneous sensitive slice using the steady-state Bloch equations with the cantilever at maximum extension, translating the magnetization profile in the x direction to mimic cantilever oscillation, and retaining the smallest z magnetization at each point. After the sensitive

slice was computed, $F_{\text{ts}}(x)$ was calculated using

$$F_{\text{ts}}(x) = \rho M_0 \delta V \sum_j (1 - m_z(\boldsymbol{r}_j)) G(\boldsymbol{r}_j) \tag{3.15}$$

where $\rho = 2.41 \times 10^{25}\,\text{m}^{-3}$ is the spin number density, M_0 is the Curie law magnetic moment of one spin, δV is the volume of one voxel, $m_z(\boldsymbol{r}_j)$ is the reduced z magnetization, $G(\boldsymbol{r}_j) = \partial B_z(\boldsymbol{r}_j)/\partial x$ is the first derivative of the tip field, and the sum is taken over the entire sample mesh. To perform the integral in Eq. 3.6, $F_{\text{ts}}(x)$ should be evaluated for $x = x_{0\text{p}}\cos\phi$ where $0 \geq \phi \geq 2\pi$. However, evaluating Eq. 3.15 is expensive because $G(\boldsymbol{r}_j)$ must be re-evaluated for each x value and j runs to 41.4 million here. To minimize the cost, the symmetry of the cosine function and the sensitive slice can be used to calculate $F_{\text{ts}}(x)$ for an entire cantilever cycle by only evaluating Eq. 3.15 over 1/4-cycle. For these simulations, the integrand in Eq. 3.6 was approximated using 41 points, from 11 evaluations of Eq. 3.15 and the integral approximated using the trapezoid rule.

The two simulated signals in Fig. 3.9 are very nearly identical. Although the peak heights between the simulations are slightly different, the overall size and shape of the simulation has not changed and does not improve upon the poor agreement between theory and simulation in Fig. 3.6. To understand why the lineshape changes only slightly, it will be instructive to consider the effective force as a function of cantilever amplitude. Such a plot is shown in Fig. 3.10(a),[4] for an external field $B_{\text{peak}} = 0.6287\,\text{T}$, indicated by the arrow in Fig. 3.9(right). The

---

[4]There is an apparent change in the signal sign between the simulations plotted in Figs. 3.6 and 3.9 and the effective force curve shown in Fig. 3.10. In the experiment, we were not careful to set the phase of the software lock-in amplifier which results in a sign ambiguity in the measured signal. For the experiments described in Chapter 2, we resolved this ambiguity by comparison to simulation. The first round of simulations for this experiment suffered from an error in the calculation of G' for a rectangular prism. Before the error was corrected, simulation and experiment agreed with the measured signal phased as shown in Fig. 3.6. After the calculation of G' was corrected, the phase of the measured signal in Fig. 3.6 was not updated for Ref. 33 and I have kept the same phase here. However, the interpretation of Fig. 3.10(b-e) is unclear if the phase is inverted.

effective force curve is more complex than found for a single spin (Fig. 3.8), primarily because the sensitive slice is not effectively a single dimensionless point. Neglecting for a moment that the volume of the sensitive slice depends on the cantilever amplitude, the initial slope of the effective force curve is approximately the Δk calculated using the small amplitude approximation (Eq. 3.4). The $x_{0\mathrm{p}}$ indicated by the left most open circle in Fig. 3.10(a) is approximately the same as used in Fig. 3.9, and at that point the slope of the effective force curve is still very similar to its value at $x_{0\mathrm{p}} = 0$ nm. Considering the results of Fig. 3.9, the entire change in the slope of the effective force curve up to the first open circle in Fig. 3.10(a) is accounted for by the change in the slice volume from the increasing cantilever amplitude and does not represent a failure of the small amplitude approximation. Although it was not clear *a priori*, for the parameters used in the experiment described in this chapter, the small amplitude approximation holds.

At larger amplitudes the shape of effective force curve demonstrates several initially puzzling features, such as a change in sign. To understand these features, Fig. 3.10(b–e) are scale diagrams of the experiment showing the cantilever and magnetic tip above the calculated sensitive slice; the cantilever amplitude is indicated by the arrow. The points on the effective force curve, Fig. 3.10(a), that correspond to the diagrams are shown with open circles. When the cantilever amplitude is smaller than the inner radius of the sensitive slice, $r_{\mathrm{slice}}^{\mathrm{inner}}$, as in Fig. 3.10(b, c), the effective force is negative and there is a net outward force on the cantilever. At $x_{0\mathrm{p}} = 197$ nm, Fig. 3.10(c), the effective force peaks at $\Delta k x_{0\mathrm{p}} = -144.9$ aN and $x_{0\mathrm{p}} < r_{\mathrm{slice}}^{\mathrm{inner}} = 211$ nm. As the cantilever amplitude is further increased the net force decreases because of cancellation between regions of positive and negative G, until at $x_{0\mathrm{p}} = 280$ nm the effective force becomes zero and $x_{0\mathrm{p}} \approx r_{\mathrm{slice}}^{\mathrm{inner}}$. Increasing the cantilever amplitude further to $x_{0\mathrm{p}} = 296$ nm, Fig. 3.10(e), moves

in to the $x_{0p} > r_{\text{slice}}^{\text{inner}}$ regime and the sign of the effective forces becomes positive. The effective force continues to be positive and grows nearly linearly until at least $x_{0p} = 330\,\text{nm}$. Given our $\lambda = 1310\,\text{nm}$ interferometer and the scale factor, $c = 2.02$, relating the observed deflection to the deflection at the cantilever tip, $x_{0p} = c\lambda/8 = 330\,\text{nm}$ is the largest experimentally accessible cantilever amplitude.

We have shown that the poor agreement between simulation and experiment shown in Fig. 3.6 is not due to violating the small amplitude approximation used in the simulation. However, there is another assumption in the simulation that held for the experiments using a larger magnetic tip (Chapter 2) that may not hold for the smaller magnetic tip used here. All of these simulations assume that the steady-state Bloch equations are an adequate model for the spin magnetization.

One way that the assumption of steady-state might fail is if the spins do not spend long enough in resonance to saturate. The thickness of the slice in resonance at any moment is

$$\Delta x_{\text{sat}} = \frac{2\pi}{\gamma G T_2} \tag{3.16}$$

where γ is the gyromagnetic ratio, and T_2 is the spin-spin relaxation time. When the cantilever moves the spins needs to remain in the slice for a time T_{sat} to saturate. The distance that the cantilever moves before the spins saturate, $\Delta x_{\text{osc}} = v T_{\text{sat}}$, where v is the cantilever velocity, should be much smaller than the thickness of the resonant slice, $\Delta x_{\text{osc}} \ll \Delta x_{\text{sat}}$. Torrey has shown that the time required to saturate the sample spins and reach steady-state is a complex function of the resonance offset, ΔB, the magnitude of the transverse field, B_1, and the sample relaxation times, T_1 and T_2 [118]. In our experiment, ΔB depends both on time and position, meaning that T_{sat} will vary across the slice. Additionally, the time scale on which ΔB changes is the cantilever period, $T_c \approx 200\,\text{μs}$, which is only a
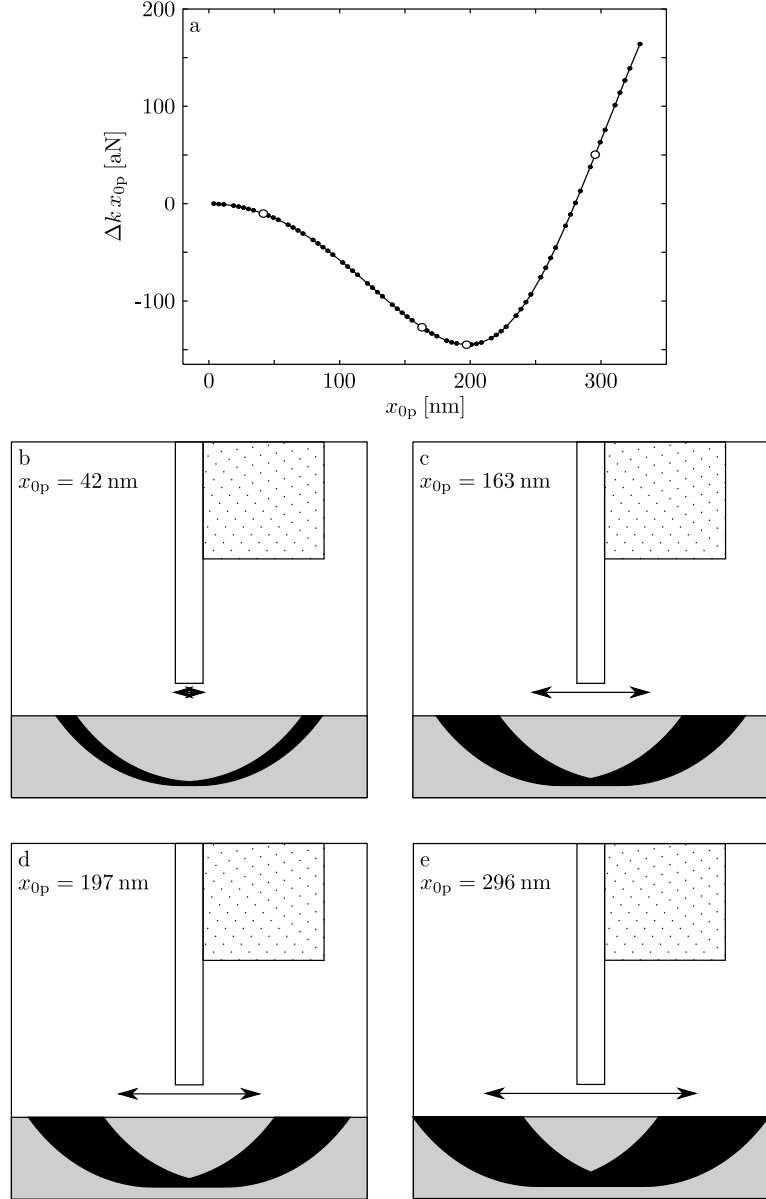
Figure 3.10: (a) Effective force as a function of cantilever amplitude for model 3. The simulation predicts that the effective force peaks at $\Delta k x_{0\mathrm{p}} = -144.9$ aN at $x_{0\mathrm{p}} = 197$ nm, passes through 0 at $x_{0\mathrm{p}} = 280$ nm and continues to grow linearly until at least $x_{0\mathrm{p}} = 330$ nm. The simulation did not consider cantilever amplitudes larger than 330 nm because they are not easily experimentally accessable, since the interferometer begins to "fold-over" at larger amplitudes. The simulation points are not equally spaced because of the finite size of the sample mesh. (b–e) Scale diagrams of the simulated sensitive slices for four cantilever amplitudes, $x_{0\mathrm{p}} = 42, 163, 197,$ and 296 nm. The overhanging nickel magnet is shown in white, the silicon body of cantilever, dotted, the sample film, light gray and the sensitive slice in black. The arrow indicates the cantilever's position at either extrema of its motion.

factor of 5 shorter than T_1. These complications in calculating T_{sat} aside, we can estimate the importance of this effect by setting $T_{\text{sat}} = T_2$. Using $v = 2\pi f_0 x_{0\text{p}}$, with $f_0 = 7374\,\text{Hz}$, $x_{0\text{p}} = 40\,\text{nm}$, and $T_2 = 500\,\text{ns}$, we calculate $\Delta x_{\text{osc}} = 1.0\,\text{nm}$. We will estimate the tip-field gradient using $G = \frac{1}{3}\mu_0 M_{\text{sat}}/r_{\text{tip}}$, with $\mu_0 M_{\text{sat}} = 0.6\,\text{T}$ and $r_{\text{tip}} = 50\,\text{nm}$. Using our estimate for G we find $\Delta x_{\text{sat}} = 0.02\,\text{nm}$. Clearly, $\Delta x_{\text{osc}} \lll \Delta x_{\text{sat}}$ and we predict that the steady-state Bloch equations are not a good model for the spin magnetization in our experiment. Applying this inequality to the experiment of Chapter 2, where we found excellent agreement between simulation and experiment, we calculate $\Delta x_{\text{osc}} = 1.0$ nm and $\Delta x_{\text{sat}} = 0.8$ nm, which, given the uncertainty in T_{sat}, satistifies the inequality.

Extending the simulation beyond the steady-state Bloch equations is difficult. The simple approach of directly integrating the Bloch equations in the rotating frame is computationally prohibitive for two reasons. Moving to the rotating frame does not remove most or all of the time dependence from our experiment as it does for traditional NMR because the large tip-field gradient means that ΔB is large, spatially variable and time dependent. Secondly, the number of numerical integrals required is too large. Rather than naively integrating, an analytical or semi-analytical approximation is required. However, for the same reasons that make directly integrating difficult, developing such an approximation is also difficult. Using a simple model, described in Appendix A, we could estimate that $B_1 > 2.2$ G will be required to saturate in an experiment using a the small magnetic tip.

3.6 Conclusions

The work presented in this chapter conclusively demonstrates that careful engineering of the cantilever's leading edge can dramatically reduce the close approach surface dissipation that it experiences when located a few nanometers above a surface. Additionally, the close approach surface dissipation measured here is, to date, the smallest ever experienced in a scanned probe experiment. Maintaining force sensitivity while operating close to the surface is a necessary component for future high sensitivity MRFM experiments. Using a small $r_{\text{tip}} \approx 50$ nm magnetic tip, as will be required for rapid, routine detection of single electron spins, will require operating with tip-sample separations of $h < 50$ nm—where without a carefully designed cantilever tip the force sensitivity would be compromised by surface noise.

Although careful engineering of the cantilever's leading edge was able to dramatically reduce the force noise, the frequency noise did not show similar improvement. The extremely large surface frequency noise experienced made the force-gradient MRFM experiment described here difficult. We were obligated to operate at a larger tip-sample separation than was ideal given r_{tip} and still required five minutes of signal averaging per point. Because the surface frequency noise probes the low frequency noise above the sample surface [64], there is little reason to think that increasing f_0 will reduce its effects. Indeed, experiments using silicon nanowires with resonant frequencies between 200 kHz and 1 MHz, that experience ultralow dissipation of $\Gamma \approx 10^{-15}$ Ns/m still experience large surface frequency noise [119].

The MRFM experiment presented here is the first ultrasensitive MRFM experiment to use a batch-fabricated magnetic tip. All earlier "scanned-probe" (i.e. magnet-on-cantilever) MRFM experiments have used micrometer-scale litho-

graphically defined magnets [120] or magnetic tips that were affixed manually [36, 39, 42, 53, 54] and whose diameters were limited to $\sim 150\,\text{nm}$ by ion damage from focussed-ion beam milling [39, 54, 55]. Although the highest sensitivity MRFM experiment [35] placed the sample on the cantilever instead of the magnet, the $0.3\,\mu\text{m} \times 1.0\,\mu\text{m}$ leading edge of the cantilever is a poor sample platform. Requiring that the sample be prepared on the end of the fragile cantilever would appear to preclude the study of a wide range of samples, such as functioning organic electronic devices or cyropreserved biomolecules and does not easily permit *in situ* study of the sample by any other technique (e.g. FRET or SEM).

Unlike the experiment presented in Chapter 2, we were unable to quantitatively simulate the MRFM signal measured here. Using classical perturbation theory we demonstrated that the poor agreement between simulation and experiment was not due to breakdown of the small amplitude approximation. However, the steady-state Bloch equations appear to be a poor model for the spin magnetization in this experiment; a computationally feasible model for the spin magnetization was not identified. The measured frequency shift first appears at a much lower magnetic field than can be explained using a uniformly magnetized rectangular prism made of nickel. If the magnetic tip is not uniformly magnetized, changing to the hang down geometry may be beneficial. In the hang down geometry the external field is aligned with the easy magnetic axis of the magnetic tip where the coercive field, B_a, is only $B_a \approx 2\text{–}20\,\text{mT}$ rather than the $B_a \approx 0.3\,\text{T}$ in the SPAM geometry used here. Simulation of the MRFM signal and cantilever magnetometry indicate there is a 10–20 nm thick magnetically dead layer on the magnetic tip. Analysis of a identically prepared magnetic nanorod using scanning transmission electron microscopy (STEM) and electron energy loss spectroscopy (EELS) [33, 63] confirm the thickness and indicate that the dead layer is most likely nickel oxide, NiO, an

antiferromagnet. The antiferromagnetic layer is another potential explanation for the non-uniform magnetization state of the magnetic tip.

CHAPTER 4

EVADING SURFACE AND DETECTOR NOISE IN
MEASUREMENTS OF FORCE GRADIENTS

4.1   Introduction

Many precision measurements rely on registering a signal of interest as a change in the amplitude or frequency of an oscillator. In theory, the ultimate precision of such measurements is limited by quantum-mechanical measurement noise; in practice, the precision achievable in an oscillator measurement is often limited by thermo-mechanical position fluctuations [38, 75], detector noise [38], or environmental fluctuations [31, 87, 112]. If one is using the oscillator to detect a time-varying *force*, then the requirements for achieving thermally-limited or quantum-limited sensitivity can be relaxed by using parametric amplification [121–123] to raise both the displacement signal and the oscillator's position-fluctuation noise above the detector's noise floor. Here we propose and demonstrate using parametric amplification to evade both detector and surface frequency noise when using a cantilever to detect a *force-gradient* signal [37].

Forces acting on microcantilevers are routinely measured at the thermo-mechanical limit, where the smallest detectable force is set by the force fluctuations, $P_F = 4k_b T \, \Gamma$, giving rise to the friction Γ experienced by the oscillator. Given the finite sensitivity of displacement sensors, however, achieving thermally-limited sensitivity in a force measurement usually requires modulating the signal force at or near the cantilever frequency, f_c, where the resulting displacement is amplified by the mechanical quality factor of the cantilever. In many cases, such modulation is inconvenient or impossible for $f_c \gtrsim 1\,\mathrm{kHz}$. In magnetic resonance force microscopy
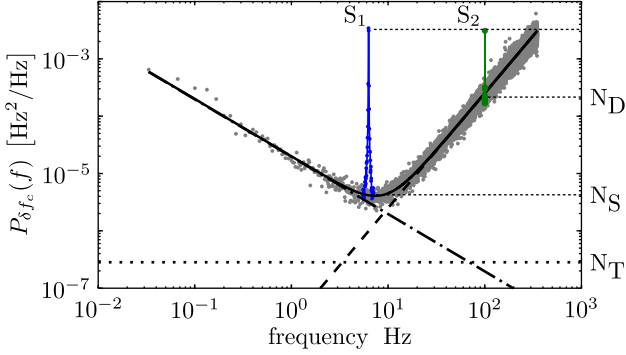
Figure 4.1: Power spectrum of cantilever frequency fluctuations with (blue and green) and without (black) a modulated force-gradient signal present. Dashed-dotted black line: surface noise. Dotted black line: thermal noise ($P_{\delta f_c}^{\mathrm{therm}} = 2.8 \times 10^{-7}$ Hz^2/Hz). Dashed line: detector noise($P_{\delta x}^{\mathrm{det}} = (10 \text{ pm})^2$/Hz). Noise at frequencies away from the signal peak in the blue and green traces has been removed for clarity.

(MRFM), for example, force modulation at f_c is often impossible because of the sample's unfavorable spin relaxation times [36, 42]. In electric force microscopy, force detection is inconvenient because of the undesirably long natural response time of the cantilever near resonance [38, 124] and the finite charging time of the sample. These shortcomings are obviated by detecting the signal as a (slowly-modulated) force gradient [36, 38, 42, 124], δk. In a force-gradient experiment, the cantilever is driven into self-oscillation via positive feedback [38] and the (modulated) force-gradient signal shifts the instantaneous frequency of the cantilever, $\delta f_c \approx f_c \, \delta k / 2k_c$, where k_c is the cantilever spring constant.

Achieving thermally-limited sensitivity in a force-gradient experiment remains challenging, however. This is illustrated in Fig. 4.1[1], in which we plot the power spectrum of cantilever frequency fluctuations seen in three representative magnetic resonance force microscope experiments (detailed below). In the first experiment (solid black line), the cantilever was brought to a height $h = 30$ nm above a

---

[1]Figures 4.1, 4.2, and 4.3 reprinted with permission from Moore *et al. Appl. Phys. Lett.* 97, 044105 (2010). Copyright 2010, American Institute of Physics.

gold-coated surface, driven to a root-mean-square amplitude of $x_{\text{rms}} = 73$ nm, and the tip-sample potential adjusted to minimize tip charge and therefore frequency noise. The observed frequency noise (solid black line) is a sum of three contributions: 1) thermo-mechanical position fluctuations (dotted line) with power spectrum $P_{\delta f_c}^{\text{therm}} = 4k_b T \Gamma \left(f_c / 2k_c x_{\text{rms}} \right)^2$, 2) detector noise (dashed line) having a power spectrum $P_{\delta f_c}^{\text{det}} = P_{\delta x}^{\text{det}} f^2 / x_{\text{rms}}^2$, where $P_{\delta x}^{\text{det}}$ is the detector noise written as an equivalent cantilever displacement fluctuation, and 3) surface noise (dot-dashed line) $P_{\delta f_c}^{\text{surf}}(f) \propto f^{-1}$ arising from uncompensated tip charge coupling to fluctuating electric field gradients produced by the sample [112].

In the second and third experiments, the magnetization of unpaired electron spins in the sample was modulated to create the force-gradient signal at 6.28 Hz (blue line) and 100 Hz (green line), respectively, in Fig. 4.1. We can see in the figure that even though the modulation frequency was chosen optimally, the noise in the 6.28 Hz experiment was nevertheless dominated by surface noise; consequently, the observed signal-to-noise ratio S_1/N_S is smaller than the thermally-limited signal-to-noise ratio S_1/N_T by a factor of 14. Modulating at 100 Hz does avoid surface noise, but the noise is dominated instead by detector noise and the observed signal-to-noise ratio is even worse: S_2/N_D is smaller than S_2/N_T by a factor of nearly 10^3.

To achieve a thermally-limited signal-to-noise ratio in this representative force-gradient experiment would require modulating at a frequency $f_{\text{mod}} \gg 80$ Hz *and* operating with a detector having a position sensitivity of $P_{\delta x}^{\text{det}} \ll (390 \text{ fm})^2/\text{Hz}$, 26 times smaller than we currently achieve using optical fiber interferometry ($P \approx 3\mu\text{W}$). More sensitive displacement sensors exist, such as single electron transistors [125, 126], atomic point contacts [127, 128] and high-finesse optical cavities [129].

Although all of these can in principle be used to monitor the cantilever deflection, all three present substantial integration challenges that currently preclude their use in general scanned probe experiments. A similar optical fiber interferometer, operating at much higher optical power ($P > 1$ mW) improves the attainable position sensitivity to $(2\,\text{fm})^2/\text{Hz}$ [130]. However, operating with more than a few microwatts of optical power is not compatible with operating at $T = 4.2\text{K}$ and lower temperatures require even smaller optical powers [131] to avoid cantilever heating. Here we introduce a parametric amplification scheme that 1) is compatible with a force-gradient measurement; 2) can be used with a modulated signal, allowing the signal to evade the effect of surface frequency noise; and 3) converts a frequency signal to an amplitude signal at f_c, evading detector frequency noise. In contrast with other applications of parametric amplification in which an externally supplied force gradient amplifies a small force signal, here the signal of interest acts as the amplifier.

4.2   Methods

As in previous work [36], a force-gradient signal was generated by interacting unpaired electron spins in a gold-coated film of TEMPAMINE with a high-compliance magnetic tipped cantilever. Experiments were carried out in vacuum ($P = 10^{-6}$mbar) and at cryogenic temperatures ($T = 8$ K). The cantilever had $f_c = 4829$ Hz, $k_c = 7.8 \times 10^{-4}\,\text{N/m}$, a mechanical quality factor $Q = 3.8 \times 10^4$, and a nickel tip of radius $r = 2\,\mu\text{m}$. A (swept) magnetic field of $B_0 = 0.50\,\text{T}$ to $0.85\,\text{T}$ was applied to polarize the sample spins and a pulsed 17.28 GHz transverse magnetic field from a half-wave microstripline resonator was applied to saturate sample spins. Spin magnetization μ_z in the sample interacted with the magnetic field from the mag-

netic tip to create a force gradient, Δk_{spin}, which shifted the resonance frequency of the cantilever [36, 42]:

$$\Delta k_{\mathrm{spin}} = \sum_j \mu_{z,j} \partial^2 B_z^{\mathrm{tip}}(\boldsymbol{r}_j)/\partial x^2 \tag{4.1}$$

where the sum is over all spins in resonance at the given applied field. A small potential, $V_{\mathrm{DC}} \approx 1$ V, was applied between the cantilever and the gold sample coating to control the charge on the cantilever tip. The cantilever was driven below resonance at a frequency $f_d = 48 f_c/49 = 4730$ Hz by applying an oscillating voltage $V_{\mathrm{AC}} = 33$ V_{rms} from a waveform generator (Agilent 33250A) to a nearby wire. The force applied to the cantilever from the drive wire is

$$F_{\mathrm{wire}}(t) = \frac{1}{2} C' \left(V_{\mathrm{DC}} + \sqrt{2}\, V_{\mathrm{AC}} \cos\left(2\pi f_d t\right)\right)^2 \tag{4.2}$$

where $C' = \partial C/\partial x$ is the derivative of the wire-cantilever capacitance with respect to the direction of cantilever motion. The resulting amplitude of motion at frequency f_d,

$$\begin{aligned} x_{\mathrm{d}} &= \frac{\chi(f_d)}{k_c} F_{\mathrm{d}} \\ &\approx C' V_{\mathrm{DC}} V_{\mathrm{AC}} \frac{\chi(f_d)}{k_c}, \end{aligned} \tag{4.3}$$

with $\chi(f_d) \approx (1 - f_d^2/f_c^2)^{-1}$ the susceptibility and F_{d} the component of F_{wire} oscillating at f_d; x_d was 99 nm for experiments here. During the experiment, the effective Q of the cantilever was reduced to $Q_{\mathrm{eff}} = 3 \times 10^3$, using negative feedback applied by a piezo at the cantilever base [132]. The sample spin magnetization, μ_z, was modulated at a frequency $f_p = f_c/49 = f_d/48 = 98.55$ Hz by pulsing the microwave field in synchrony with the cantilever motion [36].

4.3 Results

The equation of motion governing the cantilever displacement x is

$$\ddot{x} + \frac{\omega_c}{Q_{\text{eff}}}\dot{x} + \omega_c^2 x + \frac{\omega_c^2 \sqrt{2}\delta k_{\text{spin}} \cos\left(\omega_p t\right)}{k_c} x = \frac{\omega_c^2 \sqrt{2} F_{\text{d}}}{k_c} e^{i\omega_d t} \tag{4.4}$$

where we have expressed frequencies in angular units, $\omega_p = \omega_c - \omega_d$ and $\delta k_{\text{spin}} = \sqrt{2}\Delta k_{\text{spin}}/\pi$ includes only the first Fourier component of the pulse modulation. We look for a solution of the form

$$x(t) = \sum_{n=-\infty}^{\infty} a_n e^{i(n\omega_p + \omega_d)t} \tag{4.5}$$

and are particularly interested in two coefficients: $a_0/\sqrt{2} = x_{\text{d}}$ and $a_1/\sqrt{2} \equiv \delta x_{\text{spin}}$, the amplitude of the spin-induced oscillation at the cantilever's resonance frequency. Inserting Eq. 4.5 into Eq. 4.4, passing the time derivatives into the sum, and rearranging we find

$$\sum_{n=-\infty}^{\infty} e^{i(n\omega_p + \omega_d)t} \left[\frac{\omega_c^2 \sqrt{2}\delta k_{\text{spin}}}{2k_c} a_{n+1} + \left\{ -(n\omega_p + \omega_d)^2 + \frac{i(n\omega_p + \omega_d)}{Q_{\text{eff}}} + \omega_c^2 \right\} a_n \right.$$
$$\left. + \frac{\omega_c^2 \sqrt{2}\delta k_{\text{spin}}}{2k_c} a_{n-1} \right] = \frac{\omega_c^2 \sqrt{2} F_d}{k_c} e^{i\omega_d t}. \tag{4.6}$$

This sum leads to an infinite set of coupled equations for the coefficients $\{a_n\}$. The coupled equations may be written as a matrix where the matrix is tridiagonal. If we approximate the infinite matrix by just the 2×2 matrix containing the coefficients we are interested in

$$\begin{pmatrix} -\omega_d^2 + \frac{i\omega_c\omega_d}{Q_{\text{eff}}} + \omega_c^2 & \frac{\omega_c^2 \sqrt{2}\delta k_{\text{spin}}}{2k_c} \\ \frac{\omega_c^2 \sqrt{2}\delta k_{\text{spin}}}{2k_c} & \frac{i\omega_c^2}{Q_{\text{eff}}} \end{pmatrix} \begin{pmatrix} \sqrt{2}x_d \\ \sqrt{2}\delta x_{\text{spin}} \end{pmatrix} = \begin{pmatrix} \frac{\sqrt{2}F_d}{k_c} \\ 0 \end{pmatrix}, \tag{4.7}$$

inverting we find, in the limit $Q_{\text{eff}} \gg 1$,

$$\delta x_{\text{spin}} = \frac{i\sqrt{2}Q_{\text{eff}}x_{\text{d}}}{2k_c}\delta k_{\text{spin}}. \tag{4.8}$$
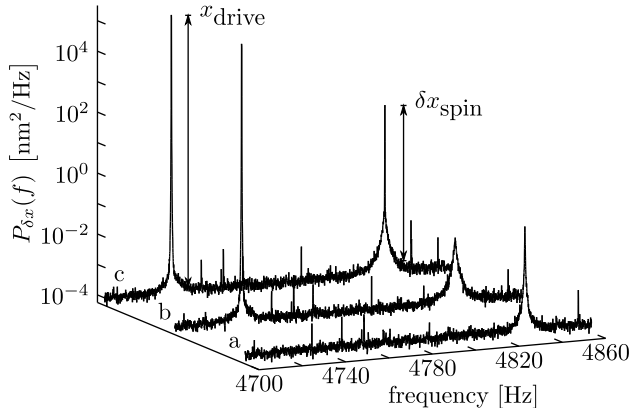
Figure 4.2: Power spectral density of cantilever motion: (a) thermo-mechanical displacement fluctuations; (b) with negative feedback active while the cantilever was driven at a frequency $f_d = f_c - f_p = 4730\,\mathrm{Hz}$; and (c) identical condition to (b), but with a microwave field pulsed at $f_p = 98.55\,\mathrm{Hz}$. Conditions: $B_0 = 0.5925\,\mathrm{T}$, $h = 200\,\mathrm{nm}$.

The central prediction of Eq. 4.4 through Eq. 4.8 is that the spin-induced spring constant modulation δk_{spin} at frequency f_p acts to up-convert some of the oscillation at frequency f_d to an oscillation at frequency f_c. The data in Fig. 4.2 verify this prediction. For reference, Fig. 4.2(a) shows the power spectrum of thermo-mechanical motion of the nascent cantilever. In Figure 4.2(b) we see the thermo-mechanical motion peak near 4829 Hz broadened by negative feedback and, in addition, a large peak near 4730 Hz due to the applied drive. In Fig. 4.2(c) the microwaves have been turned on and an additional narrow peak can be seen, near 4829 Hz, on top of the damped thermo-mechanical motion. This narrow peak demonstrates the up-conversion of a force-gradient *frequency* signal at f_p to an *amplitude* signal at f_c.

We next demonstrated that our parametric up-conversion technique was effective at evading detector noise, allowing us to modulate fast enough to also avoid surface noise. Figure 4.3(a) is a plot, versus external magnetic field, of the Fourier component at $f_p = 6.28\,\mathrm{Hz}$ of the spin-induced cantilever frequency shift. This
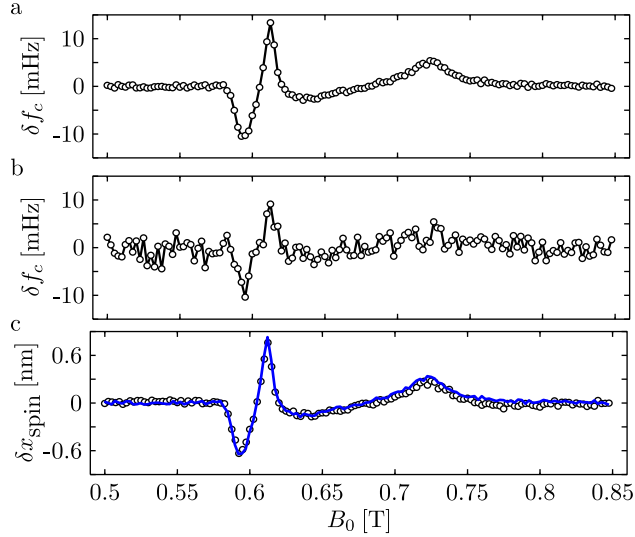
Figure 4.3: Cantilever magnetic resonance recorded via modulated force-gradient detection and parametric up-conversion amplitude detection. (a) Optimal frequency-shift measurement ($f_p = 6.28$ Hz, RMS amplitude 99 nm, and a background of -14.8 mHz subtracted). (b) Surface-noise evading frequency shift measurement ($f_p = 100.57$ Hz but otherwise identical to (a)). (c) Detection of magnetic resonance via parametric up-conversion of a frequency-shift signal (open circles, $f_p = 98.55$ Hz and a 0.53 nm background subtracted.) The blue line is the signal predicted from Eq. 4.8 and the frequency-shift signal in (a), scaled to account for the difference in modulation frequencies[37, Supplemental Materials] (scale factor = 0.70). Conditions: 2.5 mT/pt field step and detection bandwidth $b = 1$ Hz.

modulation rate was chosen to minimize the frequency noise due to the surface and the detector (Fig. 4.1). The shape of the resulting magnetic resonance signal arises from considering that spins are in resonance with the sum of the tip field and the external field and weighting each spin in resonance by the second derivative of the tip field $\partial^2 B_z^{\text{tip}}(\boldsymbol{r}_j)/\partial x^2$ at the location $\boldsymbol{r}_j$ of each spin [36]. Increasing the modulation rate to $f_p = 100.57\,\text{Hz}$, so that surface frequency noise will no longer affect the measurement, does not improve the signal-to-noise (4.3(b)). This is as expected given the large detector noise apparent at $f = 100\,\text{Hz}$ in Fig. 4.1.

Using a spin modulation rate of $f_p = 98.55\text{Hz}$ and the parametric up-conversion scheme described above, in contrast, succeeds in evading surface noise. The up-converted amplitude experiment, Fig. 4.3(c), has a signal-to-noise ratio equivalent to that seen in the optimal frequency-shift experiment, Fig. 4.3(a). The observed signal (circles) agrees quantitatively with the signal predicted (line) using Eq. 4.8, calculated using the observed frequency-shift signal in Fig. 4.3(a), x_d, and Q_eff as inputs.

4.4 Discussion

Given the power spectrum of frequency fluctuations observed in Fig. 4.1, we initially expected the up-conversion experiment to have a signal-to-noise closer to the thermo-mechanical limit ($\text{S}_2/\text{N}_\text{T}$ in Fig. 4.1). We found, however, that the signal-to-noise in the up-conversion experiment depended critically on the quality of the sine wave used to drive the cantilever off-resonance at f_d. To explain this finding, we calculated the power spectrum $P_{\delta x_n}(\omega_c)$ of cantilever amplitude noise arising from voltage fluctuations in the drive source by adding a voltage-noise term,

$\delta V_n(t)$, to Eq. 4.2. Voltage fluctuations will be a negligible source of noise when $P_{\delta x_n}(\omega_c) \ll P_{\delta x}^{\text{therm}}(\omega_c)$, the power spectral density of cantilever thermo-mechanical fluctuations. Meeting this condition requires a source with noise voltage power spectrum that satisfies

$$\frac{4k_b T \Gamma |\chi(f_d)|^2}{k_c^2 x_d^2} \gg \frac{P_{\delta V_n}(\omega_c)}{V_{\text{AC}}^2} + \frac{P_{\delta V_n}(\omega_c + \omega_d)}{2V_{\text{DC}}^2} + \frac{P_{\delta V_n}(\omega_c - \omega_d)}{2V_{\text{DC}}^2}. \tag{4.9}$$

We conclude that the drive oscillator will contribute negligibly to cantilever position fluctuations at resonance if its voltage amplitude noise is much smaller than $-97\,\text{dBc/Hz}$ at $f_c = 4829\,\text{Hz}$ and much smaller than $-125\,\text{dBc/Hz}$ at $9559\,\text{Hz}$ and $98.55\,\text{Hz}$. Although the amplitude noise for our untuned audio-frequency drive oscillator is unspecified, we note that this level of amplitude noise is challenging to achieve even with a high-Q tuned radiofrequency oscillator.

4.5 Conclusion

In conclusion, we have introduced an approach for detecting minute force gradients acting on an harmonic oscillator and have demonstrated that the approach enables the measurement to evade surface- and detector frequency noise. We have thus achieved a similar result to Budakian, *et al.* [133], but without the need to modulate spin magnetization at f_c and in an experiment which is conceptually simpler, easier to implement, and applicable to other forms of scanned probe microscopy beyond MRFM. Calculations indicate that further improvements in the electrical noise in the drive oscillator should enable the technique to better approach thermally-limited sensitivity. Although we have chosen to demonstrate this technique using magnetic resonance force microscopy, we believe the approach is generally applicable to any oscillator force-gradient measurement.

CHAPTER 5

CANTILEVER TORQUE MAGNETOMETRY OF THE IN-PLANE TO OUT-OF-PLANE TRANSITION IN INDIVIDUAL NICKEL NANORODS

5.1 Introduction

Quantifying both the average moment and magnetic fluctuations of individual nanometer-scale ferromagnets is critically important for developing stable high-density recording media [134–137], sensitive magnetoresistive heads and spin-based electronic devices [138], and pushing magnetic resonance imaging to atomic resolution via mechanical detection [35, 36, 61]. Magnetization fluctuations in individual sub-micron ferromagnets have been detected through voltage and current noise measurements [139], SQUID magnetometry [140], magnetic force microscopy [141], and, at record sensitivity, by frequency-shift torque magnetometry [29, 56, 57, 142]. The highest-sensitivity cantilever magnetometry studies to date have employed high-compliance cantilevers [51, 52] to examine in-plane switching of individual magnetic nanorods [56, 57]. Here we present a cantilever magnetometry study of *in-plane* to *out-of-plane* magnetization switching and fluctuations in a nickel nanorod at low temperature. We observe multiple sharp, simultaneous transitions in cantilever frequency, quality factor, and frequency jitter associated with individual switching events in the nanorod not seen in previous in-plane cantilever magnetometry experiments.

Table 5.1: Summary of cantilever and magnet properties. The hard axis fit for cantilever C1 and C2 extends to only 2 T. The magnet properties for cantilever C4 are a simultaneous fit to both the easy axis and hard axis data.

	quantity	C1[a]	C2	C3	C4[b]	unit
cantilever properties at $T = 4.2$ K	f_c	8778	9000	8635	4838	Hz
	k	780 ± 130	852^c	852^c	703 ± 52	$\times 10^{-6}$ N m^{-1}
	Q	86,500	135,000	135,000	94,000	(unitless)
	Γ	163	112	116	246	$\times 10^{-15}$ N s m^{-1}
magnet dimensions	l_m	1500	1500	1500	1500	nm
	w_m	200	160	200	220	nm
	t_m	50	50	50	90	nm
magnet properties from easy-axis fits	μ_{sat}	8.04 ± 1.29	4.14 ± 0.62		11.72 ± 1.27	$\times 10^{-15}$ A m^2
	$\mu_0 M_{\text{sat}}$	0.68 ± 0.11	0.43 ± 0.07		0.49 ± 0.08	T
	ΔN	0.54 ± 0.09	0.89 ± 0.13		0.40 ± 0.10	(unitless)
magnet properties from hard-axis fits	μ_{sat}	8.03 ± 1.34	5.48 ± 0.56	9.77 ± 1.47		$\times 10^{-15}$ A m^2
	$\mu_0 M_{\text{sat}}$	0.67 ± 0.11	0.57 ± 0.06	0.82 ± 0.12		T
	ΔN	0.36 ± 0.06	0.41 ± 0.04	0.29 ± 0.04		(unitless)
	$\mu_{\text{sat}}^{\text{nominal}}$	7.16	5.73	7.16	14.18	$\times 10^{-15}$ A m^2

[a]Cantilever C3 of Ref. 33
[b]Cantilever C6 of Ref. 109
[c]Calculated from cantilever dimensions and material properties.
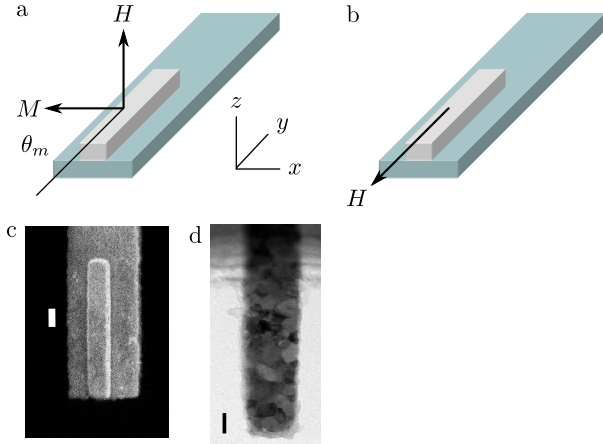
Figure 5.1: Relative orientation of cantilever, nickel nanorod tip, and applied magnetic field $\mu_0\boldsymbol{H}$ for (a) hard-axis and (b) easy-axis cantilever magnetometry experiments. The cantilever oscillates in the z direction. When modeling the tip at high field as a uniformly magnetized particle, we will treat the tip magnetization, $\boldsymbol{M}$, as oriented in the y-z plane and inclined at an angle θ_m with respect to the nanorod's easy axis. (c) Scanning electron micrograph of cantilever C1's leading edge; scale bar = 200 nm. (d) Bright-field scanning transmission electron micrograph of a nanorod fabricated to overhang the cantilever's leading edge; scale bar = 50 nm.

5.2 Methods

A schematic of the experiment is shown in Fig. 5.1(a). Nickel nanorods were fabricated near the end of an attonewton-sensitivity cantilever, as described below. The external swept magnetic field, H, points through the thickness of the cantilever and, as the field is increased, the nanorod's magnetic moment switches from in-plane to out-of-plane. As a control, we also examined in-plane switching, Fig. 5.1(b), with the magnetic field aligned with the long axis of the cantilever and nanorod.

Cantilevers ($L = 200$ μm long, 4 μm wide, and 0.34 μm thick) were fabricated from a single crystal silicon-on-insulator wafer [33, 52]. Cantilever parameters are given in Table 5.1. For cantilevers C1–C3 a single nickel nanorod was fabricated

at the end of each cantilever using e-beam patterning and liftoff; 5 nm of Cr was evaporated as an adhesion layer, followed by 50 or 90 nm of Ni, both deposited at 0.25 nm/s. The resulting nickel nanorods were 1500 nm long, 160 to 200 nm wide, and 50 or 90 nm thick. A scanning electron microscope (SEM) image of the leading edge of a representative cantilever is shown in Fig. 5.1(c). For cantilever C4 the nickel nanorod was fabricated separately on a freestanding silicon microchip using similar e-beam pattering and liftoff. The tip of the microchip supporting the nanorod was subsequently removed from the substrate via focussed-ion beam milling and attached to a bare cantilever using focussed-ion beam deposition of platinum [109]. A separate nanorod with dimensions $1500\,\mathrm{nm} \times 150\,\mathrm{nm} \times 100\,\mathrm{nm}$ was prepared for analysis by scanning transmisson electron microscopy (STEM) and electron energy-loss spectroscopy (EELS) by underetching the silicon at the cantilever's leading edge [33]. This nanorod was found to have an oxide-rich/nickel-poor coating 15 to 20 nm thick (EELS; data not shown, see Ref. 33) and was polycrystalline with grain sizes in the 20 to 40 nm range (STEM image; Fig. 5.1(d)).

Cantilever magnetometry experiments were performed at 4.2 K in high vacuum, as described in Ref. 57. Cantilever deflection was observed with a temperature-tuned 1310 nm optical fiber interferometer [71]. The cantilever deflection signal was sent to an analog gain-controlled positive feedback circuit [38] whose output excited a piezoelectric crystal located near the cantilever base. The phase and gain of the feedback loop was adjusted to drive the cantilever into self oscillation at a zero-to-peak amplitude of $z_c = 134$ nm (except where noted). A software frequency demodulator (Ref. 64, Supporting Information) was used to determine the instantaneous cantilever frequency from a record of the cantilever deflection versus time, from which the average cantilever frequency was obtained and the frequency-fluctuation power spectrum was computed. Spring constant shifts were

calculated from observed frequency shifts using $\Delta k = 2k\,\Delta f/f_c$. The gain of the positive feedback loop was controlled using a software PI loop and the instantaneous gain used to infer the cantilever quality factor, Q, from which the dissipation was calculated using $\Gamma = k/2\pi f_c Q$.

5.3   Results

The results of a representative easy-axis magnetometry control experiment is shown in Fig. 5.2 for cantilever C1. The observed coercive field of 2 to 20 mT is consistent with in-plane switching via either a curling mechanism [143, 144] or domain wall nucleation and depinning [145]. Above the coercive field the Δk was fit to[29, 56]

$$\Delta k = \frac{B_{\mathrm{sat}} V}{\mu_0 L_{\mathrm{eff}}^2} \frac{B B_a}{B + B_a} \tag{5.1}$$

using the known tip volume V, applied magnetic field $B = \mu_0 H$, effective length for the first flexural mode $L_{\mathrm{eff}} = L/1.377$, and an anisotropy field of $B_a = B_{\mathrm{sat}} \Delta N_{zy}$ with B_{sat}/μ_0 the saturation magnetization and $\Delta N_{zy} = N_z - N_y$ the difference in z and y axis demagnetization factors. The best-fit values are shown in Table 5.1. The measured values of B_{sat} and ΔN compare reasonably well with the $B_{\mathrm{sat}} = 0.60$ T and $\Delta N = 0.50$ expected for a high aspect ratio nickel rod.

In addition to measuring the cantilever spring constant shift, the magnetic field dependent dissipation and frequency jitter were also measured and are shown in Fig. 5.2 for cantilever C1. Although the cantilever dissipation, Fig. 5.2(b), does change with the magnetic field, the magnitude of the shift is similar to that experienced by a bare silicon cantilever (data not shown) as has been previously observed for slightly larger nickel tips [57]. The frequency jitter, Fig. 5.2(c), in a bandwidth $b = 15$ Hz shows no dependence on magnetic field. The magnitude

Figure 5.2: Cantilever magnetometry data taken with the field applied along the easy-axis direction of cantilever C1 (y, Fig. 5.1(b)), sweeping from -4 T to $+4$ T. (a) Plot of the fractional cantilever spring constant shift (solid line) and a fit to Eq. 5.1 used to extract the magnet properties (dashed line), with inset showing magnetization switching with a coercive field of ~ 5 mT. (b) The cantilever dissipation Γ is slightly field dependent, however for a magnet of this size, the field induced dissipation is no larger than that experienced by a cantilever without a magnetic tip. (c) The cantilever root-mean-square frequency fluctuations measured in a 15 Hz bandwidth.

of the observed frequency jitter can be entirely accounted for by considering two sources of frequency fluctuations. The first source of frequency fluctuations is the thermomechanical position fluctuations of the cantilever which give rise to a white frequency fluctuation spectral density, $P_{\delta f}^{\text{therm}}(f) = 4.8 \times 10^{-7} \text{ Hz}^2/\text{Hz}$. Secondly, the noise floor of the displacement sensor appears as frequency fluctuations proportional to the square of the offset frequency, $P_{\delta f}^{\text{det}}(f) = 5.3 \times 10^{-8} f^2 \text{ Hz}^2/\text{Hz}$ [38]. The calculated jitter,

$$J = \int_0^b (P_{\delta f}^{\text{therm}}(f) + P_{\delta f}^{\text{det}}(f)) \, df = 6.7 \times 10^{-5} \text{ Hz}^2 \tag{5.2}$$

agrees quite well with $8 \times 10^{-5} \text{ Hz}^2$ jitter apparent in Fig. 5.2(c).

The results of a representative hard-axis magnetometry experiment from cantilever C3 are shown in Fig. 5.3. We see that the hard-axis experiment shows numerous, simultaneous transitions in the cantilever spring constant, dissipation and frequency jitter which are entirely absent in the easy-axis data of Fig. 5.2. For the hard-axis experiment at high field $(B \geq B_a)$ we fit the spring constant shift to

$$\Delta k = -\frac{B_{\text{sat}}V}{\mu_0 L_{\text{eff}}^2} \frac{BB_a}{(B - B_a)} \tag{5.3}$$

(see below). The results of the fits to this model are shown in Table 5.1 and are in reasonable agreement with the results of the easy-axis experiments. However, the extracted values for ΔN_{zy} are uniformly smaller than those found in the easy-axis experiment and the values obtained by Aharoni for a rectangular prism[146].

The Δk measured in the hard-axis experiment shows multiple abrupt changes near 0.3 T. The biggest Δk dip is more than ten times larger in magnitude than any shift seen in an easy-axis magnetometry experiment. Moreover, the dips are in many cases only a few mT wide. Some of the Δk peaks show sharp edges (Fig. 5.3, right) and exhibit little or no associated dissipation and jitter; we assign
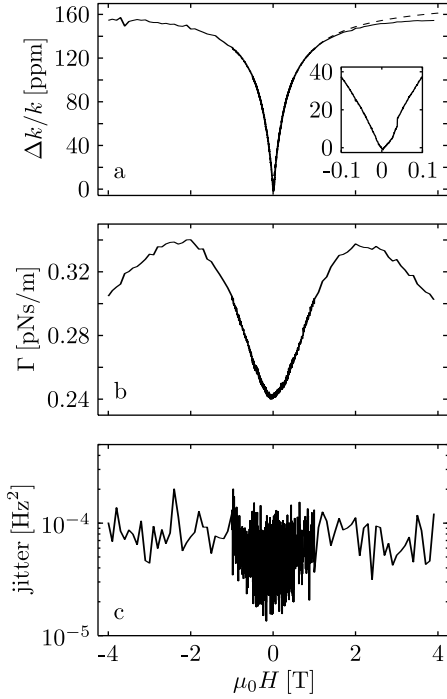
105
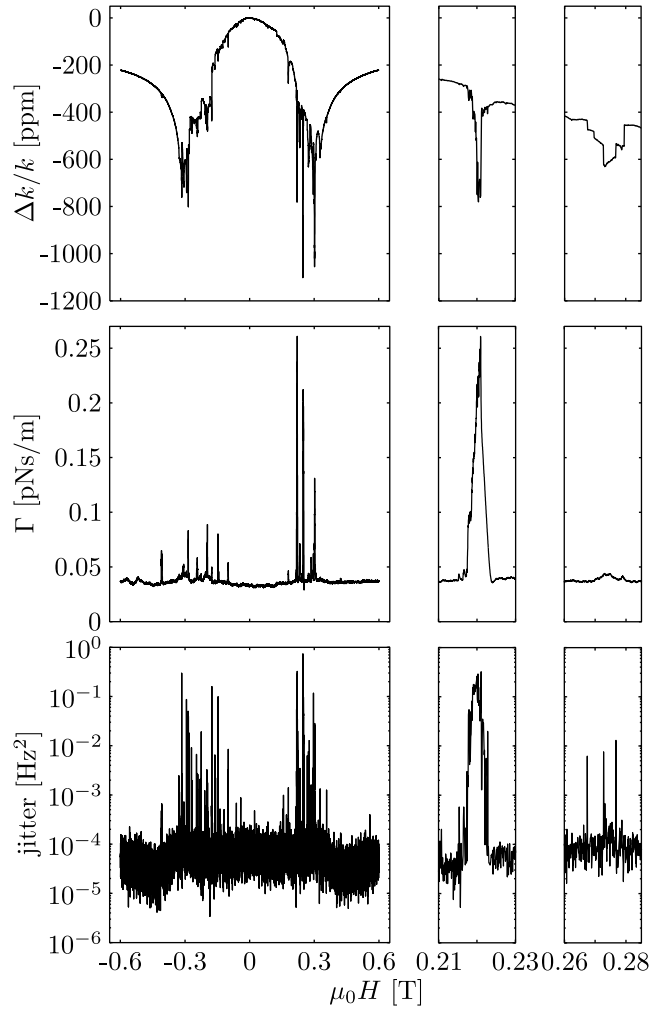
Figure 5.3: Cantilever magnetometry data taken with the field applied along the hard-axis direction of cantilever C3 (z, Fig 5.1(a)), sweeping from -0.6 to $+0.6$ T. Left: Fractional cantilever frequency shift (top) and cantilever dissipation Γ (middle), both showing large discontinuous transitions. Cantilever root-mean-square frequency fluctuation measured in a 15 Hz bandwidth (bottom); note the logarithmic scale and the 10,000-fold variation. Right: expanded view of two transitions. The magnetic field was swept at a rate of 0.1 to 0.2 mT s^{-1} and the cantilever frequency, dissipation, and jitter were measured every 0.5 s.
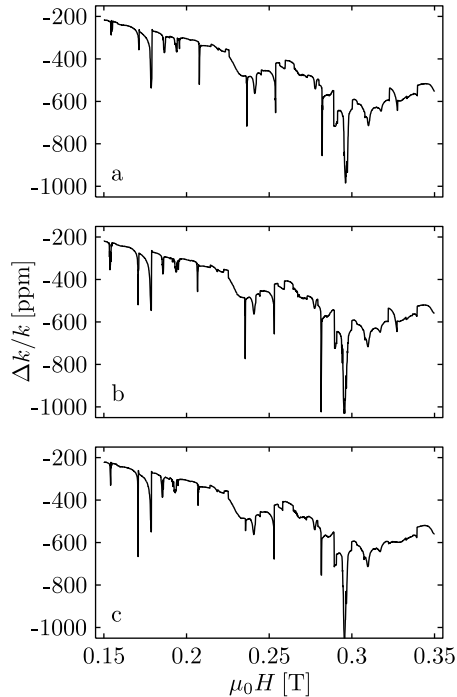
Figure 5.4: Cantilever magnetometry data from cantilever C3, with the magnetic field applied along the hard-axis. The magnetic field was swept from 0.15 T to 0.35 T, with the remainder of the hysteresis loop swept between sequential, (a) to (c), runs. The depth of the Δk dips show run to run variability. For example, the depth of the sharp dip near $\mu_0 H = 0.17$ T grows from (a) $\Delta k = -357$ ppm to (b) -519ppm and (c) -666ppm. Other features, such as the bump near $\mu_0 H = 0.322$T in (a) and (b) disappear entirely in (c).

these peaks to domain wall depinning (Barkhausen noise). Most Δk dips *did* show a simultaneous peak in dissipation.

If the hysteresis loop is run repeatedly, the Δk curve shows some run to run variability in dip depth and width, as show in Fig. 5.4. The location of each individual dip is relatively robust from run to run, as long as the sweep rate is unchanged, but does exhibit variability at a level below what is easily discerned from the plot. Attempts to stop the field sweep on one of the Δk dips where unsuccessful, in part due to the movement of the Δk dips. Additionally, our current experimental apparatus cannot sweep slower than 0.02 mT/s which does not allow our software frequency demodulator to detect the dip fast enough to stop

the sweep before the dip has been passed.

To rule out in-plane switching or domain motion caused by a small in-plane component of the applied field as the source of the Δk dips, the experiment of Fig. 5.3 was reproduced with the applied field angle intentionally misaligned from the hard axis by 2° and 4°, Fig. 5.5. This range of angles is much larger than our estimated uncertainty in angle of ±0.5°. If the field is misaligned from the hard axis by an amount θ the component along the easy axis will be $B_\perp = B \sin \theta$, which for small θ is approximately $B\theta$. If the Δk dips were due to in-plane switching we would expect the magnetization to switch at a field that makes $B_\perp = B_a$. This condition is met when the external field is

$$B = \frac{B_a}{\sin \theta} \approx \frac{B_a}{\theta}. \tag{5.4}$$

However, Fig. 5.5 clearly shows that although the observed Δk dips were smaller with the field misaligned, they were still present and centered near $B_a = 0.3$ T, inconsistent with in-plane switching caused by the small in-plane component of the external field. We also note that moving from 0° to 2° of misalignment eliminated most of the smaller Barkhausen events.

In Fig. 5.3 we identified two kinds of Δk features distinguishable by the presence or lack of increased dissipation. Fig. 5.6 demonstrates that these two types of features are also distinguishable by their dependence on cantilever amplitude. In the left plot of Fig. 5.6 one feature of each type is visible, a small step in the Δk at higher field that does not show a corresponding increase in cantilever dissipation and a large Δk dip that does have an accompanying increasing in dissipation. As shown in Fig. 5.6 the depth of the dissipation accompanied Δk dips are strongly dependent on the cantilever amplitude, while the step-like Barkhausen features showed no amplitude dependence.
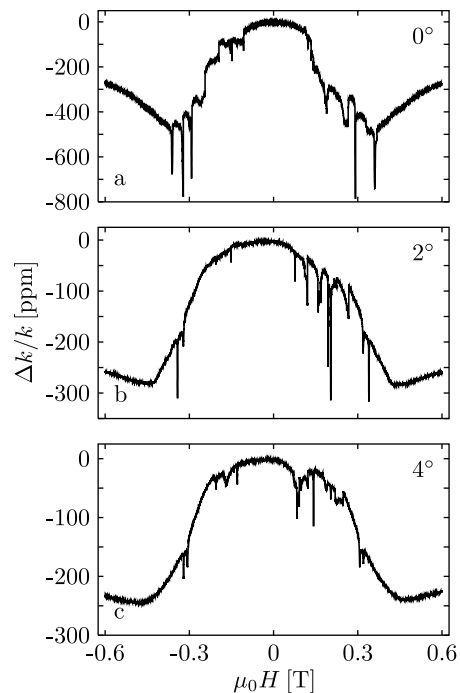
Figure 5.5: Cantilever magnetometry data from cantilever C4 taken with the field applied along the magnetic hard axis, sweeping from −0.6 T to +0.6 T for three different nominal angles between the hard axis and the applied field, (a) 0°, (b) 2° and (c) 4°.

To investigate this amplitude dependence, one would ideally sweep repeatedly through the peak, stepping the cantilever's amplitude between each sweep and holding it constant through a given sweep using a feedback loop. The ideal experiment is problematic because controlling the amplitude of a high-Q oscillator via feedback requires a relatively small feedback bandwidth [147]. Because of the limited field-sweep rates available in our experiment, the cantilever dissipation, and thus the cantilever amplitude, is changing more rapidly than our feedback loop can accommodate. To avoid this feedback problem we instead swept through the frequency dip without a feedback loop controlling the cantilever amplitude and instead used a fixed drive voltage. To generate the data shown in the right plot of Fig. 5.6 we systematically varied the drive voltage, measured the cantilever amplitude and frequency simultaneously, and plotted the resulting peak frequency shift as a function of the cantilever amplitude.

Surprisingly, the Δk dip is largest for small cantilever amplitudes and decreases with increasing cantilever amplitude. This is further evidence that these features are not a result of switching due to the small in-plane component of the magnetic field since the in-plane component is directly proportional to the cantilever amplitude.

5.4   Analysis and Discussion

5.4.1   Spring Constant Shift

In Section 5.3 the spring constant shift from both easy and hard-axis experiments was fit to extract the magnetic moment and anisotropy constant for the magnetic
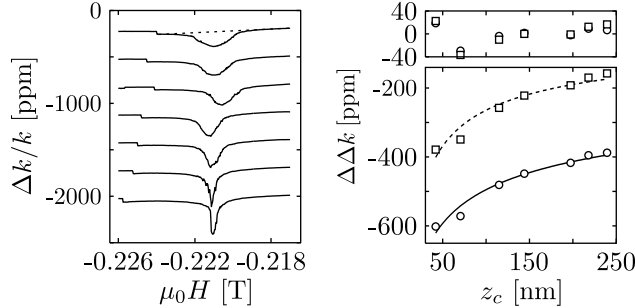
Figure 5.6: Left: Fractional cantilever spring constant shift versus field for cantilever amplitudes ranging from 250 nm (upper trace) to 50 nm (lower trace) for cantilever C2. The data has been offset vertically for clarity. Because the cantilever dissipation is changing too rapidly for the feedback loop to respond in this experiment, a fixed drive amplitude was applied and the magnetic field was swept. Right: Peak cantilever spring constant shift versus cantilever amplitude. The peak shift $\Delta\Delta k$ was computed two ways, Method 1 (circles) and Method 2 (squares), as described in the text. The lines are fits to Eq. 5.24; see text for discussion.

particle. The equations used for the fits were derived from the uniform rotation or Stoner-Wolhfarth model [148], the simplest classical model that predicts hysteresis. The model assumes that the exchange interaction holds all of the microscopic magnetic moments strictly parallel and only the direction of the magnetic moment is free to change. As indicated above, magnetization switching in nickel nanorods of the size studied here is expected to occur via either a curling mechanism[143, 144] or domain wall nucleation and depinning [145] rather than via uniform rotation. However, above the switching field the magnetization is aligned with the external magnetic field and only undergoes small angular deviations ($\theta^{\mathrm{max}} \approx 0.05°$) due to the motion of the cantilever. Uniform rotation should be a good model for the magnetization dynamics of our magnetic nanorods in this limit.

The energy of a single domain particle with uniaxial anisotropy is

$$U(B,\theta) = -\mu B \cos(\theta - \theta_m) + \frac{\mu_0 \mu^2}{2V} \left(N_y \cos^2\theta_m + N_z \sin^2\theta_m \right) \qquad (5.5)$$

$$= -\mu B \cos(\theta - \theta_m) - \frac{\mu B_a}{2} \cos^2\theta_m + \frac{\mu B_a}{2} \frac{N_z}{N_z - N_y} \qquad (5.6)$$

111

where μ and V are the magnetic moment and volume of the particle, respectively, B is the magnitude of the applied magnetic field, $B_a = \mu_0\mu(N_z - N_y)/V$ is the anisotropy field with N_y and N_z the easy and hard-axis demagnetization factors, respectively. The applied magnetic field is oriented at an angle θ and the magnetic moment is oriented at an angle θ_m both relative to the particle's long (e.g. easy) axis. The third term in Eq. 5.6 is a constant and for our purposes can be neglected. It will be more convenient to rewrite Eq. 5.6 in a unitless form by dividing through by $U_0 = \mu B_a/2$, and defining the reduced external field, $\alpha = B/B_a$,

$$U_m = \frac{U}{U_0} = -2\alpha\cos(\theta - \theta_m) - \cos^2\theta_m. \tag{5.7}$$

For the easy-axis experiment the external magnetic field is aligned with the magnetic particle's easy-axis and $\theta = 0$. As the cantilever displaces by an amount δz from its equilibrium position the angle that the external field makes with the easy axis will change by an amount $\delta\theta = \delta z/L_{\text{eff}}$ and we assume that the magnetization reorients continuously to minimize U. Substituting $\theta = 0 + \delta\theta$ and $\theta_m = 0 + \delta\theta_m$ into Eq. 5.7, minimizing with respect to $\delta\theta_m$ in the limit that $\delta\theta \ll 1$ and $\delta\theta_m \ll 1$ we find

$$-2\alpha(\delta\theta - \delta\theta_m) + 2\theta_m = 0 \tag{5.8}$$

which can be solved for the value of $\delta\theta_m$ that minimizes the energy for a given $\delta\theta$. This optimal $\delta\theta_m$ is

$$\delta\theta_m^{\text{opt}} = \frac{\alpha}{\alpha + 1}\delta\theta. \tag{5.9}$$

As the cantilever rotates, the nanorod interacts with the external field to produce a restoring torque on the cantilever, $\tau_x = -\partial U/\partial\delta\theta$ that acts to curl the end of the cantilever. This torque is kinematically equivalently to a point force $F_z = \tau_x/L_{\text{eff}}$ acting on the tip of the cantilever. We observe a frequency shift which

requires F_z to be position dependent. Approximating F_z by the first position dependent term of its Taylor expansion about the equilibrium position, $\delta z = 0$, we have $F_x \approx (\partial F_z / \partial \delta z) \delta z$ (Eq. 3.5). We recognize this as having the same form as Hooke's Law and define $k_{\mathrm{mag}} \equiv -\partial F_z / \partial \delta z$ to be the magnetic contribution to the cantilever's spring constant. Using the definitions for F_z, τ_x and $\delta \theta$, k_{mag} is related to the optimized energy of the magnetic nanorod by

$$k_{\mathrm{mag}} = \frac{U_0}{L_{\mathrm{eff}}^2} \left. \frac{\partial^2 U_m^{\mathrm{opt}}}{\partial \, \delta\theta^2} \right|_{\delta\theta = \delta\theta_{\mathrm{eq}}}. \tag{5.10}$$

Inserting Eq. 5.9 into Eq. 5.7 and applying Eq. 5.10 we find

$$k_{\mathrm{mag}} = \frac{\mu}{L_{\mathrm{eff}}^2} \frac{BB_a}{B + B_a} \tag{5.11}$$

for the magnetic contribution to the spring constant in the easy-axis case, in agreement with previous work [29, 56, 149].

In the hard-axis experiment, the external magnetic field is aligned with the particle's hard axis and $\theta = \pi/2$. As indicated above, the Stoner-Wolhfarth model only applies to our system in the limit $\theta_m \ll 1$, a condition not met until the external field has become strong enough to align the magnetization along the field. This condition occurs in the hard-axis experiment when $B \approx B_a$. Above $B = B_a$ (or $\alpha = 1$), $\theta = \pi/2 + \delta\theta$ and $\theta_m = \pi/2 + \delta\theta_m$. Making these substitutions, Eq. 5.7 becomes

$$U_m = -2\alpha \cos(\delta\theta - \delta\theta_m) - \sin^2 \theta_m. \tag{5.12}$$

As above, minimizing this expression with respect to $\delta\theta_m$ yields the optimized magnetization angle

$$\delta\theta_m^{\mathrm{opt}} = \frac{\alpha}{\alpha - 1} \delta\theta. \tag{5.13}$$

Inserting this back into Eq. 5.12 and applying Eq. 5.10,

$$k_{\mathrm{mag}} = -\frac{\mu}{L_{\mathrm{eff}}^2} \frac{BB_a}{B - B_a} \tag{5.14}$$

for the magnetic contribution to the spring constant at high field.

Although we know that the uniform rotation model does not apply to the nanorods studied here below $B = B_a$, an expression for magnetic contribution to the spring constant in this limit can be derived. Using the same techniques as above, we find

$$k_{\mathrm{mag}} = \frac{\mu}{L_{\mathrm{eff}}^2} \frac{B^2}{B_a}. \tag{5.15}$$

Eq. 5.15 predicts that at low field the cantilever's spring constant would increase with the square of the external field, while as shown in Fig. 5.3(a), we observe the spring constant decreasing with roughly the square of the external field. This disagreement is not suprising; we do not expect our particle to behave as a Stoner-Wolhfarth particle at low field.

Earlier work by Miller *et al.* [142] studying much larger CoPt magnets using cantilever-torque magnetometry observed a spring constant shift similar to the envelope of the spring constant shift observed in Fig. 5.3(a). Miller *et al.* did not observe any Δk dips; however, the external field was changed in this experiment by $\sim 0.1\,\mathrm{T}$ between measurements of Δk. The features we observe occur over field ranges covering only millitesla and we would not expect a much coarser field sweep to be able to resolve them.

5.4.2 Amplitude Dependence

As the cantilever displaces by an amount z, the apparent angle of the applied field experienced by the magnetic particle will change by $\delta\theta \approx z/L_{\mathrm{eff}}$. To model the amplitude dependence of the cantilever frequency shift near the switching field B_{sw}, let us take the view that the magnetization of a domain reorients continuously

to minimize energy as the cantilever vibrates, and let us make the ansatz that the energy of the domain is given by, for small angular displacements,

$$U_m = -\mu_d B_{\text{sw}} \, c_\theta \, |\delta\theta|^m \tag{5.16}$$

where μ_d is the magnetic moment of the domain, c_θ is a constant of order one, and the power m will be taken to be greater than zero. In writing Eq. 5.16 we are neglecting hysteresis, for simplicity. The torque associated with this energy is $\tau_x = -\partial U_m / \partial \, \delta\theta$. This torque is kinematically equivalent to a restoring force

$$F_z = \frac{\tau_x}{L_{\text{eff}}} = \pm \frac{\mu_d B_{\text{sw}} \, c_\theta}{L_{\text{eff}}} \left(\frac{z}{L_{\text{eff}}} \right)^{m-1} \tag{5.17}$$

where the $\pm$ signifies that the sign of the force should be positive for $z > 0$ and negative for $z < 0$. We use Hamilton-Jacobi perturbation theory to calculate the perturbation to the cantilever spring constant Δk resulting from the displacement-dependent force[116] of Eq. 5.17:

$$\Delta k = -\frac{2}{z_{0\text{p}}^2} \langle F_z(t) \, z(t) \rangle_{\text{period}} \tag{5.18}$$

where $z_{0\text{p}}$ is the zero-to-peak cantilever amplitude and the $\langle \cdots \rangle$ indicates a temporal average over one cantilever period of duration T. Substituting $z(t) = z_{0\text{p}} \sin\left(2\pi t/T\right)$, and using the fact that the perturbation is an antisymmetric function of the displacement,

$$\Delta k = -\frac{2c_\theta \mu_d B_{\text{sw}}}{z_{0\text{p}}^2} \left(\frac{z_{0\text{p}}}{L_{\text{eff}}} \right)^m \left[\frac{2}{T} \int_0^{T/2} \left\{ \sin(\frac{2\pi t}{T}) \right\}^m dt \right]. \tag{5.19}$$

The integral $[\cdots]$ in Eq. 5.19 is independent of T and can be carried out analytically in terms of the gamma function Γ. The result yields

$$\frac{\Delta k}{k} = -\frac{c_\theta \mu_d B_{\text{sw}}}{k L_{\text{eff}}^m \, z_{0\text{p}}^{2-m}} \frac{4\sqrt{\pi} \sec\left(\frac{m\pi}{2}\right)}{\Gamma(\frac{1-m}{2}) \, \Gamma(\frac{m}{2})}. \tag{5.20}$$

The rightmost fraction in Eq. 5.20 is a slowly varying function of m. For $m = 2$, this equation reduces to $\Delta k/k = 2c_\theta \mu_d B_{\text{sw}}/k L_{\text{eff}}^2$ — independent of cantilever

amplitude, as expected for a potential energy which depends quadratically on the cantilever displacement. For $m < 2$, Eq. 5.20 predicts an amplitude-dependent change in spring constant, in qualitative agreement with experiment.

If the domain acts as a Stoner-Wolhfarth particle, Eq. 5.7 can be used to predict the values of c_θ and m we would expect. Making the substitutions, $\theta = \pi/2 - \delta\theta$ and $\theta_m = \pi/2 - \delta\theta_m$ into Eq. 5.7, setting $\alpha = 1$ and calculating $\partial U_m/\partial\delta\theta_m = 0$, we find

$$0 = \sin(\delta\theta - \delta\theta_m) - \sin\delta\theta_m\cos\delta\theta_m. \tag{5.21}$$

Expanding this to third order in $\delta\theta$ and $\delta\theta_m$ produces a cubic equation, which can be solved to find $\delta\theta_m^{\text{opt}}$. However, $\delta\theta \ll 1$ and the leading term of the solution,

$$\delta\theta_m^{\text{opt}} = (2\delta\theta)^{1/3} \tag{5.22}$$

is a good approximation to the full solution in this limit. Inserting Eq. 5.22 into Eq. 5.7, and expanding in a Taylor series about $\delta\theta = 0$, the potential energy surface at the critical field is

$$U_0 U_m^{\text{opt}} = \frac{\mu_d B_a}{2}\left(-2 - \frac{3}{2^{2/3}}\delta\theta^{4/3}\right)$$
$$\approx -\mu_d B_a \frac{3}{2^{5/3}}\delta\theta^{4/3}. \tag{5.23}$$

From Eq. 5.23, the Stoner-Wolhfarth model predicts $c_\theta = 3/2^{5/3} = 0.945$ and $m = 4/3$.

To analyze the spring-constant dips in Fig. 5.6(left), the depth of the dip was inferred using two methods. In Method 1, the frequency at the bottom of the dip was compared to the cantilever frequency at zero field, and the computed frequency shift converted to an equivalent spring constant shift. In Method 2, in order to account for the background shift arising from already-flipped domains,

Table 5.2: Analysis of Fig. 5.6 data. The reported error bars represent a 95% confidence interval.

value	Method 1	Method 2	unit
κ_{ref}	620 ± 36	401 ± 50	ppm
m	1.740 ± 0.053	1.52 ± 0.13	–
μ_d	4.4 ± 1.9	0.53 ± 0.53	10^{-15} A m^2
N_d	1.3 ± 0.5	11 ± 11	–

the frequency shift at the bottom of the dip was compared to a frequency baseline obtained by fitting the data to either side of the dip to a line (Fig. 5.6, left, dotted line). The shifts computed by Methods 1 and 2 are plotting in Fig. 5.6(right) as circles and squares, respectively.

Following Eq. 5.20, we fit the data of Fig. 5.6(right) to the power-law function

$$\frac{\Delta\Delta k}{k} = -\kappa_{\mathrm{ref}} \left(\frac{z_{\mathrm{ref}}}{z_{\mathrm{0p}}} \right)^{2-m} \tag{5.24}$$

with $z_{\mathrm{ref}} = 41.9$ nm a reference amplitude and κ_{ref} a prefactor representing the relative spring constant shift at the reference amplitude. The domain magnetic moment in Eq. 5.16 is computed from best-fit parameters using

$$\mu_d = \frac{\kappa_{\mathrm{ref}} \, k \, L_{\mathrm{eff}}^m \, z_{\mathrm{ref}}^{2-m}}{c_\theta B_{\mathrm{sw}}} \frac{\Gamma(\frac{1-m}{2}) \, \Gamma(\frac{m}{2})}{4\sqrt{\pi} \sec(\frac{m\pi}{2})}, \tag{5.25}$$

taking $c_\theta = 1$ for simplicity. The standard error in the domain magnetic moment, which depends on the error in both the prefactor and the power, is computed numerically as $\sigma_{\mu_d} = ((\partial\mu_d/\partial\kappa_{\mathrm{ref}})^2 \sigma_{\kappa_{\mathrm{ref}}}^2 + (\partial\mu_d/\partial m)^2 \sigma_m^2)^{1/2}$. The number of domains in the tip, N_d, is computed by dividing the total tip magnetic moment reported for cantilever C2 in Table 5.1 by μ_d.

Fitting results are presented in Table 5.2. The Method 1 data, when analyzed in terms of the model of Eq. 5.20, give a domain magnetic moment which is too large. The domain parameters extracted from the Method 2 data, in contrast,

predict a number of domains (0 to 22) in good agreement with the total number of frequency dips seen in Figs. 5.3 and 5.4. In spite of the large uncertainty in the domain magnetic moment inferred from the Method 2 data, we can nevertheless conclude that the domains giving rise to the frequency dips seen in 5.3 and 5.4 are well described by Eq. 5.16 with $m = 1.52 \pm 0.13$, in reasonable agreement with $m = 1.33$ predicted from the Stoner-Wolhfarth model.

5.4.3 Dissipation

Field-dependent dissipation, Fig. 5.3(middle), in a cantilever magnetometry experiment arises from transverse magnetization fluctuations [56, 57]. For a field oriented as in Fig. 5.1(a), fluctuations in magnetization angle give rise to a fluctuating x-axis torque $\delta\tau_x(t) = \delta\mu_y(t)\, B$. This torque is kinematically equivalent to a fluctuating z-axis force of magnitude $\delta F_z(t) = \delta\tau_x(t)/L_{\text{eff}}$. This force will lead to a dissipation $\Gamma_m = P_{\delta F_z}(f_c)/4k_bT$ with $P_{\delta F_z}(f)$ the one-sided power spectrum of force fluctuations and f_c the cantilever frequency [56, 57]. It follows that the nanorod's contribution to the cantilever's dissipation is

$$
\begin{aligned}
\Gamma_m &= \frac{B^2}{4k_BTL_{\text{eff}}^2}P_{\delta\mu_y}(f_c) \\
&= \frac{\mu^2 B^2}{4k_BTL_{\text{eff}}^2}P_{\delta\theta_m}(f_c)
\end{aligned}
\tag{5.26}
$$

where we have used $\delta\mu_y = \mu\sin\delta\theta_m \approx \mu\,\delta\theta_m$. The existence of dissipation peaks thus requires multiple domains having a magnetic potential energy function with states of many different magnetization angles thermally populated near ~ 0.3 T. One such potential is shown in Fig. 5.7. In Fig. 5.7 we plot the potential energy U_m (Eq. 5.7) of a Stoner-Wolhfarth particle for increasing field applied along the particle's hard axis. The potential has two degenerate minima at angles $\theta_m^{\pm} =$
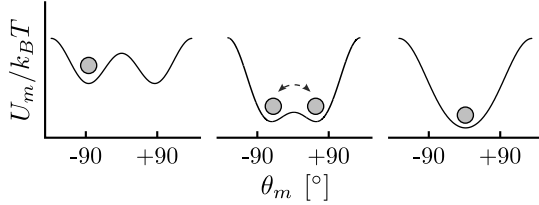
Figure 5.7: Potential energy of magnetization as a function of magnetization angle θ_m. The field, which is applied along the z axis of Fig 5.1(a), increases from left to right.

$\pm \arccos(\alpha)$. The barrier between the minima is $\Delta U_m = U_0(1 - \alpha)^2$. This barrier goes to zero at $B = B_a$.

We can use this uniform rotation model to derive a closed form expression for the height of the dissipation peaks seen in Fig. 5.3(middle). Let us approximate the angular fluctuations as arising from thermally-activated magnetization hops between these two degenerate minima. For simplicity, we take the associated correlation function to be

$$C_{\delta\theta_m}(t) = (2 \arccos(\alpha))^2 e^{-t/\tau_m} \tag{5.27}$$

where the hopping time is

$$\tau_m = \tau_0 e^{\Delta U_m / k_B T} \tag{5.28}$$

and the inverse attempt frequency is $\tau_0 \sim 10^{-9}$ s. Computing $P_{\delta\theta_m}(f)$ by taking the Fourier transform of $C_{\delta\theta_m}(t)$, we find for the peak dissipation

$$\Gamma_m^{\text{pk}} = \frac{0.150}{\sqrt{-\ln(2\pi f_c \tau_0)}} \frac{B_{\text{sat}}^2 V \Delta N_{zy}}{f_c L_{\text{eff}}^2 \mu_0} \left(\frac{B_{\text{sat}}^2 V \Delta N_{zy}}{\mu_0 k_B T} \right)^{1/2} \tag{5.29}$$

Eq. 5.29 predicts a $\Gamma_m^{\text{pk}} \approx 0.2$ pN s/m for a single domain having a high aspect ratio, $\Delta N_{zy} = 0.5$ and a volume of $V \sim (30\,\text{nm})^3$. Performing this analysis on all sharp Δk dips, we estimate that approximately 3% of the nanorod's volume gives rise to the sharp, dissipation accompanied Δk dips we observe.

119

The original impetus for performing the hard-axis magnetometry experiment was to probe the magnetization of the nanorod when magnetized out-of-plane. We were interested in this because using a batch fabricated magnetic tip in the SPAM geometry [29] requires magnetizing it along along one of its hard axes. However, the point of using the SPAM geometry is that the tip-field interaction does not change the spring constant or cause large field induced dissipation. Although this is convenient experimentally, it also means the magnetization of the tip cannot be probed *in situ*. Our ESR experiments take place near $B = 0.6$ T and we were concerned that the magnetization of the nanorod would not be saturated. Earlier work [56, 57] indicated that there are two regimes in which magnetization fluctuations in the magnetic tip will not deleteriously effect the spin relaxation rates of the sample spins. One can operate with a tip made of a hard magnetic material, such as samarium-cobalt, at low magnetic fields [56], as was done in the single-spin experiment [28] or with a tip made from a soft magnetic material, such as nickel, in a high magnetic field [57]. The experiment described in Chapter 3 using a nickel tip like those studied here took place at low field and magnetization fluctuations effecting T_1 were a concern.

Even though we cannot observe them, the magnetization dynamics that produce the Δk dips and dissipation peaks still occur in the SPAM geometry. Instead of calculating the size of the dissipation peak as above, it is useful to convert the measured dissipation into a fluctuating magnetic field and ask how it will effect spin relaxation in a nearby sample. At B_{sw}, the power spectral density of magnetic moment fluctuations giving rise to a dissipation peak is thus

$$P_{\delta\mu_y}(f_c) = \frac{4k_b T L_{\mathrm{eff}}^2}{B_{\mathrm{sw}}^2}\,\Gamma_m. \tag{5.30}$$

For a dissipation peak with $\Gamma_m = 0.25 \times 10^{-12}\mathrm{Nsm}^{-1}$, $B_{\mathrm{sw}} = 0.221\mathrm{T}$, and $T = 4.2\mathrm{K}$, we compute $P_{\delta\mu_y}(f_c) = 2.6 \times 10^{-42}\ \mathrm{A}^2\ \mathrm{m}^4\ \mathrm{Hz}^{-1}$. Modeling the fluctuating domain

as a dipole, the resulting power spectral density of magnetic field fluctuations at a distance r from the domain is

$$P_{\delta B_y}(f_c) = \left(\frac{\mu_0}{\pi \, r^3}\right)^2 P_{\delta \mu_y}(f_c). \tag{5.31}$$

At $r = 220$ nm, where the field from the dipole is estimated to be 0.20 T, we calculate $P_{B_y}(f_c) = 3.6 \times 10^{-12}$ T^2 Hz^{-1}. Since $f_c \sim$ few kHz is similar to the Rabi frequency in a magnetic resonance experiment, the magnetic fluctuations underlying the dissipation peaks in Fig. 5.3 are at the right frequency to affect $T_{1\rho}$, the spin-lattice relaxation time in the rotating frame [57]. The associated spin relaxation rate, $\gamma_j^2 P_{B_y}$ with γ_j the gyromagnetic ratio, evaluates to 15 ms for protons and 0.4 ns for electrons. This calculation indicates that efficient relaxation of sample spins in a magnetic resonance experiment could be induced by adjusting the external field to coincide with one of the dissipation peaks in Fig. 5.3. The dissipation peaks are only a few gauss wide, suggesting that rapid modulation of sample relaxation times could be achieved.

5.4.4 Angle Dependence

Fig. 5.5 shows the relative spring constant change for three different angles between the external magnetic field and the hard-axis of the nanorod. Although the δk dips did not move from near 0.3 T, they did become much less deep as the field was misaligned. To investigate the dependence of the Δk depth on the external field angle, we calculated the spring constant change numerically. Our procedure was very similar to that used above—at given values of α and θ the value of θ_m that minimized the energy was found by setting $\partial U_m / \partial \theta_m = 0$ and locating the root using bisection and Newton's method, starting from the previous value of θ_m. The
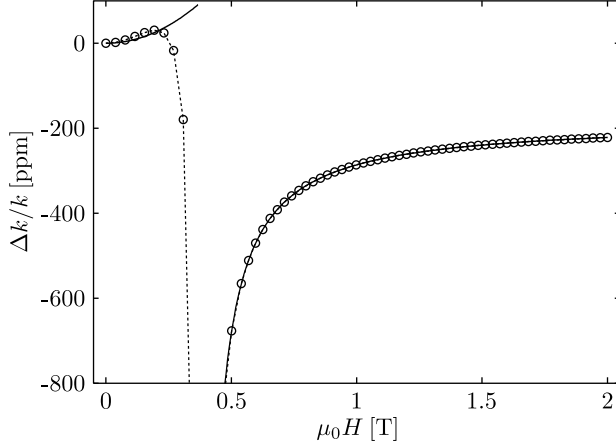
Figure 5.8: Numerical calculation of the relative spring constant change for cantilever C1. The numerical results are shown as open circles, and the analytic results, Eqs. 5.14 and 5.15, shown as solid lines; the dotted line is a guide for the eye. The numeric routine recovers the analytic results.

motion of the cantilever was included by letting θ range between $\pi/2 \pm z_{\max}/L_{\mathrm{eff}}$. The force on the cantilever was calculated using $F_z = -L_{\mathrm{eff}}^{-1}\partial U_m/\partial\theta$ and the spring constant change calculated using Hamiltonian-Jacobi perturbation theory.

As a first test of our numerical routine, we calculated the spring constant change for cantilever C1 with the external magnetic field aligned with the hard axis, $\theta = \pi/2$. The results are plotted in Fig. 5.8; the numerical results are shown as circles and Eqs. 5.14 and 5.15 shown as solid lines. Our numerical routine recovers the analytic results derived above.

The calculated relative spring constant change is shown in Fig. 5.9, for the external field aligned with the hard-axis and for four different misalignments, $0.01°$, $0.03°$, $0.05°$ and $2.00°$. The domain giving rise to the peak was taken to be nickel with a volume $V = (50\mathrm{nm})^3$ and difference in demagnetization factors $\Delta N_{zy} = 0.5$. The calculated δk depth is a much stronger function of misalignment angle that we observe experimentally, dropping to only 38% after $0.05°$ of misalignment. With $2°$ of misalignment, the Δk dip is nearly gone, reduced to 2% of its original value.
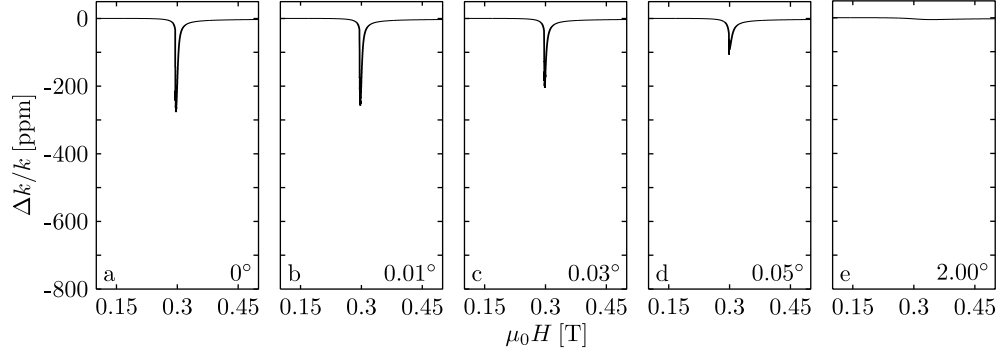
122

Figure 5.9: Results of numerically calculating the depth of the Δk dip with the external field misaligned from $\theta = \pi/2$ by (a) 0°, (b) 0.01°, (c) 0.03°, (d) 0.05°, and (e) 2°. The depth of the Δk dip decreases rapidly with only small angular misalignments, from an initial depth of -276.9 ppm in (a) to -257.2 ppm in (b), to -205.3 ppm in (c), to -106.4 ppm in (d) and -5.4 ppm in (e). The sensitivity to small misalignments is much stronger than we observe experimentally, as shown in Fig. 5.5.

The dip depth is very a very sensitive function of angle in this model because near the critical field $(B = B_a)$ the magnetization is being coherently pumped back and forth between the two minima by the motion of the cantilever. For a cantilever amplitude, $z_{0p} = 131$ nm, the nanorod only rotates by 0.05° and angular misalignments on that order are all that is required to disrupt the magnetization oscillation. Experimentally, we observe Δk dips even at 4° of field misalignment. We interpret this to mean that different domains produce the Δk dips observed at each field angle. This conclusion is reasonable given the above estimate that the Δk dips we observe are produced by between 0 and 22 domains. A second corroborating estimate, from analysis of the dissipation data, is that the dissipation peaks we observe account for only 3% of the total volume of the magnet. Our numerical model assumes that the magnetization is restricted to the yz-plane; extending the numerical model from modeling a prolate spheroid to a general triaxial ellipsoid should be straight forward.

5.5 Conclusions

In summary, we have observed dramatic changes in cantilever spring constant, dissipation, and frequency jitter in a cantilever magnetometry study of in-plane to out-of-plane magnetization switching in a single nickel nanorod. Many of these features are robust toward angular deviations of up to a few degrees, and show a strong dependence on cantilever amplitude. These findings are quite general, having been observed for every nanorod tipped cantilever we have investigated to date, spanning approximately two years and including extensive changes in the cantilever and nanorod fabrication process during that time [62, 109].

We derived a model for the changes in the cantilever spring constant above the anisotropy field by treating the nanorod as a Stoner-Wolhfarth particle, and find reasonable agreement between the model and the experimental results. An estimate for the active volume from the amplitude dependence of a single Δk dip is consistent with the presence of multiple dips, and the estimated active volume is comparable to the grain size of our nanorods as estimated using STEM.

The existence of multiple weakly coupled volumes within the nanorod that switch quasi-independently could be explained by the presence of crystalline domains (Fig. 5.1(d)), spatial variations in the nickel thickness, or the templating of magnetization by an antiferromagnetic nickel oxide coating. There is precedent for observing magnetization switching in nickel nanorods via thermally-activated coherent rotation in magnetic force microscopy, [143] anisotropic magnetoresistance [150], and SQUID [144] magnetometry. The grain size was much smaller in the nickel films used in these prior studies, which may explain why they did not observe switching via distinct intermediate states as seen here. Whatever the underlying mechanism, the results of Fig. 5.3 suggest a new method for creating giant tunable

magnetic field fluctuations and for mechanically detecting magnetic fields at high sensitivity and nanoscale spatial resolution [35, 36, 61].

APPENDIX A

B_1 MAGNITUDE REQUIRED TO SATURATE USING THE SMALL MAGNETIC TIP

We want to estimate how large a B_1 will be required to saturate in an experiment using a small magnetic tip. In Chapter 3, we argued that the steady state solutions to the Bloch equations were an inadequate model for the magnetization in the small tip experiment because the spins did not remain in the sensitive slice long enough to reach steady state. Here we will extend this argument to estimate the necessary transverse field magnitude for reaching the steady state using a small magnetic tip.

In Chapter 3, we estimated the thickness of the instantaneous resonant slice to be

$$\Delta x_{\mathrm{sat}} = \frac{2\pi}{\gamma G T_2} \tag{A.1}$$

$$= \frac{\Delta B}{G} \tag{A.2}$$

where γ is the gyromagnetic ratio, $G = \partial B_z / \partial x$ is the tip field gradient, T_2 is the spin-spin relaxation time and ΔB is the resonance linewidth in units of magnetic field. Eq. A.2 is the correct thickness of the resonant slice in the limit $B_1 \ll \Delta B$. If B_1 is larger than ΔB, Eq. A.2 should be rewritten as

$$\Delta x_{\mathrm{sat}}^{\mathrm{strong}\ B_1} = \frac{B_1}{G}. \tag{A.3}$$

In Chapter 3 we proposed that the steady state solution applies in the limit $\Delta x_{\mathrm{sat}} \gg \Delta x_{\mathrm{osc}}$ where $\Delta x_{\mathrm{osc}} = v T_{\mathrm{sat}}$ and $v = 2\pi f_c x_{\mathrm{pk}}$ is the cantilever velocity. Using Eq. A.3 and setting $T_{\mathrm{sat}} = 2T_2 = 2 \times 500$ ns, $G = 40$ G/nm, $f_c = 7374$ Hz

and $x_{\mathrm{pk}} = 40$ nm, as in Chapter 3, we calculate that $B_1 \geq 74$ G is necessary to reach $\Delta x_{\mathrm{sat}} \geq \Delta x_{\mathrm{osc}}$.

The B_1 estimated above is far to large because it assumes that the spin must saturate completely during the time it remains in the sensitive slice. However, the spin moves in and out of the sensitive slice faster than T_1 which means that we can saturate some, then recover some and eventually saturate completely using a much smaller B_1. Using the Bloch equations, Torrey has shown, for an ensemble exactly on resonance, the $1/e$ saturation time is

$$T_{\mathrm{sat}} = \frac{2T_1 T_2}{T_1 + T_2},\tag{A.4}$$

which in our limit of $T_1 \gg T_2$ is the $T_{\mathrm{sat}} = 2T_2$ used above [118]. Let us assume the magnetic field at the spin is

$$B_z(t) = B_0 + G x_{\mathrm{pk}} \sin(2\pi f_0 t)\tag{A.5}$$

and the resonance condition is met when $B_z(t) = B_0$. Further, we will assume that when $|B_z(t) - B_0| \leq B_1$ the magnetization is exactly on resonance. The magnetization will spent a time

$$t_{\mathrm{on}} = \frac{B_1}{\pi f_0 G x_{\mathrm{pk}}}\tag{A.6}$$

on resonance for every half cantilever cycle, where we have used $t_{\mathrm{on}} \ll T_c$. During t_{on} the magnetization will decay exponentially with T_{sat}. During the remaining half cycle, $t_{\mathrm{recover}} = T_c/2 - t_{\mathrm{on}}$ the z magnetization will recover with T_1. As long as

$$-\Delta M_{\mathrm{on}} > \Delta M_{\mathrm{recover}}\tag{A.7}$$

where ΔM_{on} and $\Delta M_{\mathrm{recover}}$ are the change in magnetization during t_{on} and t_{recover}, respectively, the system will eventually reach a mildly oscillating saturated state.

For our system we expect $t_\text{on} \ll T_\text{sat}$ and $t_\text{recover} \ll T_1$, which will allow us to approximate the exponential growth (ΔM_recover) and exponential decay (ΔM_on) in Eq. A.7 by the first two terms of their Taylor expansions,

$$\frac{t_\text{on}}{T_\text{sat}} > \frac{t_\text{recover}}{T_1}. \tag{A.8}$$

Inserting the above values for t_on and t_recover, rearranging to solve for B_1 we find,

$$B_1 > \frac{\pi f_0 G x_\text{pk} T_c T_\text{sat}}{2(T_1 + T_\text{sat})}. \tag{A.9}$$

Inserting our values from above in to Eq. A.9, we find $B_1 > 2.2$ G. A transverse field this large should be experimentally accessible, although depending on the details of the spin location and cantilever amplitude, this may also be enough B_1 to perform OSCAR-style spin flips, providing a $2\times$ enhancement in the size of the spin signal.

BIBLIOGRAPHY

[1] E. K. Zavoisky, J. Phys. USSR **9**, 245 (1944).

[2] F. Bloch, W. W. Hansen, and M. Packard, Nuclear induction, Phys. Rev. **69**, 127 (1946).

[3] E. M. Purcell, H. C. Torrey, and R. V. Pound, Resonance absorption by nuclear magnetic moments in a solid, Phys. Rev. **69**, 37 (1946).

[4] P. C. Lauterbur, Image formation by induced local interactions: Examples employing nuclear magnetic resonance, Nature **242**, 190 (1973).

[5] P. Mansfield and P. K. Grannell, NMR "diffraction" in solids?, J. Phys. C **6**, L422 (1973).

[6] J. A. Sidles, Noninductive detection of single-proton magnetic resonance, Appl. Phys. Lett. **58**, 2854 (1991).

[7] I. Lee et al., Nanoscale scanning probe ferromagnetic resonance imaging using localized modes, Nature **466**, 845 (2010).

[8] H.-J. Chia et al., Dynamical measurements with a nuclear magnetic resonance force microscope, J. Appl. Phys. **105**, 07D531 (2009).

[9] F. Xue, P. Peddibhotla, M. Montinaro, D. P. Weber, and M. Poggio, A geometry for optimizing nanoscale magnetic resonance force microscopy, Appl. Phys. Lett. **98**, 163103 (2011).

[10] K. Wago et al., Magnetic resonance force detection and spectroscopy of electron spins in phosphorus-doped silicon, Rev. Sci. Instrum. **68**, 1823 (1997).

[11] G. P. Berman, G. D. Doolen, P. C. Hammel, and V. I. Tsifrinovich, Solid-state nuclear-spin quantum computer based on magnetic resonance force microscopy, Phys. Rev. B **61**, 14694 (2000).

[12] G. P. Berman, G. D. Doolen, P. C. Hammel, and V. I. Tsifrinovich, Magnetic resonance force microscopy quantum computer with tellurium donors in silicon, Phys. Rev. Lett. **86**, 2894 (2001).

[13] P. Rabl et al., Strong magnetic coupling between an electronic spin qubit and a mechanical resonator, Phys. Rev. B **79**, 041302 (2009).

[14] P. F. Lindley, The use of synchrotron radiation in protein crystallography, Radiat. Phys. Chem. **45**, 367 (1995).

[15] D. A. Snyder et al., Comparisons of NMR spectral quality and success in crystallization demonstrate that NMR and X-ray crystallography are complementary methods for small protein structure determination, J. Am. Chem. Soc. **127**, 16505 (2005).

[16] S. G. Zech, A. J. Wand, and A. E. McDermott, Protein structure determination by high-resolution solid-state NMR spectroscopy: Application to microcrystalline ubiquitin, J. Am. Chem. Soc. **127**, 8618 (2005).

[17] A. Loquet et al., 3D structure determination of the Crh protein from highly ambiguous solid-state NMR restraints, J. Am. Chem. Soc. **130**, 3579 (2008).

[18] C. Wasmer et al., Amyloid fibrils of the HET-s(218–289) prion form a β solenoid with a triangular hydrophobic core, Science **319**, 1523 (2008).

[19] C. Altenbach, T. Marti, H. G. Khorana, and W. L. Hubbell, Transmembrane protein structure - Spin labeling of bacteriophodopsin mutants, Science **248**, 1088 (1990).

[20] W. L. Hubbell, A. Gross, R. Langen, and M. A. Lietzow, Recent advances in site-directed spin labeling of proteins, Curr. Opin. Struct. Biol. **8**, 649 (1998).

[21] P. P. Borbat, A. J. Costa-Filho, K. A. Earle, J. K. Moscicki, and J. H. Freed, Electron spin resonance in studies of membranes and proteins, Science **291**, 266 (2001).

[22] O. Schiemann et al., A PELDOR-based nanometer distance ruler for oligonucleotides, J. Amer. Chem. Soc. **126**, 5722 (2004).

[23] P. P. Borbat, J. H. Davis, S. E. Butcher, and J. H. Freed, Measurement of large distances in biomolecules using double-quantum filtered refocused electron spin-echoes, J. Am. Chem. Soc. **126**, 7746 (2004).

[24] N. J. Malmberg and J. J. Falke, Use of EPR power saturation to analyze the membrane-docking geometries of peripheral proteins: Applications to C2 domains, Ann. Rev. of Biophys. and Biomolec. Struct. **34**, 71 (2005).

[25] S. Y. Park et al., Reconstruction of the chemotaxis receptor-kinase assembly, Nat. Struct. Mol. Biol. **13**, 400 (2006).

[26] Q. Cai et al., Site-directed spin labeling measurements of nanometer distances in nucleic acids using a sequence-independent nitroxide probe, Nucleic Acids Res. **34**, 4722 (2006).

[27] A. Blank and J. H. Freed, ESR microscopy and nanoscopy with "induction" detection., Israel Journal of Chemistry **46**, 423 (2006).

[28] D. Rugar, R. Budakian, H. J. Mamin, and B. W. Chui, Single spin detection by magnetic resonance force microscopy, Nature **430**, 329 (2004).

[29] J. A. Marohn, R. Fainchtein, and D. D. Smith, An optimal magnetic tip configuration for magnetic-resonance force microscopy of microscale buried features, Appl. Phys. Lett. **73**, 3778 (1998).

[30] D. D. Smith, J. A. Marohn, and L. E. Harrell, Detailed description of a compact cryogenic magnetic resonance force microscope, Rev. Sci. Instrum. **72**, 2080 (2001).

[31] S. Kuehn, R. F. Loring, and J. A. Marohn, Dielectric fluctuations and the origins of noncontact friction, Phys. Rev. Lett. **96**, 156103 (2006).

[32] S. Kuehn, J. A. Marohn, and R. F. Loring, Noncontact dielectric friction, J. Phys. Chem. B **110**, 14525 (2006).

[33] S. A. Hickman et al., Batch-fabrication of cantilevered magnets on attonewton-sensitivity mechanical oscillators for scanned-probe nanoscale magnetic resonance imaging, ACS Nano **4**, 7141 (2010).

[34] L. E. Harrell, K. R. Thurber, and D. D. Smith, Cantilever noise in off-cantilever-resonance force-detected nuclear magnetic resonance, J. Appl. Phys. **95**, 2577 (2004).

[35] C. L. Degen, M. Poggio, H. J. Mamin, C. T. Rettner, and D. Rugar, Nanoscale magnetic resonance imaging, Proc. Natl. Acad. Sci. **106**, 1313 (2009).

[36] E. W. Moore et al., Scanned-probe detection of electron spin resonance from a nitroxide spin probe, Proc. Natl. Acad. Sci. **106**, 22251 (2009).

[37] E. W. Moore, S. Lee, S. A. Hickman, L. E. Harrell, and J. A. Marohn, Evading surface and detector frequency noise in harmonic oscillator measurements of force gradients, Appl. Phys. Lett. **97**, 044105 (2010).

[38] T. R. Albrecht, P. Grütter, D. Horne, and D. Rugar, Frequency-modulation detection using high-Q cantilevers for enhanced force microscope sensitivity, J. Appl. Phys. **69**, 668 (1991).

[39] B. C. Stipe et al., Electron spin relaxation near a micron-size ferromagnet, Phys. Rev. Lett. **87**, 277602 (2001).

[40] K. C. Fong, P. Banerjee, Y. Obukhov, D. V. Pelekhov, and P. C. Hammel, Manipulating spins by cantilever synchronized frequency modulation: A variable resolution magnetic resonance force microscope, Appl. Phys. Lett. **93**, 012506 (2008).

[41] S. G. Lee, S. Won, S. b. Saun, and S. Lee, Magnetic resonance force microscopy in fast-relaxing spins using a frequency-modulation mode detection method, Nanotechnology **18**, 375505 (2007).

[42] S. R. Garner, S. Kuehn, J. M. Dawlaty, N. E. Jenkins, and J. A. Marohn, Force-gradient detected nuclear magnetic resonance, Appl. Phys. Lett. **84**, 5091 (2004).

[43] S. Kuehn, *Force-gradient detected nuclear magnetic resonance and the origins of noncontact friction*, PhD thesis, Cornell University, 2007.

[44] H. J. Mamin, M. Poggio, C. L. Degen, and D. Rugar, Nuclear magnetic resonance imaging with 90-nm resolution, Nature Nanotech. **2**, 301 (2007).

[45] Y. Obukhov, K. C. Fong, D. Daughton, and P. C. Hammel, Real time cantilever signal frequency determination using digital signal processing, J. Appl. Phys. **101**, 034315 (2007).

[46] F. J. Giessibl, Advances in atomic force microscopy, Rev. Mod. Phys. **75**, 949 (2003).

[47] P. T. Callaghan, *Principles of Nuclear Magnetic Resonance Microscopy*, Oxford University Press, 1991.

[48] K. W. Eberhardt, C. L. Degen, and B. H. Meier, Fast magnetic resonance force microscopy with hadamard encoding, Phys. Rev. B **76**, 180405 (2007).

[49] K. W. Eberhardt et al., Two-dimensional magnetic resonance force microscopy using full-volume fourier and hadamard encoding, Phys. Rev. B **78**, 214401 (2008).

[50] J. G. Kempf and J. A. Marohn, Nanoscale fourier-transform imaging with magnetic resonance force microscopy, Phys. Rev. Lett. **90**, 087601 (2003).

[51] T. D. Stowe et al., Attonewton force detection using ultrathin silicon cantilevers, Appl. Phys. Lett. **71**, 288 (1997).

[52] N. E. Jenkins et al., Batch fabrication and characterization of ultrasensitive cantilevers with submicron magnetic tips, J. Vac. Sci. Technol. B **22**, 909 (2004).

[53] K. Wago, D. Botkin, C. S. Yannoni, and D. Rugar, Paramagnetic and ferromagnetic resonance imaging with a tip-on-cantilever magnetic resonance force microscope, Appl. Phys. Lett. **72**, 2757 (1998).

[54] H. J. Mamin, R. Budakian, B. W. Chui, and D. Rugar, Magnetic resonance force microscopy of nuclear spins: Detection and manipulation of statistical polarization, Phys. Rev. B **72**, 024413 (2005).

[55] N. I. Kato, Reducing focused ion beam damage to transmission electron microscopy samples, J. Electron. Microsc. **53**, 451 (2004).

[56] B. C. Stipe, H. J. Mamin, T. D. Stowe, T. W. Kenny, and D. Rugar, Magnetic dissipation and fluctuations in individual nanomagnets measured by ultrasensitive cantilever magnetometry, Phys. Rev. Lett. **86**, 2874 (2001).

[57] T. N. Ng, N. E. Jenkins, and J. Marohn, Thermomagnetic fluctuations and hysteresis loops of magnetic cantilevers for magnetic resonance force microscopy, IEEE T. Magn. **42**, 378 (2006).

[58] M. Giorgio, B. Meier, R. Magin, and E. Meyer, Magnetic damping losses of tipped cantilevers, Nanotechnology **17**, 871 (2006).

[59] D. Rugar et al., Force detection of nuclear magnetic resonance, Science **264**, 1560 (1994).

[60] J. A. Sidles et al., Magnetic resonance force microscopy, Rev. Mod. Phys. **67**, 249 (1995).

[61] S. Kuehn, S. A. Hickman, and J. A. Marohn, Advances in mechanical detection of magnetic resonance, J. Chem. Phys. **128**, 052208 (2008).

[62] S. A. Hickman, *Batch Fabrication of Cantilevered Magnetic Nanorods on Attonewton-Sensitivity Silicon Oscillators for Magnetic Resonance Force Microscopy*, PhD thesis, Cornell University, 2010.

[63] J. G. Longenecker, PhD thesis, Cornell University, 2012.

[64] S. M. Yazdanian, J. A. Marohn, and R. F. Loring, Dielectric fluctuations in force microscopy: Noncontact friction and frequency jitter, J. Chem. Phys **128**, 224706 (2008).

[65] D. Rugar, Private communication, 2011.

[66] J. L. Du, G. R. Eaton, and S. S. Eaton, Temperature, orientation, and solvent dependence of electron spin-lattice relaxation rates for nitroxyl radicals in glassy solvents and doped solids, J. Magn. Reson. A **115**, 213 (1995).

[67] Y. Zhou, B. E. Bowler, G. R. Eaton, and S. S. Eaton, Electron spin lattice relaxation rates for S = 1/2 molecular species in glassy matrices or magnetically dilute solids at temperatures between 10 and 300 K, J. Magn. Reson. **139**, 165 (1999).

[68] C. T. Farrar, D. A. Hall, G. J. Gerfen, S. J. Inati, and R. G. Griffin, Mechanism of dynamic nuclear polarization in high magnetic fields, J. Chem. Phys. **114**, 4922 (2001).

[69] H. J. Mamin, R. Budakian, B. W. Chui, and D. Rugar, Detection and manipulation of statistical polarization in small spin ensembles, Phys. Rev. Lett. **91**, 207604 (2003).

[70] D. Rugar, C. S. Yannoni, and J. A. Sidles, Mechanical detection of magnetic resonance, Nature **360**, 563 (1992).

[71] K. J. Bruland et al., Thermal tuning of a fiber-optic interferometer for maximum sensitivity, Rev. Sci. Instrum. **70**, 3542 (1999).

[72] D. Rugar, H. J. Mamin, and P. Guenther, Improved fiber-optic interferometer for atomic force microscopy, Appl. Phys. Lett. **55**, 2588 (1989).

[73] E. R. Abraham and E. A. Cornell, Teflon feedthrough for coupling optical fibers into ultrahigh vacuum systems, Appl. Opt. **37**, 1762 (1998).

[74] D. Rugar et al., Adventures in attonewton force detection, Appl. Phys. A: Mater. Sci. Process. **72**, S3 (2001).

[75] J. Hutter and J. Bechhoefer, Calibration of atomic-force microscope tips, Rev. Sci. Instrum. **64**, 1868 (1993).

[76] K. Kim and S. Lee, Self-oscillation mode induced in an atomic force microscope cantilever, J. Appl. Phys. **91**, 4715 (2002).

[77] H. Hölscher, P. Milde, U. Zerweck, L. M. Eng, and R. Hoffmann, The effective quality factor at low temperatures in dynamic force microscopes with fabry–pérot interferometer detection, Appl. Phys. Lett. **94**, 223514 (2009).

[78] P. Y. Ktonas and N. Papp, Instantaneous envelope and phase extraction from real signals: theory, implementation, and an application to EEG analysis, Signal Processing **2**, 373 (1980).

[79] B. Boashash, Estimating and interpreting the instantaneous frequency of a signal I. fundamentals, Proc. IEEE **80**, 520 (1992).

[80] B. Boashash, Estimating and interpreting the instantaneous frequency of a signal. II. algorithms and applications, Proc. IEEE **80**, 540 (1992).

[81] P. Horowitz and W. Hill, *The Art of Electronics, 2nd Ed.*, Cambridge University Press, 1989.

[82] W. J. Wallace and R. H. Silsbee, Microstrip resonators for electron-spin resonance, Rev. Sci. Instrum. **62**, 1754 (1991).

[83] H. How, A. Widom, and C. Vittoria, Lagrangian formulation of a linear microstrip resonator: theory and experiment, IEEE T. Microw. Theory. **39**, 660 (1991).

[84] S. Ramo, J. R. Whinnery, and T. Van Duzer, *Fields and Waves in Communication Electronics, 2nd Ed.*, Wiley, 1984.

[85] T. C. Edwards and M. B. Steer, *Foundations of Interconnect and Microstrip Design, 3rd Ed.*, Wiley, 2000.

[86] H. Wheeler, Transmission-line properties of a strip on a dielectric sheet on a plane, IEEE T. Microw. Theory. **25**, 631 (1977).

[87] B. C. Stipe, H. J. Mamin, T. D. Stowe, T. W. Kenny, and D. Rugar, Non-contact friction and force fluctuations between closely spaced bodies, Phys. Rev. Lett. **87**, 096801 (2001).

[88] R. R. Ernst, G. Bodenhausen, and A. Wokaun, *Principles of Nuclear Magnetic Resonance in One and Two Dimensions*, Oxford University Press, USA, 1990.

[89] K. M. Salikhov and Y. D. Tsvetkov, *Time Domain Electron Spin Resonance*, chapter 7, pages 231 – 277, Wiley, NY, 1979.

[90] W. M. Dougherty et al., The bloch equations in high-gradient magnetic resonance force microscopy: Theory and experiment, J. Magn. Reson. **143**, 106 (2000).

[91] J. D. Hannay, R. W. Chantrell, and D. Rugar, Thermal field fluctuations in a magnetic tip / implications for magnetic resonance force microscopy, J. Appl. Phys. **87**, 6827 (2000).

[92] V. S. Bajaj et al., Dynamic nuclear polarization at 9 T using a novel 250 GHz gyrotron microwave source, J. Magn. Reson. **160**, 85 (2003).

[93] K. J. Bruland, W. M. Dougherty, J. L. Garbini, J. A. Sidles, and S. H. Chao, Force-detected magnetic resonance in a field gradient of 250 000 tesla per meter, Appl. Phys. Lett. **73**, 3159 (1998).

[94] L. Shtirberg et al., High-sensitivity Q-band electron spin resonance imaging system with submicron resolution, Rev. Sci. Instrum. **82**, 043708 (2011).

[95] K. Wago, D. Botkin, C. S. Yannoni, and D. Rugar, Force-detected electron-spin resonance: Adiabatic inversion, nutation, and spin echo, Phys. Rev. B **57**, 1108 (1998).

[96] M. Poggio, C. L. Degen, C. T. Rettner, H. J. Mamin, and D. Rugar, Nuclear magnetic resonance force microscopy with a microwire rf source, Appl. Phys. Lett. **90**, 263111 (2007).

[97] T. H. Oosterkamp, M. Poggio, C. L. Degen, H. J. Mamin, and D. Rugar, Frequency domain multiplexing of force signals with application to magnetic resonance force microscopy, Appl. Phys. Lett. **96**, 083107 (2010).

[98] R. Narkowicz, D. Suter, and I. Niemeyer, Scaling of sensitivity and efficiency in planar microresonators for electron spin resonance, Rev. Sci. Instrum. **79**, 084702 (2008).

[99] Y. Twig, E. Suhovoy, and A. Blank, Sensitive surface loop-gap microresonators for electron spin resonance, Rev. Sci. Instrum. **81**, 104703 (2010).

[100] D. I. Schuster et al., High-cooperativity coupling of electron-spin ensembles to superconducting cavities, Phys. Rev. Lett. **105**, 140501 (2010).

[101] R. G. Griffin and T. F. Prisner, High field dynamic nuclear polarization—the renaissance, Phys. Chem. Chem. Phys. **12**, 5737 (2010).

[102] Y. Maguire, I. L. Chuang, S. Zhang, and N. Gershenfeld, Ultra-small-sample molecular structure detection using microslot waveguide nuclear spin resonance, Proc. Natl. Acad. Sci. **104**, 9198 (2007).

[103] K. C. Gupta, R. Garg, and I. J. Bahl, *Microstrip Lines and Slotlines*, Artech House, 1979.

[104] G. Ghione and C. U. Naldi, Coplanar waveguides for MMIC applications: Effect of upper shielding, conductor backing, finite-extent ground planes, and line-to-line coupling, IEEE T. Microw. Theory. **35**, 260 (1987).

[105] A. Reyes, S. El-Ghazaly, S. Dorn, M. Dydyk, and D. Schroder, Silicon as a microwave substrate, in *Microwave Symposium Digest, IEEE MTT-S International*, pages 1759 –1762 vol.3, 1994.

[106] J. B. Hertzberg, *Back-Action Evading Measurements of Nanomechanical Motion Approaching Quantum Limits*, PhD thesis, University of Maryland, 2009.

[107] D. Mozyrsky, I. Martin, D. Pelekhov, and P. C. Hammel, Theory of spin relaxation in magnetic resonance force microscopy, Appl. Phys. Lett. **82**, 1278 (2003).

[108] H. J. Mamin, R. Budakian, and D. Rugar, Superconducting microwave resonator for millikelvin magnetic resonance force microscopy, Rev. Sci. Instrum. **74**, 2749 (2003).

[109] J. G. Longenecker, E. W. Moore, and J. A. Marohn, Rapid serial prototyping of magnet-tipped attonewton-sensitivity cantilevers by focused ion beam manipulation, J. Vac. Sci. Technol. B **29**, 032001 (2011).

[110] V. B. Braginsky, *Systems with Small Dissipation*, Chicago Press, 1985.

[111] K. Yasumura et al., Quality factors in micron- and submicron-thick cantilevers, J. Microelectromech. Syst. **9**, 117 (2000).

[112] S. M. Yazdanian, N. Hoepker, S. Kuehn, R. F. Loring, and J. A. Marohn, Quantifying electric field gradient fluctuations over polymers using ultrasensitive cantilevers, Nano Lett. **9**, 2273 (2009).

[113] H. Goldstein, *Classical Mechanics, 2nd Ed.*, Addison-Wesley, 1980.

[114] R. Grimshaw, *Nonlinear Ordinary Differential Equations*, CRC Press, 1993.

[115] T. L. Ferrell, Hamilton-Jacobi perturbation theory, Am. J. Phys. **39**, 622 (1971).

[116] F. J. Giessibl, Forces and frequency shifts in atomic-resolution dynamic-force microscopy, Phys. Rev. B **56**, 16010 (1997).

[117] G. P. Berman, F. Borgonovi, and V. I. Tsifrinovich, Theory of frequency shifts in the oscillating cantilever-driven adiabatic reversals technique as a function of the spin location, Phys. Rev. B **72**, 224406 (2005).

[118] H. C. Torrey, Transient nutations in nuclear magnetic resonance, Phys. Rev. **76**, 1059 (1949).

[119] R. Budakian, Private communication, 2011.

[120] J.-H. Choi et al., Oscillator microfabrication, micromagnets, and magnetic resonance force microscopy, Proc. SPIE **5389**, 399 (2004).

[121] D. Rugar and P. Grütter, Mechanical parametric amplification and thermo-mechanical noise squeezing, Phys. Rev. Lett. **67**, 699 (1991).

[122] D. W. Carr, S. Evoy, L. Sekaric, H. G. Craighead, and J. M. Parpia, Parametric amplification in a torsional microresonator, Appl. Phys. Lett. **77**, 1545 (2000).

[123] M. Zalalutdinov et al., Optically pumped parametric amplification for micromechanical oscillators, Appl. Phys. Lett. **78**, 3142 (2001).

[124] A. Kikukawa, S. Hosaka, and R. Imura, Silicon pn junction imaging and characterization using sensitivity enhanced kelvin probe microscopy, Appl. Phys. Lett. **66**, 3510 (1995).

[125] A. Naik et al., Cooling a nanomechanical resonator with quantum back-action, Nature **443**, 193 (2006).

[126] M. D. LaHaye, O. Buu, B. Camarota, and K. C. Schwab, Approaching the quantum limit of a nanomechanical resonator, Science **304**, 74 (2004).

[127] N. E. Flowers-Jacobs, D. R. Schmidt, and K. W. Lehnert, Intrinsic noise properties of atomic point contact displacement detectors, Phys. Rev. Lett. **98**, 096804 (2007).

[128] M. Poggio et al., An off-board quantum point contact as a sensitive detector of cantilever motion, Nature Physics **4**, 635 (2008).

[129] O. Arcizet et al., High-sensitivity optical monitoring of a micromechanical resonator with a quantum-limited optomechanical sensor, Phys. Rev. Lett. **97**, 133601 (2006).

[130] H. I. Rasool, P. R. Wilkinson, A. Z. Stieg, and J. K. Gimzewski, A low noise all-fiber interferometer for high resolution frequency modulated atomic force microscopy imaging in liquids, Rev. Sci. Instrum. **81**, 023703 (2010).

[131] H. J. Mamin and D. Rugar, Sub-attonewton force detection at millikelvin temperatures, Appl. Phys. Lett. **79**, 3358 (2001).

[132] J. Mertz, O. Marti, and J. Mlynek, Regulation of a microcantilever response by force feedback, Appl. Phys. Lett. **62**, 2344 (1993).

[133] R. Budakian, H. J. Mamin, and D. Rugar, Spin manipulation using fast cantilever phase reversals, Appl. Phys. Lett. **89**, 113113 (2006).

[134] H. N. Bertram, *Theory of Magnetic Recording*, Cambridge University Press, 1994.

[135] D. Weller and A. Moser, Thermal effect limits in ultrahigh-density magnetic recording, IEEE Trans. Mag. **35**, 4423 (1999).

[136] C. A. Ross, Patterned magnetic recording media, Ann. Rev. Materials Res. **31**, 203 (2001).

[137] A. Moser et al., Magnetic recording: Advancing into the future, J. Phys. D **35**, 157 (2002).

[138] S. A. Wolf et al., Spintronics: A spin-based electronics vision for the future, Science **294**, 1488 (2001).

[139] N. Smith and P. Arnett, White-noise magnetization fluctuations in magnetoresistive heads, Appl. Phys. Lett. **78**, 1448 (2001).

[140] W. Wernsdorfer et al., Experimental evidence of the Néel-Brown model of magnetization reversal, Phys. Rev. Lett. **78**, 1791 (1997).

[141] P. Grütter, Y. Liu, P. LeBlanc, and U. Dürig, Magnetic dissipation force microscopy, Appl. Phys. Lett. **71**, 279 (1997).

[142] C. W. Miller, U. M. Mirsaidov, T. C. Messina, Y. J. Lee, and J. T. Markert, External field effects on the resonant frequency of magnetically capped

oscillators for magnetic resonance force microscopy, J. Appl. Phys. **93**, 6572 (2003).

[143] R. O'Barr et al., Preparation and quantitative magnetic studies of single-domain nickel cylinders, J. Appl. Phys. **79**, 5303 (1996).

[144] W. Wernsdorfer et al., Nucleation of magnetization reversal in individual nanosized nickel wires, Phys. Rev. Lett. **77**, 1873 (1996).

[145] W. Wernsdorfer et al., Measurements of magnetization switching in individual nickel nanowires, Phys. Rev. B **55**, 11552 (1997).

[146] A. Aharoni, Demagnetizing factors for rectangular ferromagnetic prisms, J. Appl. Phys. **83**, 3432 (1998).

[147] U. Dürig, H. R. Steinauer, and N. Blanc, Dynamic force microscopy by means of the phase-controlled oscillator method, J. Appl. Phys. **82**, 3641 (1997).

[148] E. C. Stoner and E. P. Wohlfarth, A mechanism of magnetic hysteresis in heterogeneous alloys, Phil. Trans. R. Soc. Lond. A **240**, 599 (1948).

[149] J. H. E. Griffiths and J. R. MacDonald, An oscillation type magnetometer, J. Sci. Instrum. **28**, 56 (1951).

[150] J.-E. Wegrowe, D. Kelly, A. Franck, S. E. Gilbert, and J.-P. Ansermet, Magnetoresistance of ferromagnetic nanowires, Phys. Rev. Lett. **82**, 3681 (1999).